



University of Kentucky
UKnowledge

Theses and Dissertations--Physics and
Astronomy

Physics and Astronomy


2021

Predicting Material Properties: Applications of Multi-Scale Multiphysics Numerical Modeling to Transport Problems in Biochemical Systems and Chemical Process Engineering

Tom Pace

University of Kentucky, tompace101@gmail.com

Author ORCID Identifier:

 <https://orcid.org/0000-0003-3364-5123>

Digital Object Identifier: <https://doi.org/10.13023/etd.2021.162>

[Right click to open a feedback form in a new tab to let us know how this document benefits you.](#)

Recommended Citation

Pace, Tom, "Predicting Material Properties: Applications of Multi-Scale Multiphysics Numerical Modeling to Transport Problems in Biochemical Systems and Chemical Process Engineering" (2021). *Theses and Dissertations--Physics and Astronomy*. 84.

https://uknowledge.uky.edu/physastron_etds/84

This Doctoral Dissertation is brought to you for free and open access by the Physics and Astronomy at UKnowledge. It has been accepted for inclusion in Theses and Dissertations--Physics and Astronomy by an authorized administrator of UKnowledge. For more information, please contact UKnowledge@lsv.uky.edu.

STUDENT AGREEMENT:

I represent that my thesis or dissertation and abstract are my original work. Proper attribution has been given to all outside sources. I understand that I am solely responsible for obtaining any needed copyright permissions. I have obtained needed written permission statement(s) from the owner(s) of each third-party copyrighted matter to be included in my work, allowing electronic distribution (if such use is not permitted by the fair use doctrine) which will be submitted to UKnowledge as Additional File.

I hereby grant to The University of Kentucky and its agents the irrevocable, non-exclusive, and royalty-free license to archive and make accessible my work in whole or in part in all forms of media, now or hereafter known. I agree that the document mentioned above may be made available immediately for worldwide access unless an embargo applies.

I retain all other ownership rights to the copyright of my work. I also retain the right to use in future works (such as articles or books) all or part of my work. I understand that I am free to register the copyright to my work.

REVIEW, APPROVAL AND ACCEPTANCE

The document mentioned above has been reviewed and accepted by the student's advisor, on behalf of the advisory committee, and by the Director of Graduate Studies (DGS), on behalf of the program; we verify that this is the final, approved version of the student's thesis including all changes required by the advisory committee. The undersigned agree to abide by the statements above.

Tom Pace, Student

Dr. Peter M. Kekenos-Huskey, Major Professor

Dr. Christopher B. Crawford, Director of Graduate Studies

PREDICTING MATERIAL PROPERTIES:
APPLICATIONS OF MULTI-SCALE MULTIPHYSICS
NUMERICAL MODELING TO TRANSPORT PROBLEMS
IN BIOCHEMICAL SYSTEMS AND CHEMICAL PROCESS ENGINEERING

DISSERTATION

A dissertation submitted in partial fulfillment of the
requirements for the degree of Doctor of Philosophy in the
College of Arts and Sciences at the University of Kentucky

By
Thomas G. Pace
Lexington, Kentucky

Co-Directors: Dr. Peter M. Kekenos-Huskey,
Associate Professor of Cell and Molecular Physiology

and Dr. Ribhu K. Kaul,
Professor of Physics and Astronomy

Lexington, Kentucky

Copyright © Thomas G. Pace 2021

<https://orcid.org/0000-0003-3364-5123>

ABSTRACT OF DISSERTATION

PREDICTING MATERIAL PROPERTIES: APPLICATIONS OF MULTI-SCALE MULTIPHYSICS NUMERICAL MODELING TO TRANSPORT PROBLEMS IN BIOCHEMICAL SYSTEMS AND CHEMICAL PROCESS ENGINEERING

Material properties are used in a wide variety of theoretical models of material behavior. Descriptive properties quantify the nature, structure, or composition of the material. Behavioral properties quantify the response of the material to an imposed condition. The central question of this work concerns the prediction of behavioral properties from previously determined descriptive properties through hierarchical multi-scale, multiphysics models implemented as numerical simulations. Applications covered focus on mass transport models, including sequential enzyme-catalyzed reactions in systems biology, and an industrial chemical process in a common reaction medium.

KEYWORDS: Finite Element Method, Homogenization, Transport, Zeolites

Thomas G. Pace

May 12, 2021

PREDICTING MATERIAL PROPERTIES:
APPLICATIONS OF MULTI-SCALE MULTIPHYSICS
NUMERICAL MODELING TO TRANSPORT PROBLEMS
IN BIOCHEMICAL SYSTEMS AND CHEMICAL PROCESS ENGINEERING

By
Thomas G. Pace

Peter M. Kekenus-Huskey
Co-Director of Dissertation

Ribhu K. Kaul
Co-Director of Dissertation

Christopher B. Crawford
Director of Graduate Studies

May 12, 2021

*and lean not
on your own
understanding*

ACKNOWLEDGMENTS

I thank Dr. Pete Kekenes-Huskey for his support and guidance, for introducing me to the area of multiphysics models in mass transport systems, for helping me learn to the technique of Molecular Dynamics, for introducing me to asymptotic homogenization, and for the opportunity to use and further develop my skills with the Finite Element Method. I also thank him for his patience and understanding during the time of our work together.

I thank Dr. Ribhu Kaul for his support and encouragement over the years, through the many ups and downs of my doctoral studies, and his willingness to help me work through the complexity of my situation as a returning student.

I thank the other members of my committee for their helpful comments and suggestions. This includes Dr. Douglas Strachan from Physics, Dr. Jason DeRouchey from Chemistry, and Dr. Christoph Brehm from Mechanical Engineering. I thank Dr. Kate Ponto from Mathematics for her participation as the committee member appointed by the Graduate School.

I thank my fellow students Dylan Colli and Hadi Rahmaninejad for their contributions to our mutual projects. I am also grateful to the other members of our research group for beneficial conversations and camaraderie.

The Director of Graduate Studies, Dr. Christopher Crawford, also fielded many questions about the requirements of the doctoral program with great patience. I thank him for doing the extra work to understand and explain the rules that apply in unusual situations like mine. I know that I am not the only student for whom he has been a stabilizing force during difficult times.

I thank also Dr. David Singh and Dr. Madhu Menon. Along with Dr. Ribhu Kaul, they helped me gain experience in Density Functional Theory. Even though

my experience with Density Functional Theory is mostly not discussed herein, I hope to return to problems of electronic structure and computational chemistry at some point in my career.

I also thank my Stantec supervisors, Greg Yankey and Dr. Alan Rauch, for their support and patience during the eight years I was a part-time graduate student and part-time employee. I am also grateful to my other colleagues at Stantec for their willingness to work around my schedule.

Most of this thesis was compiled during the COVID-19 pandemic. Accordingly, I wish to thank all the workers in health care and other occupations who faced the greatest risk to their own safety during this time. I also thank Kentucky's Governor, Andy Beshear, for his courageous leadership throughout this ongoing crisis.

I am exceptionally grateful to my wife and children, who have made many sacrifices, over many years, so that this could be possible. I cannot describe how important to me their encouragement and support have been. I would also like to thank my parents, brothers, and extended family for their support as well.

Above all, I am grateful to that boundless and eternal Power that once created and still sustains all things, that is stronger even in defeat than evil is even in triumph, and that is available in each of us if sought.

One final acknowledgement: the work you are now reading is certainly an imperfect, incomplete one. As in all endeavors, I have learned things in doing this work that I wish I had known when I first began it. While this document marks the end of my education in an official capacity, learning truly is a lifelong commitment. In this spirit, whatever the future may hold for me, I hope that I may always be considered a student.

TABLE OF CONTENTS

Acknowledgments	iii
Table of Contents	v
List of Tables	vii
List of Figures	viii
Chapter 1 Introduction	1
1.1 Objective, Organization, and Notation	1
1.2 Multi-scale Models	2
1.3 Multiphysics Models	3
1.4 Heat and Diffusion Equations	4
1.5 Fickian Diffusion	6
1.6 The Nernst-Planck and Smoluchowski Equations	7
1.7 Diffusion Coefficient	8
1.8 Other Diffusion Models	11
Chapter 2 Principal Methods	14
2.1 Overview	14
2.2 Electronic Structure Calculations	14
2.3 Molecular Simulations	17
2.4 The Finite Element Method	19
2.5 Periodic Homogenization	21
2.6 Stochastic Homogenization	23
Chapter 3 Sequential Enzymes in a Nanoscale Domain	26
3.1 Background	26
3.2 Geometry of a Nanoporous Membrane	26
3.3 Fickian Diffusion in a Nanoscale Pore	29
3.4 Electro-diffusion in a Nanoscale Pore	32
3.5 Diffusion-Limited Reaction Kinetics of a Single Enzyme	39
3.6 Diffusion-Limited Kinetics of Sequential Enzyme-Catalyzed Reactions	41
3.7 Discussion and Conclusion	43
Chapter 4 Transport Properties of Zeolites and Other Porous Silicates	45
4.1 Background	45
4.2 Theoretical Model	46
4.3 Silicate Channel System	48
4.4 Methods	50
4.5 Validation Analyses for Molecular Simulations	53

4.6	Validation Analyses for Homogenization of Fickian Diffusion	57
4.7	Validation Analyses for the Homogenized Smoluchowski Equation	59
4.8	Results of Homogenization for Zeolites	60
4.9	Results of Molecular Simulations in Silicate Channel	62
4.10	Effective Diffusion Coefficients for the Silicate Channel	69
4.11	Discussion and Conclusion	71
Chapter 5 Summary, Conclusions, and Speculation		73
5.1	Summary and Review: Successes and Limitations of the Methods	73
5.2	Speculation: The Possibility of Novel Algorithms	74
5.3	Conclusion: Continuing the Search for Useful Approximations	75
Appendices		77
Appendix A Glossary of Acronyms		78
Appendix B Glossary of Mathematical Notation		79
Appendix C Glossary of Terms		85
Appendix D Mathematical Derivations		90
D.1	Reaction-Diffusion Systems	90
D.2	Weak Forms for Unhomogenized Diffusion Equations	91
D.3	Homogenization of Fickian Diffusion	92
D.4	Weak Form for Homogenized Fickian Diffusion	95
D.5	Effective Diffusion Coefficient of Bi-Layered Media	97
D.6	Effective Diffusion Coefficient in an Example with Spatially Varying D_{local}	105
D.7	Conditions for Symmetry of the Homogenized Diffusion Coefficient Ma- trix	113
D.8	Effective Diffusion Coefficient from Solution of Fick's Law	114
D.9	Reactive Boundary Condition	116
D.10	Langevin Dynamics in a Harmonic Potential	118
D.11	Gauge-Dependence in the Homogenized Smoluchowski Equation with the Slotboom Transformation	120
D.12	An Example Problem for the Homogenized Smoluchowski Equation	122
References		131
Vita		146

LIST OF TABLES

1.1	Common linear gradient constitutive laws.	5
1.2	Continuity equations.	5
1.3	Anomalous diffusion regimes.	13
3.1	Unit cell geometries for the parametric variations of the nanoporous membrane.	30
4.1	Mean-Squared Displacement (MSD) results from simulations of methane in bulk water.	53
4.2	Diffusion coefficient results from simulations of methane in bulk water.	54
4.3	Diffusion coefficient results from unrestrained methane simulations in bulk water.	55
4.4	Results of effective tortuosity calculation.	61

LIST OF FIGURES

1.1	Analysis scales and relevant methods.	3
3.1	Two-dimensional geometry for a nanopore.	27
3.2	Three-dimensional geometry for a cylindrical nanopore.	28
3.3	Finite element mesh for nanoscale pore between reservoirs.	29
3.4	Concentration field from the solution of the steady-state Fickian diffusion.	30
3.5	Concentration profiles along pore centerline	31
3.6	Influence of porosity on the effective diffusion ratio.	32
3.7	Electric potential from the solution of the Linearized Poisson-Boltzmann equation.	33
3.8	Concentration field from solution of the Smoluchowski Equation.	34
3.9	Solution variables for Smoluchowski diffusion, taken along the model centerline.	35
3.10	Solution variables along radial lines.	36
3.11	Concentration profiles along pore centerline	37
3.12	Influence of electrostatic interaction on relationship between effective diffusion ratio and porosity.	38
3.13	Reaction rate coefficient within the nanopore.	41
3.14	Cut through finite element mesh with reactive inclusions.	42
3.15	Cut through finite element mesh with non-diffusive inclusions.	43
4.1	Renderings of four different zeolite frameworks.	45
4.2	Geometry of the silicate channel model.	49
4.3	Comparison of position Autocorrelation Functions (ACFs) using two different force fields.	54
4.4	Calculation of diffusion coefficient from MSD	55
4.5	Comparison of diffusion coefficient for methane in bulk water from different methods.	56
4.6	Water density around a methane molecule, for two different simulation durations.	57
4.7	Unit cell for the idealized geometry.	58
4.8	Result of homogenization of the idealized geometry.	58
4.9	Validation of the homogenized Smoluchowski equation.	59
4.10	Face-on and oblique views of the finite element mesh for the BEA zeolite framework.	60
4.11	Results of homogenization of the zeolite meshes, with constant D_{local}	61
4.12	Water density near the silicate face from the Molecular Dynamics (MD) simulation with a channel width of 1.6 nm.	62
4.13	Water density in the MD silicate simulation with a channel width of 1.6 nm.	63
4.14	Examples of local diffusion coefficient in the 1.6 nm channel.	64

4.15	Spatial variation of averaged PMF, local diffusion coefficient, and water density in the 1.6 nm channel.	65
4.16	Water density, local diffusion coefficient, and potential of mean force for a plane in the 1.2 nm channel, fully protonated. The imposed rectangle shows the limits of data used in the finite element model within the plane.	66
4.17	Water density, local diffusion coefficient, and potential of mean force for a plane in the 1.6 nm channel, fully protonated. The imposed rectangle shows the limits of data used in the finite element model within the plane.	66
4.18	Water density, local diffusion coefficient, and potential of mean force for a plane in the 2.0 nm channel, fully protonated. The imposed rectangle shows the limits of data used in the finite element model within the plane.	67
4.19	Water density, local diffusion coefficient, and potential of mean force for a plane in the 2.0 nm channel, 27% de-protonated. The imposed rectangle shows the limits of data used in the finite element model within the plane.	67
4.20	Water density, local diffusion coefficient, and potential of mean force for a plane in the 2.0 nm channel, 50% de-protonated. The imposed rectangle shows the limits of data used in the finite element model within the plane.	68
4.21	Predicted effective diffusion coefficient for a silicate channel as a function of wall separation.	70
4.22	Predicted effective diffusion coefficient for a silicate channel as a function of de-protonation level.	71

Chapter 1 Introduction

1.1 Objective, Organization, and Notation

Engineering and the physical sciences use mathematical models to describe and predict the behavior of a system under study. These models define abstract concepts representing real-world phenomena, and express principles governing the causal relationships between these concepts. Many mathematical models include coefficients referred to as *material properties*. These properties quantify various characteristics of a material as it relates to a mathematical model.

Consider the following two types of material properties: *descriptive* properties are those that define the nature, structure, or composition of a material. In contrast, *behavioral* properties are those that quantify the response of the material to different imposed conditions. For example, the chemical composition of a metal is a descriptive property, while the rate at which it corrodes in air is a behavioral property dependent on conditions of temperature, humidity, salinity, and others.

The object of this work is to investigate how to predict behavioral properties from descriptive properties. In other words, from a quantitative description of what a material *is*, can we predict how it *behaves*?

In practice, it may sometimes be more prudent to proceed in the reverse direction: predicting descriptive properties by making use of previously established behavioral ones. For example, the behavioral properties involved might be easier to measure experimentally than the descriptive ones. Yet, even in such circumstances, the direction of causality is not reversed. The nature of a material governs its behavior simply because existence precedes action.

In a situation where a material is already available and its properties can be measured, there is no need to predict the properties. However, in situations where a desired set of properties is specified and a material meeting these requirements must be found, a model that can predict material properties can be helpful. Furthermore, in some cases material properties are observed in measurements, and then investigated theoretically to explain the measured results. Finally, there are some situations where attempts to measure a property would interfere with the processes that give rise to the property. This is the case in a biochemical system described in Chapter 3.

The distinction between descriptive and behavioral properties is often dependent on the scale considered: a descriptive property at one scale may be a behavioral property at a smaller scale. For example, the density of a solid is a descriptive property at the macroscale, but the density is determined by the masses of its constituent particles and their equilibrium separation distances. The separation distances, in turn, result from nanoscale interactions between the constituent particles of the solid.

These methods of prediction rely on two developing areas of mathematical modeling. First, a relevant model at one scale of observation can derive properties applicable to another model appropriate at a larger scale, as further discussed in Section 1.2. Secondly, the models used at each scale must incorporate all of the diverse physical

phenomena that are relevant, as further discussed in Section 1.3.

The scope of this study focuses primarily on material properties relating to the field of transport theory, as described in Sections 1.4, 1.5, 1.6, and 1.8. The primary (though not exclusive) material property of concern is described in more detail in Section 1.7.

The principal methods employed are reviewed in Chapter 2. Chapter 3 illustrates an application from the area of systems biology. Chapter 4 applies these methods to an industrial chemical process in a common reaction medium. Finally, Chapter 5 concludes with thoughts on possible areas of future investigation. Appendix A contains a list of abbreviations used herein. A glossary of the notation used for variables and operators is provided in Appendix B. A glossary of terms is provided in Appendix C. Various mathematical derivations referenced in the text are detailed in Appendix D.

The mathematical formulas presented herein are written with index notation [18, 93, 6]. Subscripts that are lowercase letters represent indices for dimensions of space unless otherwise noted. Repeated spatial indices within a term imply a summation over all spatial dimensions. Subscripts that are uppercase letters represent non-spatial indices, and are excluded from implied summation. The units or dimensions of a given quantity are expressed inside double square brackets. For example, dimensions of length are shown as $\llbracket L \rrbracket$. Names of software packages are written a typewriter font, such as `python`, `FEniCS`, and `gromacs`.

1.2 Multi-scale Models

Material properties are often themselves the result of complex processes taking place at smaller scales. A model of behavior at the smaller scale, which incorporates all of the relevant physical phenomena, can be used to estimate the appropriate material properties at the larger scale. Because the smaller-scale models may themselves include material properties of their own, this process can continue downward to lower and lower scales, eventually reaching the atomistic scale.

At the scale of electrons and nuclei, quantum mechanics is well-established as the relevant mathematical model, and the necessary experimentally-derived material properties, such as particle masses and charges, have already been measured to great precision. For this reason, models that begin with quantum-mechanical interactions of subatomic particles are often called *ab-initio* models.

Starting from *ab-initio* models, it is theoretically possible to derive properties for models at larger and larger scales, eventually reaching material properties at macroscopic scales of both length and time. In practice, this overall process is still developing, as described by the Materials Genome Initiative [31]:

Materials scientists have developed powerful computational tools to predict materials behavior, but these tools have fundamental deficiencies that limit their usefulness. The primary problem is that current predictive algorithms do not have the ability to model behavior and properties across

multiple spatial and temporal scales; for example, researchers can measure the atomic vibrations of a material in picoseconds, but from that information they cannot predict how the material will wear down over the course of years.

Figure 1.1 illustrates different analysis scales and the methods described herein relating to them. Similar figures, listing additional methods not included here, can be found in Raabe et al. [103], Kim [75], and Horstemeyer [59].

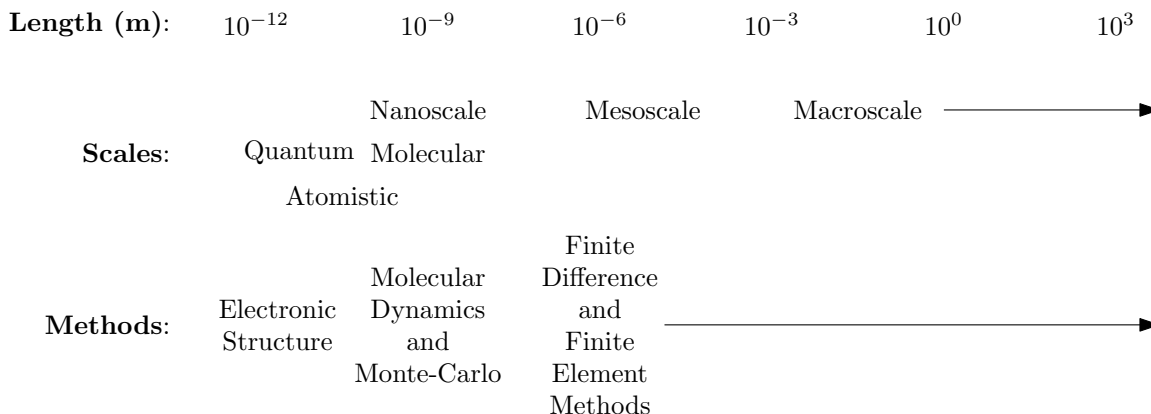


Figure 1.1: Analysis scales and relevant methods.

Multi-scale analysis involves not only selecting appropriate analysis methods within each scale, but also selecting appropriate methods of transferring information between scales. *Homogenization*, described in Chapter 2, is the primary method used herein for transferring information from a smaller scale to a larger one. Models where information passes only in this direction, from smaller scales to larger ones, are often called *hierarchical* multi-scale models.

1.3 Multiphysics Models

Many mathematical models have been defined within a particular area of study, such as Maxwell’s equations for electromagnetism, the theory of elasticity in continuum mechanics, and the equations of General Relativity to describe the gravitational interactions. Within the past few decades, a trend has emerged where models originally defined in different areas of study are combined to describe a particular system. For example, fluid dynamics and structural dynamics are both well-established areas of study with their own literature. However, models coupling these two theories have seen widespread use in the area of aircraft design for over 20 years [109]. This trend of combining mathematical models from different fields of study has come to be known as *multiphysics*.

The properties of a material are often governed by a set of phenomena that exhibit this kind of multiphysics coupling. Specifically, the applications described in Chapters 3 and 4 require consideration of coupled phenomena. The relevant combined mathematical models are described therein.

The topic of multiphysics simulations is very broad for two reasons: First, the number of possible combinations of fields of study is much larger than the number of fields to be combined. Additionally, a variety of different techniques are available to couple originally separate mathematical models [72].

Other examples of applications where multiphysics approaches have been used include coupling between mechanical strain and electronic behavior in devices [127], coupling between the ocean and the atmosphere in geophysics [72], and the coupling between deformation and fluid flow in a porous medium, which has applications in fields as diverse as geotechnical engineering and cardiac modeling [115].

1.4 Heat and Diffusion Equations

Mathematical descriptions of behavior of materials are often called *constitutive laws* or constitutive models. The simplest such laws are linear: they posit the response of a material is directly proportional to an applied stimulus. In these cases, the material property in question is the proportionality constant for this linear relationship.

The causal relationship between stimulus and response can often be reversed: either quantity may be imposed on the material while maintaining the constitutive relation. In thermodynamics, the terms *forces* and *currents*, respectively, are often used instead [98, 38]. The term *force* is used here in a very general sense, as these forces are not necessarily related directly to the time derivative of a momentum by Newton's second law [38].

The success of a linear model lies in making proper choices for the quantities to be related. For a given physical phenomenon, some pairs of quantities are more suitable than others. Some examples of successful linear constitutive models are listed in Table 1.1. Each of these models is often referred to as a *law* and named after a discoverer. The force variable in the model is the negative gradient of a scalar field in each case. Of course, many other linear constitutive models exist. The selection here is limited to only the laws that are most similar to Fick's Law, for the purpose of illustrating the broader areas in which the techniques used here can also be applied.

If the material property is a scalar value, then the force and current vectors will be anti-parallel. For a given force magnitude, the current magnitude will not vary with the direction in which force is applied. This condition is known as *isotropy*. In contrast, *anisotropic* conditions refer to situations where there is a dependence on the direction. In anisotropic conditions, the material property is a matrix (a tensor of rank 2) rather than a scalar value. The laws in Table 1.1 are written in a general form that allows for anisotropic conditions. For isotropic conditions, the property tensor is simply the identity matrix multiplied by a scalar value.

In practical analyses, constitutive laws must be combined with other governing equations. The equations of Table 1.1 are often combined with conservation laws expressed as continuity equations. The continuity equation corresponding to each constitutive law is shown in Table 1.2.

The constitutive laws of Table 1.1 can be substituted into the continuity equations of Table 1.2. In the case of the Fick's Law, with the additional assumption of an

Table 1.1: Common linear gradient constitutive laws.

Law	Phenomenon	Equation	Property
Fick's [47, 98, 120]	Diffusion	$j_i = -D_{ij}\partial_j c$ $j_i = \text{species flux}$ $c = \text{concentration}$	$D_{ij} =$ Diffusion Coefficient
Ohm's [51, 65]	Electrical Conduction	$J_i = -\sigma_{ij}\partial_j \Phi$ $J_i = \text{current density}$ $\Phi = \text{electric potential}$	$\sigma_{ij} =$ Conductivity
Fourier's [92, 16]	Heat Conduction	$\dot{q}_i = -\kappa_{ij}\partial_j T$ $\dot{q}_i = \text{heat flux}$ $T = \text{temperature}$	$\kappa_{ij} =$ Thermal Conductivity
Darcy's [11, 55]	Groundwater Seepage	$q_i = -K_{ij}\partial_j H$ $q_i = \text{specific discharge}$ $H = \text{total hydraulic head}$	$K_{ij} =$ Permeability

Table 1.2: Continuity equations.

Law	Continuity Equation	Time Derivative	Conserved Quantity
Fick's [16, 34, 120]	$\partial_t c = -\partial_i j_i$	$c = \text{concentration}$	Number of Molecules
Ohm's [51, 65]	$\partial_t \rho = -\partial_i J_i$	$\rho = \text{charge density}$	Electric Charge
Fourier's [8]	$\partial_t u = -\partial_i \dot{q}_i$	$u = \text{specific energy}$	Energy
Darcy's [29, 129]	$\partial_t (\phi\rho) = -\partial_i (\rho q_i)$	$\rho = \text{fluid density},$ $\phi = \text{porosity}$	Mass

isotropic and spatially invariant diffusion coefficient, the result is Equation 1.1, often known as Fick's Second Law of Diffusion [120].

$$\partial_t c = D\partial_i\partial_i c \quad (1.1)$$

A similar form of equation can be obtained for Fourier's Law by defining the thermal conductivity $\alpha = \kappa/\rho C$ for isotropic and spatially invariant thermal conductivity κ , mass density ρ , and heat capacity C . The result is Equation 1.2 [16, 8].

$$\partial_t T = \alpha\partial_i\partial_i T \quad (1.2)$$

Because Equations 1.1 and 1.2 have a similar form, other equations with this form are often called heat-flow or diffusion equations. For mathematical convenience, the constant within the equation is sometimes written as the square of another constant, for a general form given by Equation 1.3 [6, 18].

$$\partial_t \psi = \alpha^2\partial_i\partial_i \psi \quad (1.3)$$

1.5 Fickian Diffusion

Within the context of the equations presented in Section 1.4, this work is concerned mostly with applications of Fick's Laws.

Fick's First Law is the constitutive relation from Table 1.1 as shown in Equation 1.4. The relevant continuity equation from Table 1.2 is shown in Equation 1.5. In the general case where the diffusion coefficient may vary in space and is potentially anisotropic, Fick's Second Law as described in Section 1.4 can be written as Equation 1.6.

$$j_i = -D_{ij}\partial_j c \quad (1.4)$$

$$\partial_t c = -\partial_i j_i \quad (1.5)$$

$$\partial_t c = \partial_i (D_{ij}\partial_j c) \quad (1.6)$$

The variables of interest in Equations 1.4, 1.5, and 1.6 are the concentration and the flux. These variables describe the location and net motion of individual molecules, ions, or atoms suspended within a fluid or other medium. Herein, the diffusing molecules, ions, or atoms will be referred to as diffusing *particles*. The concentration, c , is a scalar field that represents the number of particles present per unit volume. Equivalently, when normalized to unity, the concentration may be considered as the probability density function for the location of a single particle, assuming the system is ergodic. The normalization factor for this equivalency is the total number of particles present within the system. For the continuity equation to be valid, this value must be invariant. The flux, j_i , is a vector field that represents the net motion of the particles. The units involved can be inferred from the units of concentration by unit analysis of the continuity equation. For example, if the concentration is expressed in units of particles per cubic nanometer, and nanometers are used for length and nanoseconds for time, then by the continuity equation the vector flux must be in units of particles per square nanometer per nanosecond.

An extension of this model to include chemical reactions is presented in Appendix D, Section D.1.

The term *flux* is also sometimes used to refer to the integration of the vector flux over a surface. Herein, this will be termed the *integrated flux*, and denoted with J_Γ for the flux through surface Γ , and defined by Equation 1.7. The vector $n_{\Gamma i}$ represents the unit normal to the surface, which will vary in space if the surface is not flat. The integrated flux represents the number of particles crossing the designated surface in a given period of time. Accordingly, the units of the integrated flux are the number of particles per unit time.

$$J_\Gamma = \int_\Gamma d\Gamma n_{\Gamma i} j_i \quad (1.7)$$

In some cases, more than one diffusing species will be considered simultaneously. In this, the variables will be given an uppercase species index, as in c_S , j_{Si} , and $J_{\Gamma S}$.

Fickian diffusion presumes a continuum. At a lower scale, of course, the medium through which any particles diffuse must itself be made of particles. For example, a solute molecule diffusing through a liquid solvent is actually surrounded by solvent molecules. At this discrete scale, diffusion is actually caused by Brownian motion and can be modeled as a random walk [116, 47, 98]. Passing from this discrete system to the continuum of Fick's Laws is an example of the statistical approach to multi-scaling.

Frequently, the *steady-state* solution of the diffusion equation will be desired, where the concentration is constant with respect to time. The governing equation for the steady-state condition is therefore given by Equation 1.8. Note that the fluxes can still be nonzero for steady-state conditions: the derivative of the concentration with respect to time is zero, but the spatial derivatives can be nonzero depending on the problem boundary conditions.

$$\partial_i (D_{ij} \partial_j c) = 0 \tag{1.8}$$

1.6 The Nernst-Planck and Smoluchowski Equations

The Fickian diffusion equations of Section 1.5 describe the diffusion of the molecules of a substance due to Brownian motion, as further described in Section 1.7. If, in addition to Brownian motion, the molecules are also subjected to force arising from a scalar potential, such as an electrostatic potential acting on ions, the diffusion equation must be modified to couple the action of the potential as well. The diffusion equation that includes the coupling to such a force is known in various references as the Nernst-Planck equation or the Smoluchowski equation [85], though the former name seems to be more strongly associated with an electrostatic potential and the latter name with a potential of unspecified source. Complete derivations of the equation are presented by Schulten and Kosztin [116] and Maex [86].

To include the effect of the potential, an additional term is added to the diffusive flux of Equation 1.4. The resulting flux can be written in two mathematically equivalent forms. The form that is linear in the potential is shown in Equation 1.9, and the form that contains exponential functions of the potential is shown in Equation 1.10 [136]. The mathematical equivalence of these two forms is observed by use of the product rule on the gradient in the exponential form, which ultimately leads to a cancellation of the exponential factors.

$$j_i = -D_{ij} (\partial_j c + \beta c \partial_j \Psi) \tag{1.9}$$

$$j_i = -D_{ij} e^{-\beta \Psi} \partial_j (e^{\beta \Psi} c) \tag{1.10}$$

While the exponential form may seem more complicated, it more readily lends itself to a convenient simplification. Specifically, the flux can be expressed in a purely Fickian form by means of the Slotboom transformation [85, 122]. The transformation

and its inverse are presented in Equations 1.11 and 1.12, respectively. Equation 1.13 presents the flux in terms of the transformed variables.

$$\begin{aligned}\bar{D}_{ij} &= D_{ij}e^{-\beta\Psi} \\ \bar{c} &= ce^{\beta\Psi}\end{aligned}\tag{1.11}$$

$$\begin{aligned}D_{ij} &= \bar{D}_{ij}e^{\beta\Psi} \\ c &= \bar{c}e^{-\beta\Psi}\end{aligned}\tag{1.12}$$

$$j_i = -\bar{D}_{ij}\partial_j\bar{c}\tag{1.13}$$

1.7 Diffusion Coefficient

Under general conditions, the diffusion coefficient is a matrix, D_{ij} . That is, changes in the coordinate axes of the problem transform the diffusion coefficient in the manner established for tensors of second rank. However, under isotropic conditions, the matrix can be expressed as a scalar D multiplied by the identity matrix. As isotropic conditions are common, especially for diffusion through fluid media, many references provide more information on the nature of the diffusion coefficient for this case. Additionally, many such discussions also assume that the diffusion coefficient is spatially invariant.

At the microscopic level, the process of diffusion results from Brownian motion of the diffusing particles. The equation of motion for a single such particle is a *Langevin equation*, which is a stochastic differential equation. That is, the equation of motion includes a term which varies randomly in time, representing the force applied to the particle from random collisions with solute molecules. This Langevin equation is shown in Equation 1.14, from which the *Einstein relation* of Equation 1.15 can be derived [98, 116].

$$M\partial_tv_i = -\xi v_i + F_i\tag{1.14}$$

where

$$\begin{aligned}M &= \text{particle mass } \llbracket\text{M}\rrbracket \\ v_i &= \text{time-dependent particle velocity vector } \llbracket\frac{\text{L}}{\text{T}}\rrbracket \\ \xi &= \text{coefficient of friction } \llbracket\frac{\text{M}}{\text{T}}\rrbracket \\ F_i &= \text{force varying randomly in time } \llbracket\text{F}\rrbracket\end{aligned}$$

$$D = \frac{1}{\beta\xi}\tag{1.15}$$

The coefficient of friction, ξ , depends on the size of the particle and the viscosity of the solvent. For a spherical particle of radius a , diffusing through a fluid with coefficient of viscosity η , $\xi = 6\pi\eta a$, which is known as *Stokes's Law* [98, 108]. The drift velocity of a diffusing particle subjected to a constant force of unit magnitude is $\frac{1}{\xi}$ [98].

Furthermore, by considering the process of Brownian motion as a random walk, it can be shown that the MSD of a Brownian particle grows linearly with time, with the proportionality constant related to the diffusion coefficient, as shown in Equation 1.16. If, instead of the MSD, only one Cartesian coordinate, q , is evaluated, the result is given by Equation 1.17 [98, 47].

$$\partial_t \langle r_i r_i \rangle = 2N_d D \quad (1.16)$$

$$\partial_t \langle q^2 \rangle = 2D \quad (1.17)$$

By expressing the coordinate q as the integral with respect to time of the corresponding velocity component v_q , Equation 1.17 can be used to show that D can also be obtained by integration of the Velocity Autocorrelation Function (VACF), as shown in Equation 1.18 [47].

$$D = \int_0^\infty dt \langle v_q(t) v_q(0) \rangle \quad (1.18)$$

Diffusion can also take place in *porous media*, where the diffusing substance travels within gas or liquid-filled pores through a solid. The solids themselves are typically considered to be impermeable, while the fluid within the pores has its own diffusion coefficient, D_{fluid} . At a larger scale, the porous medium will have a different diffusion coefficient than the fluid itself. This *effective diffusion coefficient*, D_{eff} , will generally be lower than D_{fluid} due to the obstructions imposed by the solid phase. An empirical approach to obtaining D_{eff} is illustrated in Equation 1.19, from Coutelieis and Delgado [32].

$$D_{\text{eff}} = D_{\text{fluid}} \frac{\epsilon \delta}{\tau} \quad (1.19)$$

where

$$\begin{aligned} \epsilon &= \text{effective porosity, dimensionless, } \leq 1 \\ \delta &= \text{constrictivity, dimensionless, } \leq 1 \\ \tau &= \text{tortuosity, dimensionless, } \geq 1 \end{aligned}$$

The three dimensionless factors in Equation 1.19 relate to phenomena that influence the value of D_{eff} . Each is described in Coutelieis and Delgado [32] as follows, along with empirical correlations. The effective porosity, ϵ , represents the reduction in the cross-sectional area of the pore space due to the obstruction from the solid phase. The effective porosity therefore depends on the shape of the pores in cross-section, perpendicular to the direction of flow. In contrast, the tortuosity, τ , depends on the shape of the pores along the direction of flow. Long, looping pores will increase the distance that must be traveled, and thus reduce the diffusion rate overall. Specifically, $\tau = \left(\frac{\ell_{\text{eff}}}{\ell}\right)^2$, where ℓ_{eff} is the effective path length and ℓ is the linear distance between points within the medium. While illustrative, this formula does not provide a means to actually evaluate the tortuosity for a given material. The final dimensionless factor is the constrictivity, δ , which depends on both the size

of the pores and the size of the diffusing particles. Diffusing particles taking up more of the available space within the pore transport more slowly than smaller particles.

For simple, one dimensional problems, the effective porosity, ϵ , is equivalent to the *porosity*, or *free volume fraction*, ϕ , of the material. The dimensionless value ϕ is the ratio of the volume of the void space within a material to the total volume. The value of ϕ thus ranges from zero, for a solid material, to unity, for a fluid with no solid phase.

For more complicated problems, the effective porosity ϵ is not equal to ϕ , but can sometimes be obtained through geometric analyses if the structure of the solid phase is simple enough. However, no such approaches are known for the tortuosity and constrictivity. Indeed, another empirical approach presented in Coutelieres and Delgado [32] dispenses with these latter variables, and instead simply uses an empirical exponential value, m , on the effective porosity, as shown in Equation 1.20.

$$D_{\text{eff}} = D_{\text{fluid}}\epsilon^m \tag{1.20}$$

For these reasons, the methods employed herein do not attempt to predict D_{eff} through the porosity, tortuosity, and constrictivity. Instead, a multi-scale approach is used as described in Chapter 2. Nonetheless, Equation 1.19 can be used to validate the multi-scale approach in sufficiently simple materials.

Anisotropic conditions can arise in porous media simply through anisotropic geometry of the solid phase. For example, a porous medium consisting of horizontal layers of different materials can be expected to have different transport behavior in horizontal directions than in the vertical direction. This is the case, for example, in the seepage of groundwater through soils, which often possess a layered structure because of natural deposition or artificial construction methods [55].

For situations where the diffusion is not isotropic, the diffusion coefficient matrix is generally symmetric [15]. However, as will be shown in Section 2.5, inhomogeneities at larger scales can yield asymmetry of the effective diffusion coefficient at those scales.

The diffusion coefficient matrix is not positive-definite, but is instead positive-semidefinite. A positive-definite matrix M_{ij} is one that where the product $M_{ij}x_ix_j$ is greater than zero for any nonzero vector x_i [24]. For a positive-semidefinite matrix, this product may be equal to zero for some nonzero vectors x_i , but is greater than zero for all others. That the diffusion coefficient must be positive-semidefinite is most easily seen by first considering the isotropic case, where the flux vector and the concentration gradient must be antiparallel. Consider the dot product of the flux and the concentration gradient, $j_i\partial_ic$. For the vectors to be antiparallel, this dot product must be negative. The dot product could also be zero, for the case of zero flux caused by an impermeable medium. For anisotropic conditions, the vectors are no longer necessarily antiparallel, but the dot product must still be zero or negative. From this requirement, the steps to demonstrate that the diffusion coefficient matrix

is positive-semidefinite are shown in Equation 1.21.

$$\begin{array}{ll}
\text{Dot product described above:} & j_i \partial_i c \leq 0 \\
\text{Substitute Fick's First Law (Equation 1.4) for flux:} & (-D_{ij} \partial_j c) \partial_i c \leq 0 \\
\text{Multiply by -1:} & (D_{ij} \partial_j c) \partial_i c \geq 0 \\
\text{Define vector } x_i = \partial_i c: & D_{ij} x_i x_j \geq 0 \\
\text{\textit{D}_{ij} is positive-semidefinite by the definition above:} & M_{ij} x_i x_j \geq 0 \\
\text{\textit{QED}} &
\end{array} \tag{1.21}$$

A matrix which is symmetric and positive-semidefinite can be *diagonalized*. That is, there exists a rotation of the coordinate system under which the diffusion coefficient matrix consists of N_d scalar values on the diagonal of the matrix, with all off-diagonal terms being zero. This coordinate system, and the associated diagonal values of the matrix, can be found by obtaining the eigenvalues and eigenvectors of the matrix in another coordinate system. The eigenvalues are the principal diffusion coefficients, and the eigenvectors are the axes along which these coefficients apply. For a matrix which is positive-definite, the eigenvalues are all positive numbers. The diffusion coefficient matrix is positive-semidefinite, meaning that zero is a possible eigenvalue. This would be the case for a medium which has at least one direction in which it is impermeable.

Under particular conditions of anisotropy known as *orthotropic* conditions, the principal axes of the diffusion coefficient are aligned with the coordinate axes, and so the matrix is diagonal. In such a scenario, the isotropic D in Equations 1.17 and 1.18 would be replaced with the diagonal component D_{xx} . Equation 1.16 would not be valid in such a scenario.

1.8 Other Diffusion Models

The diffusion equations used in this work are only a subset of mass transport models used in a wide variety of applications. This section briefly describes a small selection of the situations in which models other than those described herein might be appropriate.

One common multiphysics generalization of Fickian diffusion includes convection-diffusion systems. Examples of such systems include some chemical separation processes and dispersal of atmospheric pollutants [57, 63]. In convection-diffusion systems, a substance diffuses through a medium which is itself also in motion, with velocity field v_i . In more complicated models, this velocity field may be coupled with fluid dynamics models such as the Navier-Stokes equations. With a nonzero velocity field, the total flux includes not only the diffusive flux as from Fick's first law, but also the advective flux [57]:

$$j_i = j_{i,\text{diffusive}} + j_{i,\text{advective}} \tag{1.22}$$

$$j_{i,\text{diffusive}} = -D_{ij} \partial_j c \tag{1.23}$$

$$\dot{j}_{i,\text{advective}} = v_i c \quad (1.24)$$

In this work, the velocity field $v_i = 0$, and so only the diffusive flux is nonzero.

Furthermore, the diffusion equations of Sections 1.5 and 1.6 generally refer to the diffusion of a chemical species through a solvent also consisting of a single chemical species. This condition can be described as *binary diffusion*, as only two chemical components are considered. Binary diffusion can also describe situations where two substances mix in concentrations allowing mutual solvation. These models can also be applied to multiple diffusing species withing a single solvent, provided their concentrations are sufficiently low that Brownian interactions between the diffusing species are unlikely. This is the case, for example, in Chapter 3. However, for other situations, multi-component mass transport models may be more appropriate. One such model includes the Maxwell-Stefan equations, presented in Equation 1.25 [15, 125].

$$\partial_i \tilde{c}_S = \sum_{R=1}^{N_{\text{species}}} \frac{\tilde{c}_S j_{Ri} - \tilde{c}_R j_{Si}}{c_{\dagger} \mathcal{D}_{SR}} \quad (1.25)$$

where

$$\begin{aligned} S, R &= \text{indices over chemical species} \\ c_S &= \text{concentration of species } S \left[\left[\frac{\#}{\text{L}^{(N_d)}} \right] \right] \\ c_{\dagger} &= \sum_{S=1}^{N_{\text{species}}} c_S = \text{total molar density} \left[\left[\frac{\#}{\text{L}^{(N_d)}} \right] \right] \\ \tilde{c}_S &= \frac{c_S}{c_{\dagger}} = \text{unitless molar fraction of species } S \left[[1] \right] \\ \mathcal{D}_{SR} &= \text{Maxwell-Stefan diffusion coefficient for species } S \text{ and } R \left[\left[\frac{\text{L}^2}{\text{T}} \right] \right] \end{aligned}$$

For ideal gases, the Maxwell-Stefan diffusion coefficients, \mathcal{D}_{SR} , are the same as the binary Fickian diffusion coefficients. For non-ideal mixtures, this is no longer the case, as the coefficients themselves vary with concentration [15, 125].

The Maxwell-Stefan equations have been used to study systems related to those considered in Chapter 4 [54], but are not used herein.

Anomalous diffusion is another topic that requires models other than the Fickian diffusion equations in Sections 1.5 and 1.6. As noted in Section 1.7, the Fickian diffusion coefficient is related to the derivative with respect to time of the MSD of a diffusing particle. This presumes that the derivative is constant, that is, that the MSD grows linearly with time. In *anomalous diffusion*, however, the MSD grows in a nonlinear manner with respect to time, so the Fickian diffusion coefficient cannot be defined. Specifically, diffusive regimes are classified by the exponent μ in Equation 1.26 as shown in Table 1.3, taken from Balescu [9]. Applications of anomalous diffusion include plasma and fusion physics [9], the motion of a single molecule through a solid, polymer dynamics, and particles suspended in fluids subject to irregular flow [99].

$$\langle r_i r_i \rangle \propto t^{\mu} \quad (1.26)$$

Table 1.3: Anomalous diffusion regimes.

μ	Regime
$0 < \mu < 1$	Subdiffusive
$\mu = 1$	(Normal) Diffusive
$\mu > 1$	Superdiffusive

Another application of diffusion requiring different mathematical models than those considered here is found in the design of pharmaceutical agents. There, a wide variety of different mathematical models have been employed to describe the process of drug release, which refers to the delivery of a therapeutic agent to its intended location. In particular, controlled release systems are designed to maintain the concentration of the therapeutic agent at a desired level for a period of time. The mathematical models used to design such systems must account for simultaneous processes such as swelling and dissolution of solid delivery forms, and the subsequent diffusion of the therapeutic agent. Anomalous diffusion is considered in some mathematical models used in the design of these systems [21].

Chapter 2 Principal Methods

2.1 Overview

This chapter introduces the methods used to explore the mathematical models described in Chapter 1.

The techniques applicable to analyses at the atomistic and molecular scales are briefly described in Sections 2.2 and 2.3.

The diffusion equations described in Sections 1.5 and 1.6 take the form of Partial Differential Equations (PDEs). Unfortunately, analytical solutions to these equations are not available for anything but the simplest geometries. Typically, only approximate solutions are available. In particular, these approximate solutions often take the form of computer-generated numerical data, leading to the terms *numerical models* and *numerical methods*. Section 2.4 briefly reviews the Finite Element Method (FEM), which is the principal numerical method used in this work to generate approximate solutions to the PDEs described in Chapter 1.

Despite the power of the FEM, models must still be limited to fit into the memory and time constraints of available computing resources. This becomes challenging for problems spanning multiple scales of length and/or time. Multi-scaling techniques, as described in Section 1.2, allow such problems to be solved efficiently using reasonable amounts of computing resources. Details on homogenization, the primary multi-scale method used in this work, is provided in Sections 2.5 and 2.6, for periodic and stochastic systems, respectively.

2.2 Electronic Structure Calculations

As noted in Chapter 1, the mathematical model of quantum mechanics has been well-established as an accurate description of the behavior of atoms, and the relevant empirical properties are well-established. Atoms consist of electrons and nuclei, and the masses and charges of these particles, and the strength parameters of the electromagnetic interactions, have all been measured to high precision. The quantum-mechanical description of the motions of the nuclei and electrons is given by the time-dependent Schrödinger Equation, shown here in Equation 2.1 [114, 119].

$$i\hbar\partial_t|\Psi\rangle = \mathcal{H}|\Psi\rangle \tag{2.1}$$

where

$$\begin{aligned} i^2 &= -1 \\ \hbar &= \frac{h}{2\pi} \text{ [[ET]]} \\ h &= \text{Planck's Constant [[ET]]} \\ \mathcal{H} &= \text{Hamiltonian operator [[E]]} \\ |\Psi\rangle &= \text{Quantum state of the electrons and nuclei} \left[\left[L^{-\frac{Nd}{2}} \right] \right] \end{aligned}$$

The pure states, $|\Psi_n\rangle$ associated with \mathcal{H} are the eigenfunctions of \mathcal{H} from the eigenvalue equation, which is the time-independent Schrödinger Equation shown here in Equation 2.2.

$$\mathcal{H}|\Psi_n\rangle = E_n|\Psi_n\rangle \quad (2.2)$$

For a system consisting of electrons and nuclei, the Hamiltonian operator includes, in principle, the kinetic energy of each electron and each nucleus, and the potential energy from the electromagnetic interaction of each particle with each of the others, and with any externally applied electromagnetic potential. Thus, the Hamiltonian depends on the position, momentum, and spin of each particle. However, the masses of the nuclei are orders of magnitude larger than the masses of the electrons, so for typical distributions of kinetic energy, the nuclei move much more slowly; there is a natural separation in the time-scales of the nuclear and electronic motions. The separation of the Hamiltonian into nuclear and electronic motions, treating the electrons as moving around fixed nuclei, is known as the Born-Oppenheimer approximation [20, 88, 124]. The search for the ground state of the electrons, assuming nuclei at fixed positions, is known as the *electronic structure* problem. The accuracy of the Born-Oppenheimer approximation has been questioned, and attempts have been made to bypass the approximation, or correct for it in other ways [40, 91, 126]. Nonetheless, the electronic structure problem cannot be described without at least making reference to this approximation.

The electronic structure problem can be solved for isolated atoms, ions, or molecules, and in crystals consisting of atoms, ions, or molecules. Methods for solving the electronic structure problem are often called methods of *quantum chemistry*.

An oft-cited target for the level of accuracy in electronic structure calculations is such that the calculations should predict energy differences that are within the bounds of uncertainty for corresponding experimental measurements. This is often taken to be an accuracy of 1 kcal per mole for predicted energies [10, 102], which corresponds to approximately 0.04 electron-volts per particle, or, in atomic units, approximately 1.6×10^{-3} Hartrees. In practice, such a level of accuracy is not always easily achieved.

Indeed, certain types of electronic structure calculations, and related problems, have been shown to be NP-Complete [130, 131].

The difficulty of the electronic structure problem can be explained in terms of optimization problems. The electronic ground state is the wave function, Ψ that gives the minimum value for the energy (obtained by application of the Hamiltonian operator, \mathcal{H}). The wave function is itself a function of all electron positions and spins. Thus, for a system with N_{elec} electrons, the wave function is a function of $3N_{\text{elec}}$ coordinates (for three-dimensional problems), and N_{elec} spins. As the number of electrons grows rapidly with the number of atoms, the optimization problem therefore takes place within a highly multi-dimensional space.

In addition to the difficulty of the optimization problem, the electromagnetic interaction between electrons also complicates the problem. In principle, even the electrostatic potential at the location of any electron depends on the positions of

all of the other $N_{\text{elec}} - 1$ electrons. Thus, the calculations required for electrostatic interactions are of order N_{elec}^2 . Such calculations quickly become intractable, and so approximations are often required to reduce the computational burden.

Another source of difficulty in the electronic structure problem is the requirement that Ψ be anti-symmetric under the exchange of any two electrons. That is, such an exchange results in a new Ψ that differs from the prior one only with regard to a change of overall sign. This requirement is important, as without it the ground state obtained would be the ground state corresponding to bosons rather than fermions [45]. Various methods of dealing with this requirement are discussed below, but they do result in additional computational difficulty.

A wide variety of methods for finding the ground-state electronic wave function, Ψ , have been developed. These methods attempt to render the optimization problem tractable, and deal with exchange requirements, by making various approximations or assumptions. The methods briefly described herein are the Hartree-Fock (HF) and Post-HF methods, Density Functional Theory (DFT), and Quantum Monte Carlo (QMC) methods. Within these methods, different approaches for evaluating electrostatic interactions are also possible.

In the HF method, the ground state is approximated by a Slater determinant of single-particle wave functions [20, 88]. The set of single-particle functions from which the determinant is constructed is called the *basis set* of functions. A variety of different basis sets have been developed. The nature of the determinant ensures that the overall wave function is antisymmetric under the exchange of any two electrons. HF is a variational procedure: the Slater determinant of the selected basis set is the variational form. The HF procedure obtains the Slater determinant that minimizes the ground state energy. The energy thus obtained is an upper bound for the ground state energy. The variational form which produces the lowest upper bound produces the most accurate estimate of the ground state energy. In general, the approximation can be improved by using larger basis sets.

While the HF method ensures that the wave function will be antisymmetric under exchange of particles, the use of only linear combinations single-particle wave functions prevents correlation between different electrons. Indeed, the *correlation energy* is defined as the difference between the exact energy and the HF energy in the limit of a very large basis set [88, 124]. Various methods have been derived to resolve this issue, by approximating the correlation energy. As these methods begin from the HF approximation, they are broadly termed Post-HF methods. However, these methods can differ from HF in significant ways other than just the quantitative results they produce. Some of these approaches, such as Configuration Interaction and Coupled Cluster, use not just a single Slater determinant as the approximation to the ground state, but rather a sum of such determinants. Other approaches, such as Møller-Plesset Perturbation Theory, treat the difference between the operator which is exactly solved by HF and the actual Hamiltonian as a perturbation. Hybrids of these approaches also exist, leading to a wide variety of Post-HF methods, explained in further detail in references such as Cramer [33] and Szabo and Ostlund [124].

DFT grew out of efforts to develop quantum mechanics in terms of the number density of the electrons rather than a many-body wave function. Hohenberg and

Kohn [58] demonstrated that the ground state energy of an electron gas is a unique functional of the number density function. (The demonstration would seem to work only for scalar potentials.) The electron density that minimizes the energy is the density of true ground state. Kohn and Sham [76] developed a procedure for using this functional to approximate the ground state. The dependence on the density functional providing the energy is the source of the name for this method.

In the Kohn-Sham approach, the electron density is found as the sum of single particle densities. This converts the many-body quantum mechanics problem to a set of single particle equations, and a self-consistency requirement. This approximation is easily extended to include spin polarization. In solids, Bloch's theorem can be applied, meaning that the electron density has the same periodicity as the lattice, and so the Kohn-Sham Hamiltonian will as well. This property can be exploited for DFT in a way that it cannot be in HF [121].

A practical form of the exact energy functional has never been found; DFT calculations make use of approximate energy functionals instead [100, 113]. Nonetheless, DFT has been developed into a highly accurate and efficient means of solving the electronic structure problem for a wide variety of cases [33]. One notable reason for this efficiency is that while the many-body wave function is in principle a function of $N_{\text{elec}}N_d$ spatial coordinates, the electron number density is only a function of N_d spatial coordinates. This is a tremendous dimensional simplification.

QMC is a developing approach to the electronic structure problem. This method is thoroughly reviewed in Foulkes et al. [46]. As the name suggests, the method uses random sampling to evaluate integrals. Because of the central limit theorem, the accuracy of such an approximation improves as sampling points are added, without regard to the number of dimensions over which the integral is taken. In highly multi-dimensional spaces such as many-body wavefunctions, this is a significant advantage over integration methods based on quadrature, where the number of sampling points grows rapidly as the spacing diminishes in all the dimensions. The main obstacle to QMC methods, though, is the anti-symmetry requirement for fermions. Without imposing this requirement, the method would tend toward the boson ground state rather than the fermion ground state [45]. This gives rise to the *sign problem*, which is usually resolved by assuming a nodal hypersurface for the wave function. The method is variational with regard to this assumed surface [25]. However, the nodal hypersurface can be highly complex [27, 77], which poses difficulties for the QMC approach.

2.3 Molecular Simulations

At the scale of length and time above the electronic structure problem, individual atoms or ions become the smallest unit of consideration. The electronic structure creates forces acting on these atoms or ions, and other forces are generated by long-range electrostatic interactions, and collisions between molecules. These forces, of course, vary with the positions of the atoms and ions, resulting in a dynamic system where forces, velocities, and positions all vary over time in highly complex ways. Two important simulation methodologies for this scale are MD and molecular Monte

Carlo (MC). In both of these approaches, individual atoms or ions (or *particles*) are subjected to classical forces, including forces arising from the underlying electronic structure.

In MD, the equations of motion for the particles in the system are integrated over time, using discrete steps of time and various numerical integration techniques. The resulting record of particle positions and velocities over time is known as the *trajectory* of the system. In contrast, MC does not involve the integration of equations of motion over time. Instead, this approach evaluates integrals over the system phase space (or subspaces thereof) using an approach based on the Metropolis algorithm [33, 89]. Where applicable, this approach can be highly efficient, as it systematically probes the regions of phase space that contribute most to the resulting integral [47].

The forces due to electronic structure in MD and MC simulations are often represented by *force fields*. These are equations representing the force (or potential energy) experienced by one particle based on its position relative to one or more other particles. These forces are not exclusively associated with the covalent bonds present within a given molecule, but can include other short-range inter-molecular interactions as well. Long-range interactions are not usually included in the force field. Forces can be defined in terms of bond distance, bond angles, bond torsion, and combinations thereof. The effect of van der Waals interactions (also known as London forces, or dispersion forces) can also be included in these equations [33]. The equation forms and parameters for these forces are tabulated and published, and are often incorporated into MD software packages. One of the key ideas to this approach is *transferability*: the force parameters that apply to a bond in one molecule apply also to the same bond in different molecules [33]. In practice, a variety of different force fields have been derived for various types of molecules or crystals; a truly universal force field has not been found. Furthermore, this approach generally requires that the electronic structure remain constant throughout the simulation, or that anticipated changes in the electronic structure are included in the force field in advance. This poses difficulties when attempting to simulate systems involving chemical reactions.

While the force field in a molecular simulation includes the effects of the electronic structure on short-range interactions, long-range interactions between the atoms or ions, such as electrostatic force, must be evaluated separately. This portion of the simulation can be very computationally demanding. Naively, the calculation of the electrostatic force on a single ion in a molecular simulation would require computing the pairwise interaction with every other ion. Computing the electrostatic forces for all ions in this way would require the evaluation of a number of pairwise interactions growing as the square of the number of ions. Clearly, for simulations with large numbers of ions, a more computationally efficient approach, with better scaling behavior, must be used. One of the simplest such approaches is to simply truncate the evaluation of the pairwise interactions at a selected cutoff distance. The electrostatic forces from distances beyond this cutoff distance are thereby approximated as zero, which can lead to serious errors in some cases. More sophisticated approaches are available such as Ewald summation, fast multipole methods, and particle-mesh methods including Particle Mesh Ewald (PME) [47].

Many chemical systems, especially in biochemistry applications, are aqueous sys-

tems. Simulations of such systems will therefore include large numbers of water molecules. For this reason, the accuracy and efficiency of water molecules in the simulation is of particular importance. A variety of published water models are available to address these concerns. Many non-aqueous systems will include a solvent other than water, where attention to the model of this solvent will be of similar importance.

Because any system of interest will likely include large numbers of atoms, measuring the statistical properties of the system becomes important. That is, the results of MD and MC simulations are often expressed in terms of system averages (often representing ensemble averages), and fluctuations around those averages. The pre-processing and post-processing of MD and MC results therefore often involve considerations from statistical mechanics. In MD, ergodicity is often assumed; ensemble averages are approximated by taking averages over the system trajectory.

In particular, simulations are often desired under conditions of statistical ensembles defined by Number, Volume, and Temperature (NVT) or Number, Pressure, and Temperature (NPT), rather than strictly Number, Volume, and Energy (NVE). This means that computational *thermostats* and *barostats* must be employed, to allow statistically appropriate variations in the total energy or total volume of the simulation.

2.4 The Finite Element Method

The Finite Element Method is a means of approximating the unknown solution to a PDEs with a finite set of unknown variables. This type of procedure is commonly known as *discretization*, as the problem is converted from a search for a function to a search for discrete values. Other discretization methods, such as the Finite Difference Method [28], are also often employed for these types of problems. Indeed, the Finite Difference Method is often used for the discretization of time in time-dependent problems.

The Finite Element Method has attained widespread use as a numerical modeling tool, with a wide variety of commercial and public software packages providing implementations. Introductory texts include Hughes [60] and Reddy [107]. A complete survey of the method could fill multiple volumes, as the literature describing its details and variations is vast. However, some key points about the method are needed for an understanding of how it is applied to the PDEs of Chapter 1.

Many FEM software packages are capable of solving only the PDEs defined within their code. Such programs cannot solve user-defined PDEs. In contrast, the FEM software package used in this work has no pre-defined equations for solution, but instead allows users to enter equations in a symbolic format. The required form of the equation is not the differential form of the equations presented in Chapter 1. Instead, the required form is an integral form often called the *weak* or *variational form*. Consequently, the PDEs of Chapter 1 must be converted to this form.

For a given PDE, the FEM approximates the solution in the form

$$\tilde{u}(x_i) = \sum_{M=1}^{N_{\text{dof}}} c_M \phi_M(x_i) \tag{2.3}$$

where

$$\begin{aligned}
i &= \text{index over the spatial dimensions} \\
x_i &= \text{spatial coordinate vector} \\
\phi_M(x_i) &= \text{known interpolation functions} \\
M &= \text{index over the interpolation functions} \\
N_{\text{dof}} &= \text{number of interpolation functions used} \\
c_M &= \text{unknown coefficients}
\end{aligned}$$

Because the interpolating functions $\phi_M(x_i)$ are known in advance, this approximation converts the problem of finding an unknown function into the problem of finding unknown constants. Solving for N_{dof} unknowns requires a system of N_{dof} algebraic equations, and so the unknown constants are the degrees of freedom in this algebraic system.

There are various methods for deriving the system of algebraic equations for the FEM. One such approach is the Galerkin Method of Weighted Residuals, which employs the calculus of variations. The following discussion illustrates this method for a linear PDE.

Consider an arbitrary linear differential operator \mathcal{A} and known function f in the PDE

$$\mathcal{A}u(x_i) = f \tag{2.4}$$

which can also be written as $\mathcal{A}u(x_i) - f = 0$. This latter form is multiplied by an arbitrary *test function*, $v(x_i)$, and integrated over the problem domain (Ω), to obtain

$$\int_{\Omega} d\Omega [\mathcal{A}u(x_i) - f] v(x_i) = 0 \tag{2.5}$$

By the fundamental lemma of variational calculus, this integral equation can only be true if the term in square brackets is zero everywhere within the problem domain. This allows the PDE to be recovered directly from the integral form. Thus, the integral form of the equation is effectively equivalent to the PDE form. Often, additional algebraic manipulations of the integral are also possible. Integration by parts is frequently performed to reduce the order of the differential operator applied to $u(x_i)$, at the cost of applying a differential operation to $v(x_i)$ as well. The integral equation then requires a lower order of derivatives than the PDE, reducing the continuity requirements on the unknown function. For this reason, the integral form may be called the *weak form*: the continuity requirements have been weakened.

Substitution of the FEM approximation of the solution, $\tilde{u}(x_i)$ (Equation 2.3), into the PDE will result in a residual error defined as

$$R(x_i) = \mathcal{A}\tilde{u}(x_i) - f \tag{2.6}$$

The weak form in Equation 2.5 can then be written as

$$\int_{\Omega} d\Omega R(x_i)v(x_i) = 0 \tag{2.7}$$

The N_{dof} equations needed to solve for the N_{dof} unknowns are provided by selecting N_{dof} specific test functions, $v_L(x_i)$. The N_{dof} equations thus obtained are of the form:

$$\sum_{M=1}^{N_{\text{dof}}} c_M \int_{\Omega} d\Omega (\mathcal{A}\phi_M(x_i)) v_L(x_i) = \int_{\Omega} d\Omega f v_L(x_i) \quad (2.8)$$

Defining the matrix element A_{LM} as

$$A_{LM} = \int_{\Omega} d\Omega (\mathcal{A}\phi_M(x_i)) v_L(x_i) \quad (2.9)$$

and the vector element b_L as

$$b_L = \int_{\Omega} d\Omega f v_L(x_i) \quad (2.10)$$

the system of algebraic equations becomes

$$A_{LM} c_M = b_L \quad (2.11)$$

with implied summation over repeated indices, even though the indices are for the algebraic degrees of freedom rather than spatial dimensions.

A similar procedure can be applied to nonlinear PDEs, but the resulting system of algebraic equations will be nonlinear as well.

Finally, note that a given differential equation has a family of solutions. Choosing a unique solution from this set requires the application of appropriate conditions on the boundary of the problem domain. There are two forms of these boundary conditions that are most commonly encountered. *Dirichlet* boundary conditions require the unknown function to take on a specified value over some portion of the domain boundary. In contrast, *Neumann* boundary conditions require the gradient of the unknown function to take on a vector value that is perpendicular to the domain boundary, and is also of specified magnitude. Other types of boundary conditions do exist, and in fact are used within this work. Regardless of the classification, boundary conditions must be expressed mathematically before they can be applied to the problem.

There are two different ways in which boundary conditions are specified within the FEM. *Natural* boundary conditions are those which must be included within the weak form, while *essential* boundary conditions are those which must be explicitly imposed on the approximate solution, $\tilde{u}(x_i)$ [107, 60]. In many cases examined herein, Dirichlet boundary conditions will be essential boundary conditions, and Neumann boundary conditions will be natural boundary conditions. However, situations where this association is reversed can also be derived.

Weak forms for the PDEs of Chapter 1 are presented in Appendix D, Section D.2.

2.5 Periodic Homogenization

Homogenization is a multi-scaling (or *coarse-graining*) technique based on asymptotic expansion. This form of expansion is similar to perturbation theory, as applied in

quantum mechanics, for example. Homogenization consists of a formal procedure described in Auriault et al. [7], Bensoussan et al. [12], and Zhikov et al. [134], which can be applied to any PDE defined on regular lattice of unit cells. The procedure transforms the PDE into a *corrector problem* which is solved on the unit cell, or Representative Elementary Volume (REV). Solution of the corrector problem, with periodic boundary conditions, yields the *corrector function*, χ_j . An integral of the corrector function over the REV yields the effective value of the desired property at the next larger scale of analysis. For sufficiently complex situations, the corrector problem may require FEM analysis.

One key aspect of the homogenization procedure is that it requires adequate separation of the length scales. This requirement is quantified by defining characteristic length scales ℓ_c and L_c for the smaller and larger scales of the analysis, respectively. The separation of scales is expressed as their ratio $\epsilon \equiv \frac{\ell_c}{L_c}$. For well-separated scales, $\epsilon \ll 1$. That is, the characteristic length for the larger scale should be much larger than the characteristic length appropriate for the REV.

The corrector problem for a particular PDE can be obtained from an asymptotic analysis by expanding in powers of ϵ . This is accomplished by expressing the spatial variable in the PDE as two separate variables, one corresponding to the larger scale and the other corresponding to the smaller scale. For example, consider x as a coordinate measured in units of meters, and y as a coordinate in the same direction but measured in units of nanometers. These variables are related by the scale separation parameter, ϵ , allowing the asymptotic expansion of the PDE to be performed. This process is applied to Fickian diffusion in Appendix D, Section D.3, following the results in Bensoussan et al. [12]. The corrector problem and the integral over the REV are repeated here as Equations 2.12 and 2.13, respectively.

$$\partial_i (D_{ik} \partial_k \chi_j) = \partial_i D_{ij} \quad (2.12)$$

$$D_{ij}^{\text{eff}} = \frac{1}{|\Omega|} \int_{\Omega} d\Omega (D_{ij} - D_{ik} \partial_k \chi_j) \quad (2.13)$$

The boundary conditions for the corrector problem of Equation 2.12 are that χ_j must be periodic, with period matching the unit cell [12]. These boundary conditions only determine the corrector function up to an additive constant. Such constants have no effect on the effective diffusion coefficient, as Equation 2.13 depends on the derivatives of the corrector function rather than its actual values.

The weak form of the corrector problem in Equation 2.12 is developed in Appendix D, Section D.4. This allows for calculation of the effective diffusion coefficient using the FEM described in Section 2.4.

Simple example problems that can be solved analytically both with and without the use of homogenization theory are demonstrated in Appendix D, Sections D.5 and D.6.

A similar procedure for finding the effective diffusion coefficient in porous media, with the local diffusion coefficient constant within the pores, was derived in Chapter V of Cushman [36], without directly using homogenization theory. A rigorous spa-

tial averaging approach was used instead, resulting in an auxiliary PDE that must be solved for a vector-valued function, which is then used in an integral over the unit cell to obtain the effective diffusion coefficient. The results for idealized two-dimensional unit cell geometries were also compared to various experimental data and the results of alternative theories. The approach that is similar to homogenization theory performed well in that comparison.

As noted in Section 1.7, the diffusion coefficient matrix is generally symmetric. However, Equation 2.13 is not guaranteed to produce a symmetric result. This is demonstrated in Appendix D, Section D.7. An asymmetric diffusion coefficient matrix poses additional challenges for interpretation and application of results. In particular, the matrix can no longer be diagonalized, meaning that a coordinate system aligning with the principal axes does not exist. Further discussion of this issue and possible resolutions can be found in Zijl [135]. However, because the homogenization procedure is an approximate method, the asymmetry of the matrix may simply be neglected in some cases.

The homogenization procedure described above is based on the assumption that the medium is an infinite, periodic repetition of the REV. Media with random structure would therefore be excluded from this treatment. As pointed out in Auriault et al. [7], sufficient separation of scales can sometimes allow random media to be approximated as periodic media. In general, though, the presence of non-periodic geometry, such as random defects in a regular structure, must be treated with a different approach. Such an approach is introduced in Section 2.6.

2.6 Stochastic Homogenization

Very few materials actually consist of a single unit cell that repeats perfectly and indefinitely without alteration. Instead, most materials contain defects, domain boundaries, and similar spatial variations. Such variations include *point defects*, where an atom or small group of atoms is displaced, or replaced, within a unit cell. Other types of variations, such as dislocations or grain boundaries, may be linear or two-dimensional. Indeed, there are many ways in which a periodic structure can be altered. Further examples and classifications of these variations can be found in sources such as Callister and Rethwisch [26].

The periodic homogenization approach from Section 2.5 can be extended or modified to properly account for random variations within an otherwise periodic structure. Such extensions are usually termed *stochastic homogenization*. This section briefly introduces some stochastic homogenization approaches.

The most obvious approach is to expand the REV from a single unit cell to multiple unit cells, with the random variations included. That is, the defects, boundaries, and other variations should be present in the REV with the correct spatial distribution. In such an approach, the REV must theoretically contain an infinite number of cells [4, 3], in order to account for even the most rare of possible variations. In practice, this approach involves creating a *supercell* containing many unit cells, but not an infinite number. The random variations are included by random generation of the supercell. To properly account for low-probability defects, either the supercell must

be very large, or multiple realizations of the supercell are required, using a Monte-Carlo approach. Computationally, there is a time-memory tradeoff between the size of the supercell and the number of randomly generated supercells required: larger supercells require fewer random trials, but also require more memory to complete a single calculation.

Fortunately, a more computationally efficient approach is available in some cases. When the structure to be analyzed is very nearly periodic, the deviations can be considered as a perturbation of the structure. This is most clearly demonstrated for the case of point defects. Consider a structure where there is some probability η for any given unit cell to contain a point defect. Thus, on average, the fraction of the unit cells containing a defect is η , and the fraction of cells that do not contain a defect is $1 - \eta$. The structure is nearly periodic when η is small. This lends itself to an asymptotic expansion in η . The effective diffusion coefficient is expressed as a polynomial in η , and usually truncated at first or second order. This is shown in Equation 2.14.

$$D_{\text{eff}} = D_0 + \eta D_1 + \eta^2 D_2 + \dots \quad (2.14)$$

The calculation of the terms in Equation 2.14 is explained mathematically in Anantharaman and Le Bris [4]. Briefly, a functional description is provided here. The zeroth-order term in the expansion, D_0 , is the result from periodic homogenization. That is, the corrector problem of Equation 2.12 is solved for a single unit cell without the defect, and the integral of Equation 2.13 is then performed to obtain D_0 . No supercell is needed for D_0 . The first-order term requires the solution for a single supercell, with one of the unit cells containing the defect. The corrector problem is solved, and the integral is performed, using the supercell as the REV, to obtain D_1 . The second-order term involves solving the problem for a number of supercells, but these supercells are constructed deterministically rather than stochastically. Specifically, each supercell must contain exactly two defective unit cells, with one as the unit cell at the center of the supercell. The second defect is located in a different unit cell within each realization of the supercell, with one realization for each possible location. Thus, the number of supercells grows with the supercell size. The corrector problem is solved for each supercell, and the integral is calculated separately for each supercell as well. The average of the results for the supercells is used as D_2 . Clearly, extending this procedure to third-order would involve an even larger number of supercells, such that the computational efficiency of the Monte-Carlo approach might become competitive again.

Note that in this asymptotic approach, the defect probability, η , enters into the results only in Equation 2.14. Each supercell problem is completely deterministic. Additionally, the asymptotic approach matches the exact result in the limit of large supercell size.

An alternative approach to an asymptotic series for nearly periodic structures is presented in Costaouec [30]. While this alternative asymptotic expansion may be more effective in particular cases, in general the two approaches would be expected to perform similarly.

Surprisingly, there is a stochastic homogenization problem for which an analytical solution is available, making it a useful case for validation of numerical approaches. This case is known as the *random checkerboard*. The problem domain consists of a square tiling of the plane, with each square assigned one of two isotropic diffusion coefficients, with equal probability. In this case, the effective diffusion coefficient is the geometric mean of the two diffusion coefficient values [3, 134].

Chapter 3 Sequential Enzymes in a Nanoscale Domain

3.1 Background

Biochemical systems do not involve “materials” in a traditional sense, but are relevant to the discussion of mass transport properties because of the key role that diffusion processes play in the phenomenon of *signal transduction*. Living cells use a highly complex network of biochemical signals to function and adapt to changes in their environment. In a typical such process, a ligand molecule in the medium surrounding the cell interacts with a receptor on the cellular membrane. This interaction results in changes in the receptor structure that can be detected inside the cell by *second messenger* molecules. These molecules disperse from the receptor through diffusion, and may undergo, or influence, reactions inside the cell, potentially changing concentrations of other biochemicals, which also diffuse through the cytosol. The complete system of all such reactions, from the membrane receptors to alterations in the cellular behavior, is known as a signal transduction pathway. Diffusion is the mechanism by which these pathways transmit information from one spatial location to another.

The rate at which a biochemical signal can be transmitted through a system depends on both the transport properties of the chemical species involved, and the rates at which the necessary reactions take place. Signal transduction pathways can therefore be modeled as reaction-diffusion systems. In such systems, the reaction rate coefficients and effective diffusion coefficients are behavioral properties.

The reaction-diffusion processes taking place in signal transduction pathways take place in the spaces within and between cells. The geometry of these regions, confined by cellular membranes and also occupied by other proteins, enzymes, and organelles, can affect the kinetics of the reaction-diffusion processes. In particular, the diffusion portion of the process can sometimes be the rate-determining step.

This chapter develops a model for steps in a signal transduction process that can be used to investigate the kinetics of diffusion-limited reactions. The model is developed in a series of steps, starting with a relatively simple model and then increasing in complexity. This model generally follows the work of Kekenés-Huskey et al. [68], Setny et al. [118], Kekenés-Huskey et al. [70], Kekenés-Huskey et al. [69], and Kekenés-Huskey et al. [71].

3.2 Geometry of a Nanoporous Membrane

A nanoporous membrane was selected as the basic geometry to be used for this study. This geometry consists of a thin membrane separating two fluid reservoirs. Each reservoir contains the solute of interest at a given concentration level, which is assumed to be generally uniform at sufficient distance from the membrane. When the solute concentration in one reservoir is higher than the other, a concentration gradient is established across the membrane. Nano-scale pores through the membrane allow transport of the solute from the higher-concentration reservoir to the lower-

concentration reservoir. This geometry was selected because, while relatively simple, it can be adapted to represent confined interstitial spaces present within biological or biomimetic systems.

The nanoporous membrane geometry can be represented in either two dimensions, as shown in Figure 3.1, or three dimensions, as shown in Figure 3.2. In two dimensions, the pores are slit-like, and the porosity of the membrane is controlled by the pore width and spacing between them. In three dimensions, the pore shape can also be varied; cylindrical pores were selected here. The membrane porosity in this situation is controlled not only by the pore radius, but also by the pattern in which the pores are placed on the membrane surface. Here, the pores are located on a body-centered rectangular lattice.

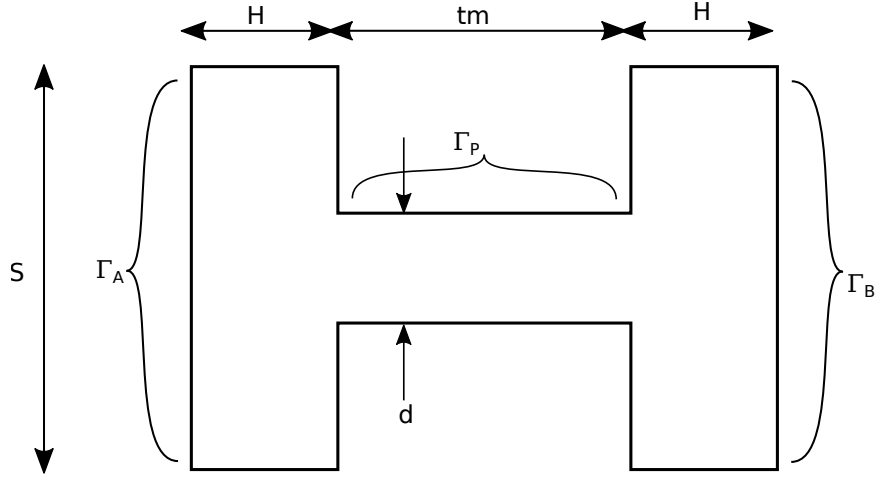


Figure 3.1: Two-dimensional geometry for a nanopore. When repeated periodically, the system becomes a stack of obstructive layers separated by slit-like pores.

The geometric variables and model boundary domains shown in Figure 3.1 are:

- H = Distance between membrane surface and model boundary $[[L]]$
- tm = Membrane thickness $[[L]]$
- d = Pore thickness $[[L]]$
- Γ_A = Model boundary surface A
- Γ_B = Model boundary surface B
- Γ_P = Model boundary surface inside pore

The geometric variables shown in Figure 3.2 are:

- H = Distance between membrane surface and model boundary $[[L]]$
- tm = Membrane thickness $[[L]]$
- R = Pore radius $[[L]]$
- Sx = Unit cell size in x -direction $[[L]]$
- Lx = Half of unit cell size, for symmetric models $[[L]]$
- Sy = Unit cell size in y -direction $[[L]]$
- Ly = Half of unit cell size, for symmetric models $[[L]]$

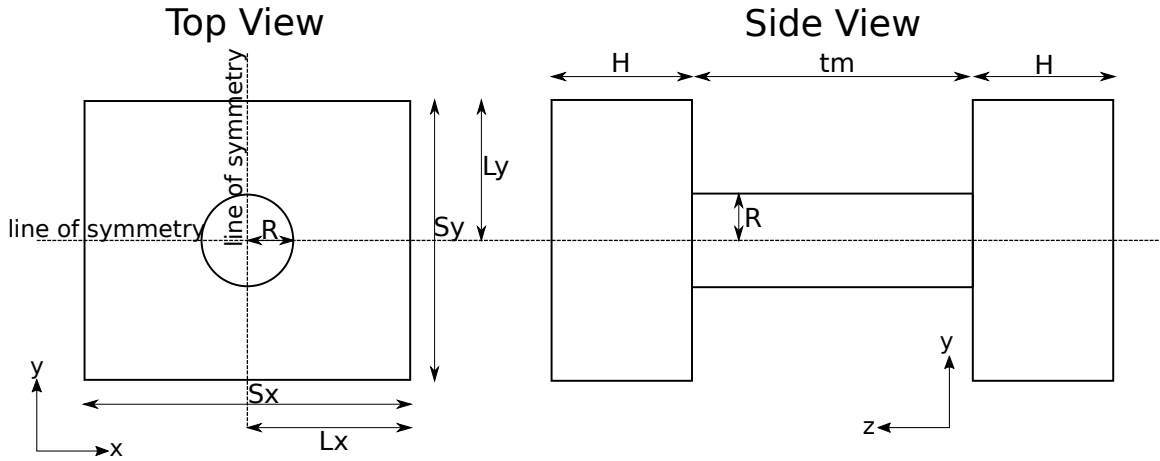


Figure 3.2: Three-dimensional geometry for a cylindrical nanopore. The pores through the obstructive material are arranged on a body-centered lattice.

The two-dimensional model is symmetric about the centerline of the pore. This line of symmetry could be used to reduce the finite element mesh to half of the unit cell, by applying a zero-flux boundary condition along the line of symmetry. Similarly, the three-dimensional model has two planes of symmetry. These can be used to reduce the finite element mesh to one quarter of the unit cell, by applying a zero-flux boundary condition on both planes of symmetry. In Section 3.5, inclusions that can break the symmetry are introduced, requiring the mesh to represent the entire model.

Figure 3.3 shows a finite element mesh for three-dimensional nanopore geometry. The mesh includes a portion the reservoirs, as the concentration will vary in the reservoir space close to the membrane. The reservoir space provided is adequate when additional reservoir space does not affect the concentration gradient within the pore. Both planes of symmetry are used, so only one quarter of the unit cell is included in the model.

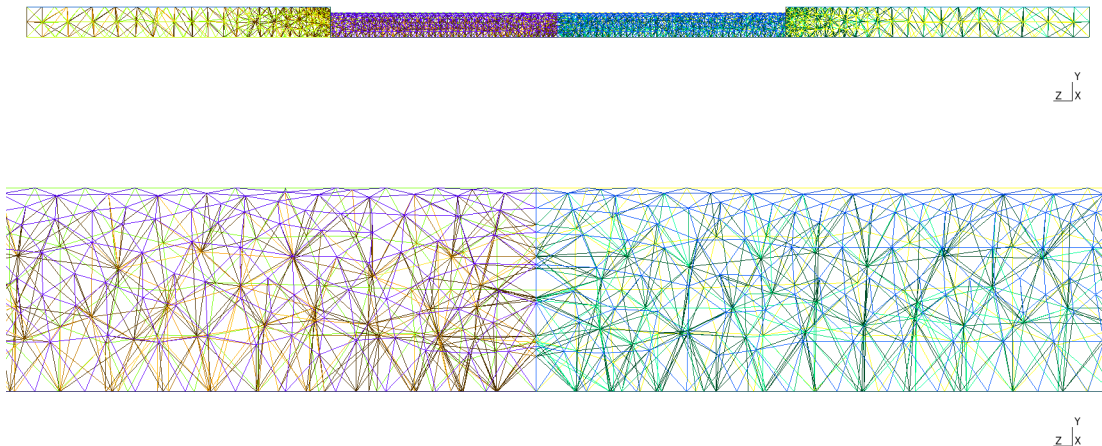


Figure 3.3: Three-dimensional finite element mesh for nanoscale pore between reservoirs. Upper image: full mesh, including reservoirs. Lower image: view showing center of pore. Both planes of symmetry are used, so only one quarter of the unit cell is included. For the pore geometry shown, $\phi = 0.5$. In these views, the mesh elements are transparent, and element edges are colored by region.

3.3 Fickian Diffusion in a Nanoscale Pore

The Fickian diffusion equation was solved for the nanoporous membrane model described in Section 3.2 under boundary conditions that imposed a concentration gradient across the membrane. A concentration of 5 particles/nm³ was applied to the model boundary in one reservoir, and a concentration of 1 particle/nm³ was applied at the opposite reservoir. These concentrations are higher than would be found for many solutes of interest in biological systems, and are only used here as a demonstration of the model. For comparison, 1 particle/nm³ is 1.661 mol/L.

The finite element model was constructed and solved in FEniCS using second-order polynomial elements. An example concentration solution field is shown in Figure 3.4.

The simulation was repeated for a number of different membrane geometries. Specifically, the simulations were run with membrane thickness values of 25 nm and 75 nm, with pore radius values ranging from 0.5 nm to 11.5 nm in steps of 0.5 nm. The five unit cell geometries used are presented in Table 3.1. Two different sets of concentration boundary conditions were also applied, with a concentration of either 5 particles/nm³ or 10 particles/nm³ for one reservoir, and 1 particle/nm³ at the other. In total, 236 different variations of the model were simulated. Two example concentration profiles are shown in Figure 3.5. Note that the solute concentration values used in these simulations are much higher than would be typical for biochemical systems. These concentrations were selected for the simulation only for demonstration purposes. In fact, because the Fickian diffusion equation is linear, the concentration values could be reduced by a constant scale factor and remain a valid solution.

For sufficiently simple geometries, the effective diffusion coefficient can be obtained from analysis of the concentration field obtained by solving the Fickian diffusion

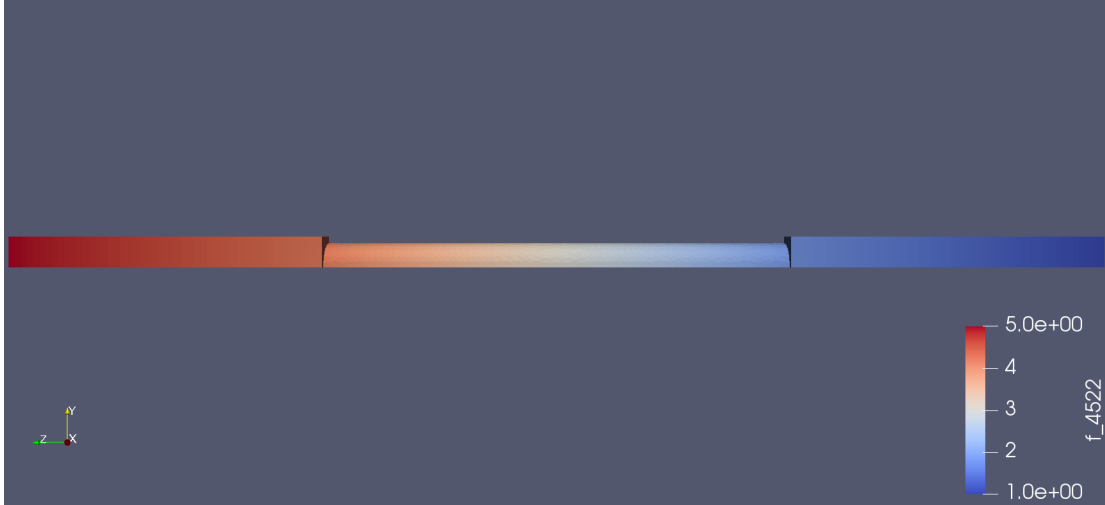


Figure 3.4: Concentration field from solution of steady-state Fickian diffusion, for a simulation with $\phi = 0.5$. The model uses both planes of symmetry, so only one quarter of the pore and reservoirs are shown. The concentration boundary conditions are 5 particles/nm³ at the end of the upper reservoir, and 1 particle/nm³ at the end of the lower reservoir. The concentration gradient extends beyond the pores into the reservoirs, illustrating the need for including the reservoirs in the finite element model.

Table 3.1: Unit cell geometries for the parametric variations of the nanoporous membrane.

Variation	L_x	L_y
1	12 nm	12 nm
2	24 nm	6 nm
3	36 nm	4 nm
4	5 nm	5 nm
5	10 nm	5 nm

problem. Details of this procedure are provided in Appendix D, Section D.8. This procedure was applied to the nanoporous membrane system, to estimate the effective diffusion coefficient of the membrane for each parametric variation of the model. The results are plotted against the porosity of the membrane in Figure 3.6. The porosity was taken as the ratio of the area of the circular pore to the area of the membrane in a unit cell: $\phi = \frac{\pi R^2}{S_x S_y}$.

The results of Figure 3.6 show that, for this simple model, the porosity is all that is needed to predict the effective diffusion coefficient, as the dimensionless ratio of the effective diffusion coefficient to the diffusion coefficient in bulk fluid is identical to the dimensionless porosity. This result owes entirely to the simplicity of the geometry and the diffusion process modeled in these simulations. In comparison to Equation 1.19, the effective porosity in this case is identical to the real porosity of the membrane, and the tortuosity and constrictivity are both equal to 1. This result demonstrates

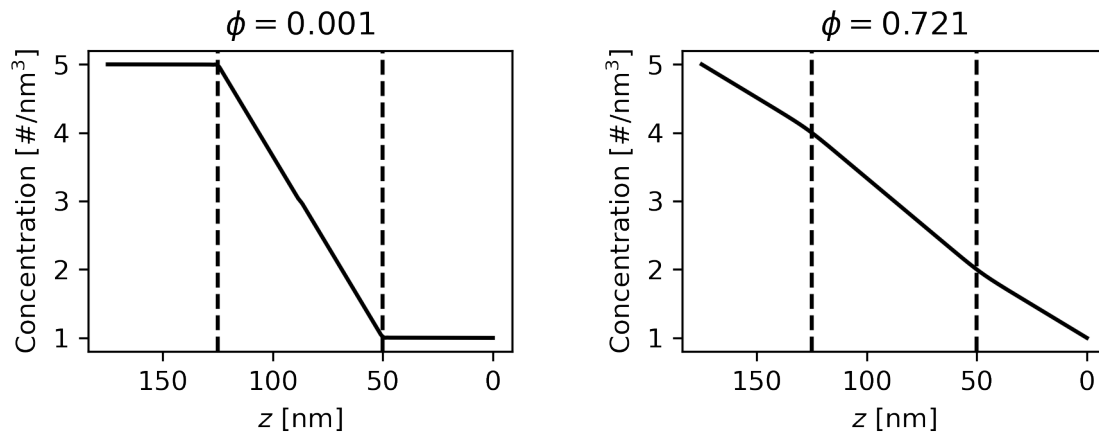


Figure 3.5: Concentration profiles along pore centerline. Solid lines show the concentration as a function of z , and the dashed lines show the limits of the pore. Left panel: low porosity (ϕ -value). Right panel: high porosity. In both cases, the concentration boundary conditions are 5 particles/nm³ at $z = 175$ nm and 1 particle/nm³ at $z = 0$ nm.

that the model can reproduce the results that are predicted by an empirically-derived relationship. The model is therefore suitable as a basis for incorporating additional complexities, such as the electrostatic interactions incorporated in Section 3.4.

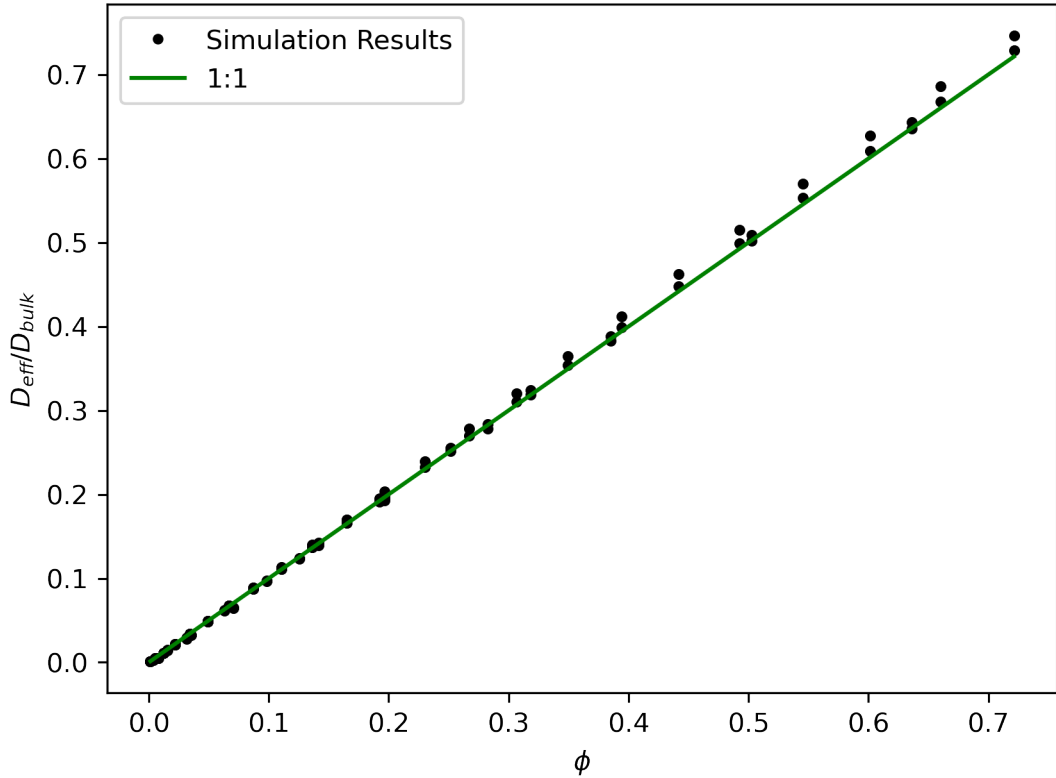


Figure 3.6: Influence of porosity on the effective diffusion ratio.

3.4 Electro-diffusion in a Nanoscale Pore

In this section, electrostatic interactions are added to the diffusion model of Section 3.3. Specifically, the purpose is to employ the Smoluchowski diffusion equation presented in Section 1.6 to the nanoporous membrane described in Section 3.2, with an electrostatic potential. To this end, the diffusing solute is assumed to carry an electrostatic charge. The solvent itself maybe electrolytic and capable of screening the charge of the diffusing species. Provided that the total concentration of the diffusing species is sufficiently low, changes in its spatial distribution may be assumed to have negligible effect on the electrostatic potential. This electrostatic potential is governed by the Poisson equation, subject to the boundary conditions of the problem. If a Boltzmann distribution of charge is assumed, the nonlinear Poisson-Boltzmann equation can be used to obtain the electrostatic potential [64]. Expanding this nonlinear equation in terms of the potential, and keeping only the first-order term results in the Linearized Poisson-Boltzmann (LPB) equation, shown here in Equation 3.1 [87].

$$\partial_i \partial_i \Phi = \kappa^2 \Phi \quad (3.1)$$

κ is a constant that depends on the ionic strength in the solute. The LPB equation can also be expressed in terms of the Debye length, λ_D , which is the inverse of κ .

For situations where the concentration of the diffusing species can affect the electrostatic potential, the fully coupled Poisson-Nernst-Planck system of equations would need to be solved instead, as presented in Section 1.6. Here, applications will be limited to cases where the LPB equation remains valid. Thus, Equation 3.1 is first solved for the electrostatic potential under the imposed boundary conditions, followed by solution of the Slotboom-transformed steady-state Smoluchowski equation shown in Equation 3.2.

$$\partial_i (\bar{D}_{ij} \partial_j \bar{c}) = 0 \quad (3.2)$$

Figure 3.7 illustrates an example potential resulting from the solution of the LPB equation for the nanoporous membrane model. In this simulation, a potential of 25 mV was applied to the cylindrical surface within the pore and the external membrane surfaces as well. The figure clearly shows the electrostatic screening of the potential.

Figure 3.8 shows an example concentration field resulting from the solution of the Smoluchowski equation, under the same potential field illustrated in Figure 3.7. In this case, the electrostatic interaction between the membrane and the diffusing species is repulsive. The effect of this repulsion can be seen by comparing with the concentration field of Figure 3.4. In fact, near the down-gradient end of the pore the model contains a region where the concentration is even lower than the concentration boundary condition for the lower reservoir.



Figure 3.7: Electric potential from the solution of the Linearized Poisson-Boltzmann equation. The model uses both planes of symmetry, so only one quarter of the pore and reservoirs are shown. The electric potential boundary conditions are 25 mV at the membrane surfaces.

The solutions shown in Figures 3.7 and 3.8 are plotted in Figures 3.9 and 3.10 as functions of distance along the pore centerline and radial distance from the pore center, respectively.

In Figure 3.9, the solution of \bar{c} resembles the solution of c from Figure 3.5, as expected given the mathematical similarity of their respective governing equations. Also, because \bar{D} is constant, \bar{D} depends only on the potential. This inverse relationship between \bar{D} and the potential can be seen by comparing their plots in Figure 3.9. The plot of the electrostatic potential shows that, within the pore, the potential

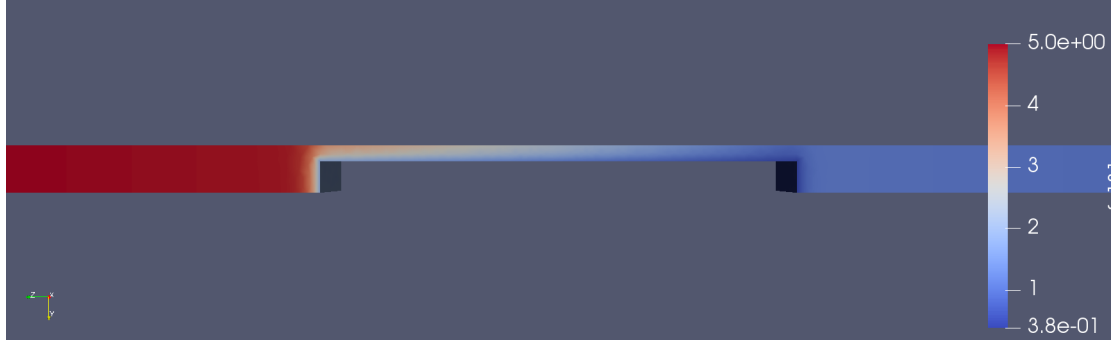


Figure 3.8: Concentration field from solution of the Smoluchowski Equation. The model uses both planes of symmetry, so only one quarter of the pore and reservoirs are shown. The electrostatic interaction between the diffusing species and the pore is repulsive. The concentration at the down-gradient end of the pore is lower than in the corresponding reservoir.

remains relatively constant at less than 8 mV at the pore center, in contrast to the 25 mV boundary condition at the pore surface. Finally, the plot of \bar{c} illustrates the effect of the electrostatic barrier on the concentration within the pore, and shows how the concentration at the down-gradient end of the pore is lower than in the adjacent reservoir.

In Figure 3.10, the solution functions were computed at varying radial distances, for a plane midway between the reservoirs. These results were generally found to be radially symmetric within the pore, such that there was little to no variation with respect to the polar angle. The value of \bar{c} is constant with respect to radial distance, and \bar{D} once again depends only on the potential. The variation of the concentration with respect to radial distance is much less pronounced than with respect to distance along the pore. The electrostatic potential is seen to decay exponentially, as would be expected for the form of Equation 3.1. The potential decays from the imposed boundary condition of 25 mV at the pore surface to the center-line value just under 8 mV that was also evident in Figure 3.9.

For each of the 236 different pore geometries described in Section 3.3, the LPB and Smoluchowski simulations were completed for three different charges assigned to the diffusing species. Specifically, one set of simulations used a charge resulting in electrostatic attraction between the solute and the membrane ($q = -1$), one set of simulations used a neutral solute ($q = 0$), and one set of simulations used a charge resulting in electrostatic repulsion between the solute and the membrane ($q = +1$). This resulted in a total of 708 simulations.

The center-line concentration profiles for 6 of the 708 simulations are shown in Figure 3.11, illustrating the effect of porosity and solute charge on the spatial distribution of the solute under steady-state conditions. The effect of the electrostatic interaction is seen most strongly in membranes with low porosity, as most of the pore volume is close to the charged surface. In contrast, large values of porosity tend to suppress the effect of the electrostatic interactions on the concentration profile. Note, however, that the concentration gradients are still affected by the electrostatic inter-

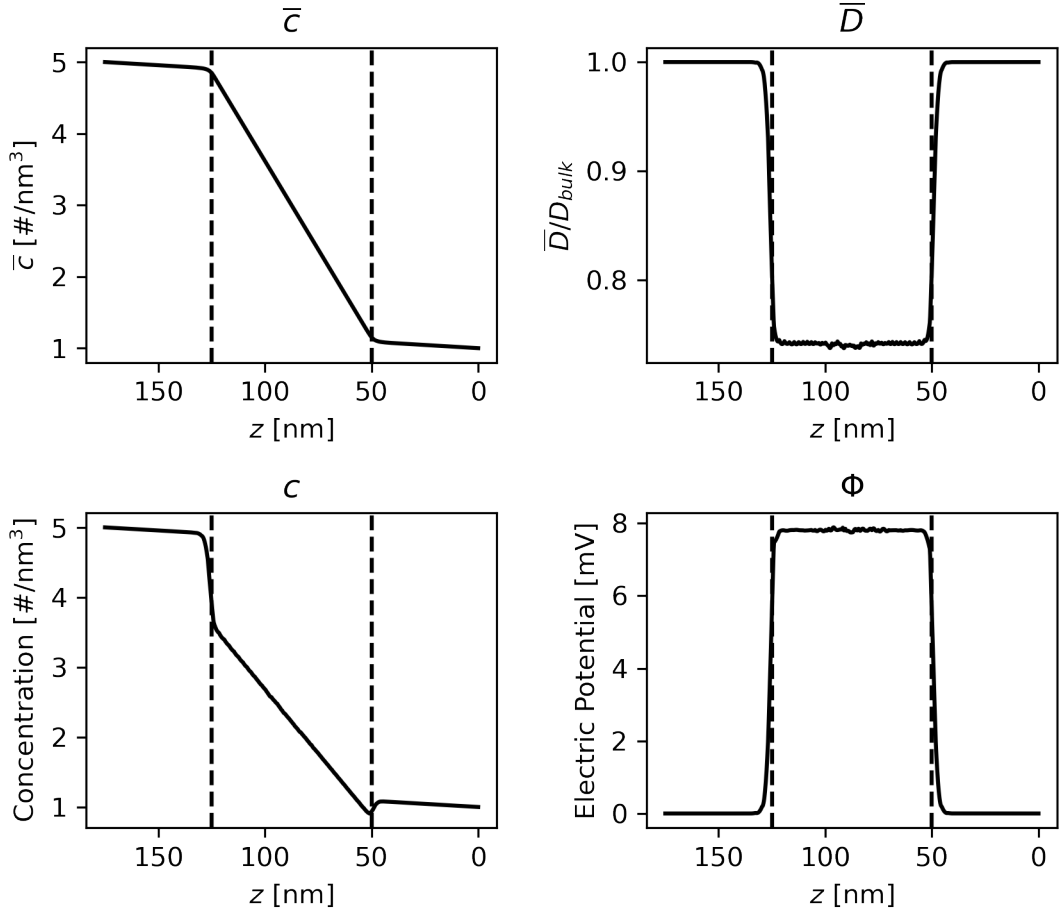


Figure 3.9: Solution variables for Smoluchowski diffusion, taken along the model centerline.

action at large porosity values, which in turn will result in changes to the effective diffusion coefficient. Furthermore, the profiles along the pore centerline show the concentration at the farthest point in the pore from the pore surface. The concentration at radial locations closer to the pore surface would still be affected more strongly by the electrostatic interactions.

The results of the 708 simulations are plotted as effective diffusion coefficient (normalized to the bulk value) versus porosity in Figure 3.12. The $q = 0$ case is identical to the results of Figure 3.6. The $q = +1$ case, where the electrostatic interaction is repulsive, shows suppression of the effective diffusion coefficient. This can be thought of as the consequence of a restriction of the accessible fraction of the pore volume, as the solute is forced away from the pore surface. However, in contrast to the results of Figure 3.11, the effect seems to be more pronounced at larger porosity values than at smaller ones. In the $q = -1$ case, where the electrostatic interaction is attractive, the diffusion appears to be accelerated relative to the neutral case.

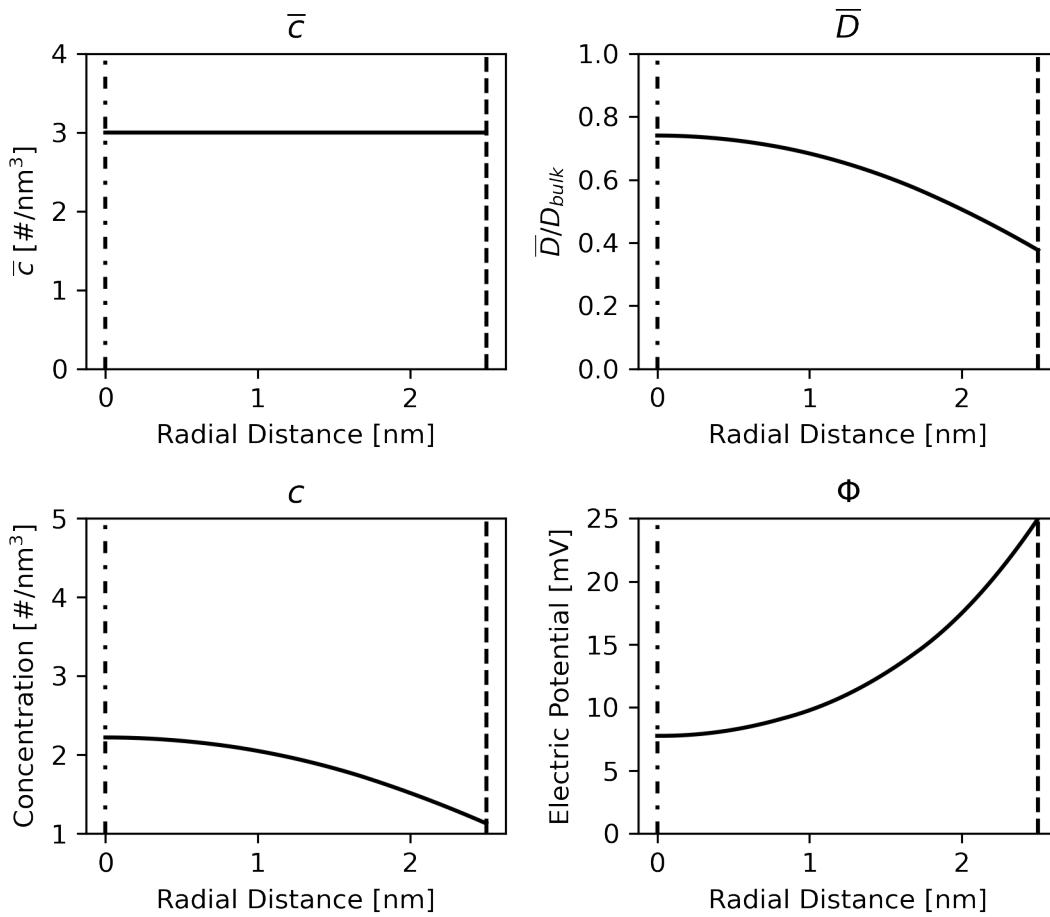


Figure 3.10: Solution variables along radial lines. The dashed line shows the radius of the pore boundary, and the dot-dashed line shows the position of the pore center, at zero radius. The solutions are radially symmetric about the pore center.

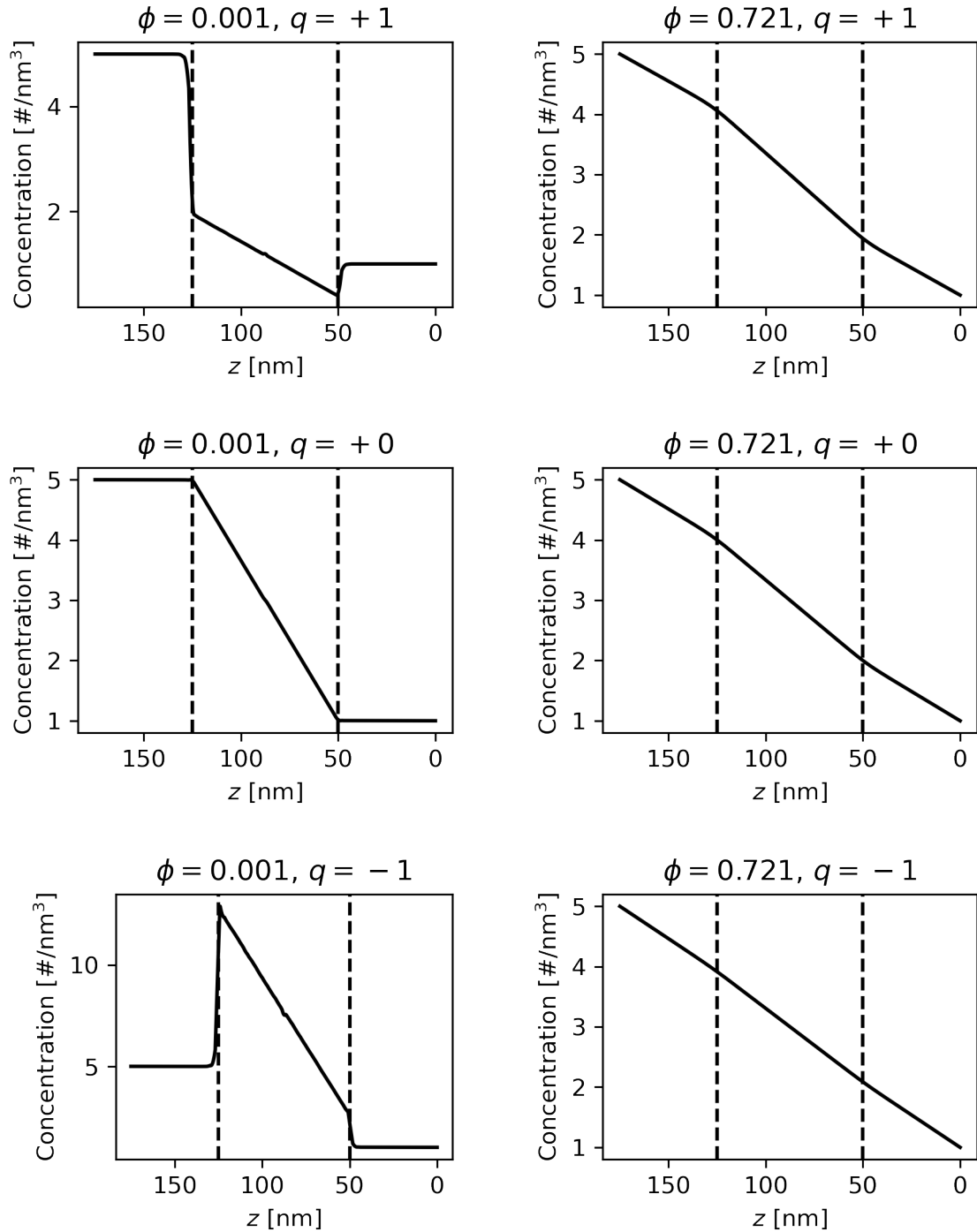


Figure 3.11: Concentration profiles along pore centerline. Solid lines show the concentration as a function of z , and the dashed lines show the limits of the pore. In all cases, the concentration boundary conditions are 5 particles/ nm^3 at $z = 175$ nm and 1 particle/ nm^3 at $z = 0$ nm. The electric potential is set to 25 mV at the membrane and pore surfaces, and zero at the reservoir ends.

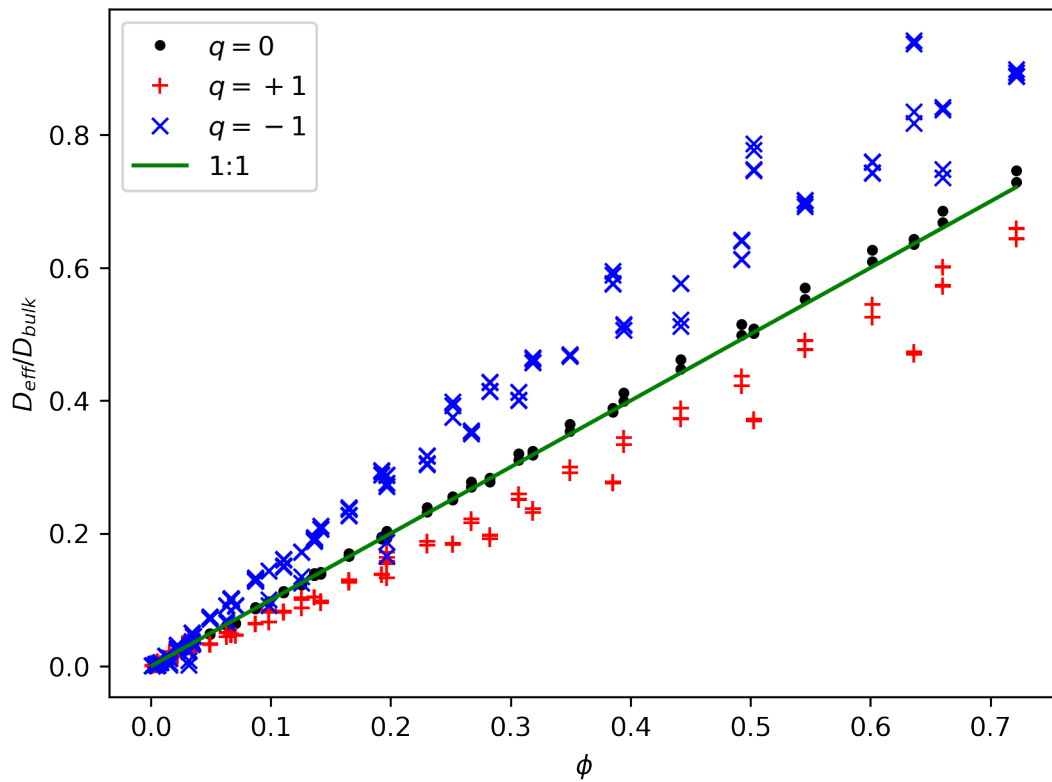


Figure 3.12: Influence of electrostatic interaction on relationship between effective diffusion ratio and porosity. Compared to the case of no electrostatic interaction ($q = 0$), repulsive interactions ($q = +1$) suppress diffusion, while attractive interactions ($q = -1$) accelerate it.

3.5 Diffusion-Limited Reaction Kinetics of a Single Enzyme

Consider an enzyme-catalyzed reaction, where enzyme E accelerates the conversion of chemical species A into species B: $A \xrightarrow{E} B$. If this reaction is sufficiently diffusion-limited, then the time required for the reaction to take place at the enzyme may be assumed to be negligible relative to the time required for the substrate A to reach the enzyme. That is, any amount of A in contact with E may be assumed to be instantly converted to B.

To add this kind of reaction into the model developed in Section 3.4, the enzyme is represented as a spherical inclusion within the pore. The reaction is implemented in the form of boundary conditions applied to this inclusion. A similar approach is used in Song et al. [123]. First, a Dirichlet concentration boundary condition of zero for species A is applied to the entire surface of the sphere. Additionally, the flux of species A and B through the surface are required to be equal and opposite, such that the total number of particles is conserved and only the type is altered, matching the stoichiometric coefficients of the reaction. Combined, these conditions result in the situation where the spherical inclusion consumes species A, and produces species B at the same rate. Mathematical details for this reactive boundary condition are presented in Appendix D, Section D.9.

The spherical inclusion representing the enzyme is not required to be centered on the centerline of the pore. This potentially breaks one axis of symmetry in the model. For maximum flexibility in the placement of the sphere within the pore, no planes of symmetry were used in these simulations; the entire unit cell was included in the finite element model.

The behavioral property of interest in this system is not the effective diffusion coefficient, but rather the rate at which the reaction takes place. This is quantified by the integrated flux for either species at the surface of the enzyme, $J_{EA} = -J_{EB}$, where J_{EA} is the rate at which species A is consumed, and $-J_{EB}$ is the rate at which species B is produced. The sign convention is such that a positive flux indicates a flux that is outward from the model, while a negative flux is inward to the model. This is related to the sign convention for the boundary surface normal vectors in FEniCS, which are positive in the outward direction.

An analytical solution to the Fickian diffusion problem is possible when the reactive sphere is placed in bulk fluid rather than confined to a nanopore. The problem is spherically symmetrical, and so it can readily be solved in spherical coordinates. The steady-state Fickian diffusion equation for this situation is shown in Equation 3.3. The solution $c_A(r)$ for species A in the domain outside the sphere, with constants K_1 and K_2 determined by the boundary conditions, is given by Equation 3.4.

$$\frac{d}{dr} \left(r^2 \frac{dc_A}{dr} \right) = 0 \tag{3.3}$$

$$c_A(r) = K_2 - \frac{K_1}{r} \tag{3.4}$$

For a sphere of radius a , the boundary condition at the surface of the sphere is that $c_A(r = a) = 0$. The other boundary condition needed for a unique solution to the problem is the concentration at a large distance from the sphere. This is simply that the concentration must return to the value it has in the bulk fluid in the absence of the sphere, $c_{A,\text{bulk}}$. This boundary condition is thus that $c_A(r \rightarrow \infty) \rightarrow c_{A,\text{bulk}}$. Under these boundary conditions, the constants of Equation 3.4 are given by Equation 3.5. The integrated flux over the surface of the sphere for these conditions, $J_{EA,\text{bulk}}$, is given by Equation 3.6.

$$\begin{aligned} K_1 &= c_{A,\text{bulk}}a \\ K_2 &= c_{A,\text{bulk}} \end{aligned} \quad (3.5)$$

$$J_{EA,\text{bulk}} = 4\pi Da c_{A,\text{bulk}} \quad (3.6)$$

If a linear reaction rate law is assumed for this system, the reaction rate coefficient k_E , would be defined by Equation 3.7. Thus, the result for the integrated flux can be used to obtain a reaction rate coefficient, for which the analytical result for bulk conditions is provided in Equation 3.8.

$$J_{EA,\text{bulk}} = k_{E,\text{bulk}} c_{A,\text{bulk}} \quad (3.7)$$

$$k_{E,\text{bulk}} = 4\pi Da \quad (3.8)$$

For a reactive sphere inside the nanopore rather than bulk fluid, the reaction rate should approach the bulk result as the pore radius grows larger. Accordingly, a set of simulations with increasing pore radius was conducted to validate the model of the nanopore including a reactive sphere. The boundary conditions for the reservoirs were that both reservoirs were set to a concentration of $c_{A,\text{bulk}}$. Thus, there was no concentration gradient applied to the membrane. Two different boundary conditions were applied to the pore surface. In the “reflecting” boundary condition, no flux of species A is allowed through the pore surface; this is a Neumann boundary condition of zero flux. In the “concentration” boundary condition, the concentration of species A along the pore surface is held constant; this is a Dirichlet boundary condition with a concentration of $c_{A,\text{bulk}}$. The results of this set of simulations are plotted and compared to the result for the bulk condition in Figure 3.13. The reaction rate coefficient for the pore condition is normalized to the analytical result for the bulk condition. As expected, the results for both boundary conditions approach the analytically derived result for bulk conditions as the pore radius increases. The rate coefficient for the concentration boundary condition is larger than the bulk condition result, because it brings a source of substrate closer to the enzyme. In contrast, the rate coefficient for the reflecting boundary condition is smaller than the bulk condition result, as the amount of substrate accessible to the enzyme is reduced. In addition to serving as a validation of the model, these results also illustrate that reaction kinetics of diffusion-limited reactions can be significantly affected by the geometry of their environment, and by the extent to which adjacent structures compete for substrate.

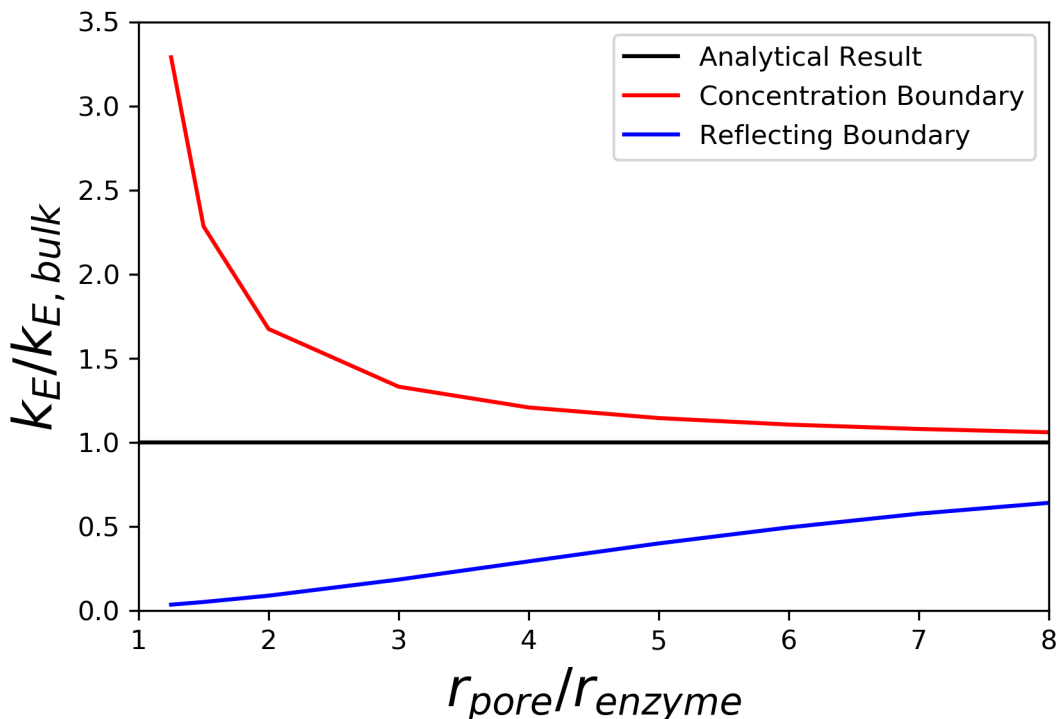


Figure 3.13: Reaction rate coefficient within the nanopore. The rate coefficient is normalized by the analytical result for the bulk condition. For both of the boundary conditions used for the pore surface, the results approach the bulk condition at the pore radius increases. The results show how the geometry of the surroundings can influence the reaction kinetics of diffusion-limited enzyme-catalyzed reactions.

3.6 Diffusion-Limited Kinetics of Sequential Enzyme-Catalyzed Reactions

Adenosine Triphosphate (ATP) is highly notable in its role as “the universal currency of free energy in biological systems” [13]. Living cells use the hydrolysis of ATP into Adenosine Diphosphate (ADP) and Adenosine Monophosphate (AMP) to drive chemical reactions that would otherwise be thermodynamically unfavorable. However, these nucleotides are used in biological systems as extracellular signaling molecules as well. This hypothesis faced great skepticism (and even derision) before finally gaining acceptance in the 1990s [23]. Signaling pathways using these nucleotides are now known to be involved in a variety of settings including the central nervous system, blood vessel linings, immune and inflammation responses, and many others [19, 23, 39].

In this section, two sequential reactions are considered, where the product of the first reaction is the reactant in the second. These two reactions are catalyzed by the CD39 and CD73 enzymes, respectively. CD39 (also known as NTPDase1) hydrolyzes ATP and ADP into AMP, while CD73 (also known as ecto-5'-nucleotidase) dephosphorylates AMP into adenosine [39, 78]. The CD39 and CD73 enzymes are

expressed by immune cells and the endothelial cells lining blood vessels, and their reaction sequence plays an important role in modulating inflammation [5, 39].

To investigate this system, the reactive enzyme model described in Section 3.5 was combined with the electrostatic interaction model of Section 3.4, within the pore geometry described in Section 3.2. Two sequential enzyme-catalyzed reactions were included: $\text{ATP} \xrightarrow{\text{CD}39} \text{AMP}$ and $\text{AMP} \xrightarrow{\text{CD}73} \text{Adenosine}$. Two spherical inclusions were therefore present within the pore, as shown in Figure 3.14. In this case, the cylindrical pore represented an extracellular junction where the enzymes were present. The overall system size was selected to match extracellular junctions such as synapses, which are often less than $1 \mu\text{m}^3$ in volume [17].

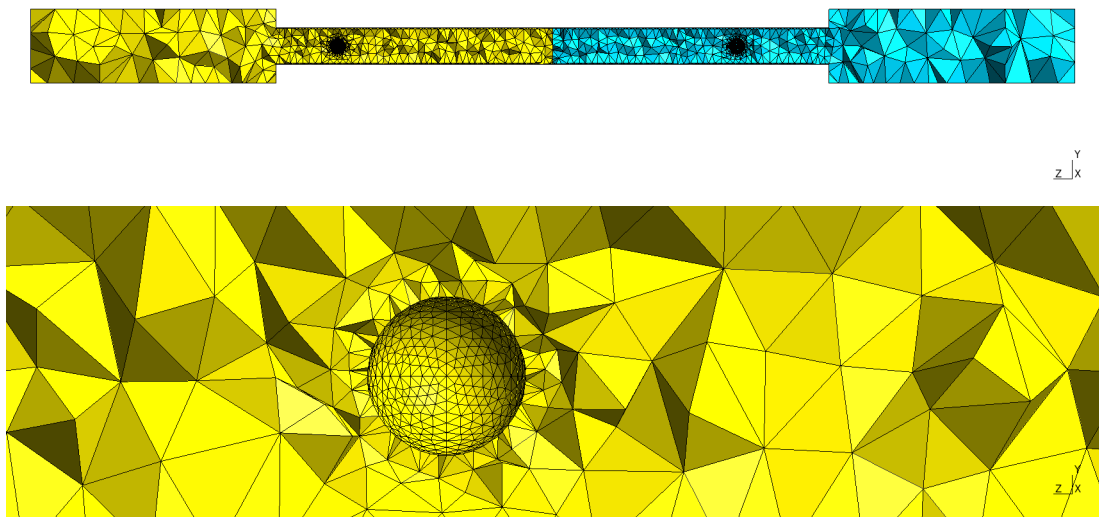


Figure 3.14: Cut through finite element mesh with reactive inclusions. Upper image: entire model, including reservoirs. Lower image: view showing left inclusion.

Parametric variations of the model parameters were used to study the effects of the junction radius, proximity of the two enzymes to each other and to the junction surface, electrostatic interactions between the nucleotides and the enzymes and junction surface, and interactions between the junction surface and the nucleotides. The results of the study are fully reported in Rahmaninejad et al. [104]. The main findings are briefly summarized here. First, in the absence of electrostatic interactions, the confined volume of the junction reduces the amount of substrate accessible to the first enzyme compared to a reaction in bulk conditions. However, the intermediate molecules are also confined, increasing the rate of the second reaction and thereby improving the efficiency of the sequence. Finally, within the volume of the junction, attractive electrostatic interactions between the junction surface and the substrate can increase the local concentration of substrate, potentially compensating for the lack of accessible volume.

The space inside living cells is frequently crowded with macromolecules, which can have significant impacts on the diffusion and interaction of biochemicals within their environment [42, 71, 110]. Extracellular spaces such as the junction considered here may be similarly crowded environments. An extension of this study is currently in progress, to investigate the effects of such crowding on the CD39/CD73 system. To this end, the finite element mesh is modified to include additional spherical inclusions representing the macromolecular crowders, as shown in Figure 3.15. The number of crowders and their electrostatic potential will be varied, to determine the consequences of such variations on the efficiency of the sequential reaction.

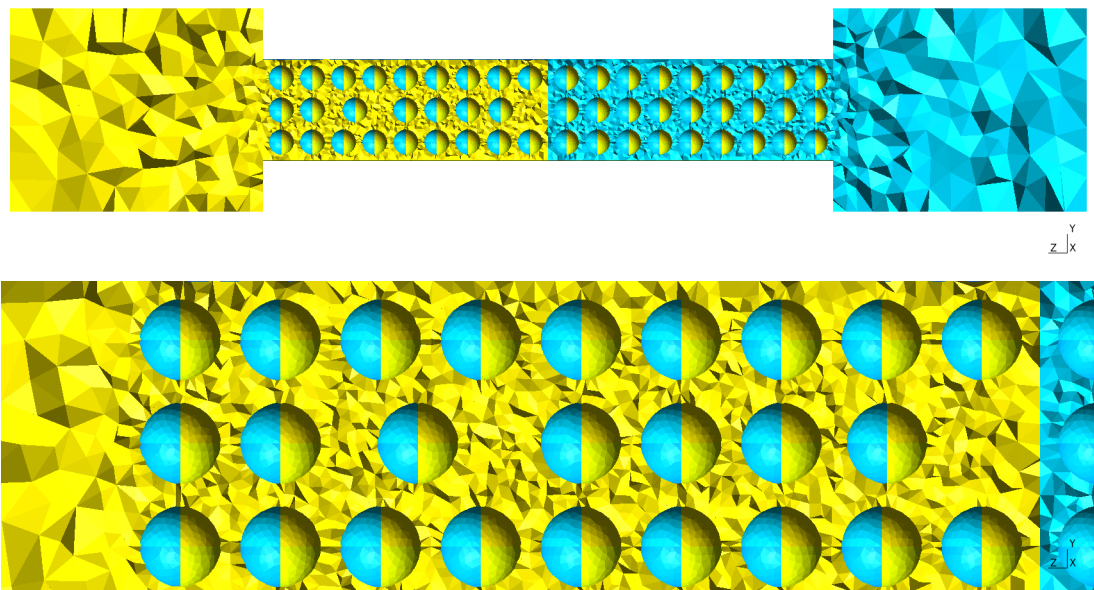


Figure 3.15: Cut through finite element mesh with non-diffusive inclusions. Upper image: entire model, including reservoirs. Lower image: view showing crowders in half of pore. Element surfaces are shown, with coloring by model region. Each spherical inclusion is made of eight curved surfaces.

3.7 Discussion and Conclusion

This chapter has illustrated the construction of a multiphysics model by starting with a simple model and adding additional complexity in stages, validating the additions at each step. Ultimately, the model was applied to a biochemical system to investigate the kinetics of sequential enzyme-catalyzed diffusion-limited reactions. Other applications of this model may be found in the future. Indeed, the model is a basis for the multi-scale multiphysics model described in Chapter 4. Another possible avenue for further development of the model would be searching for approaches that can relax the requirement of considering only diffusion-limited reactions. This would allow the model to be used for systems where the reaction and diffusion time scales are more nearly comparable. Such a change might require a time-dependent model

rather than a steady-state model. Time-dependence would complicate the interpretation of the simulation results, as the reaction kinetics parameters used in Sections 3.5 and 3.6 were defined in terms of steady-state variables. Incorporation of atomistic information into the continuum approximation, using MD approaches similar to those discussed in Chapter 4 might be beneficial as well.

Other work to be done in the future with this model, and similar models, concerns finding the limitations of the continuum approximation. To illustrate this issue, consider the relative sizes of the nanoscale pore, which was on the order of 10 nm in radius, and a single ATP molecule, which is almost 2 nm in its largest dimension. This means the size of the diffusing particle is a significant fraction of the size of the junction itself. Only a small fraction of an ATP molecule can be present in any cubic nanometer the junction volume. In such a case, the continuum approximation is not justified on the basis of scale separation or the number of ATP molecules present alone. Instead, the continuum model must be considered to represent an ensemble average over a large number of similarly prepared systems. While the principle of an ensemble average justifies the continuum simulations, there may be unexpected implications to this interpretation that have not yet been recognized. There may be benefits to formalizing this interpretation of the model.

Chapter 4 Transport Properties of Zeolites and Other Porous Silicates

4.1 Background

Methane is the primary component of natural gas and a byproduct of many industrial chemical processes, including anaerobic digestion and shale oil extraction. Methane is also a greenhouse gas more potent than carbon dioxide. For both economic and environmental reasons, there is much interest in using waste methane as an energy source, rather than merely venting or burning it where it is produced. Because of the difficulties in transporting methane gas, conversion of methane to a liquid hydrocarbon is desirable. Such conversion can be achieved using common catalyst materials, but high temperature and/or pressure is required, which in turn increases the energy demand of the process. A more efficient approach is desired.

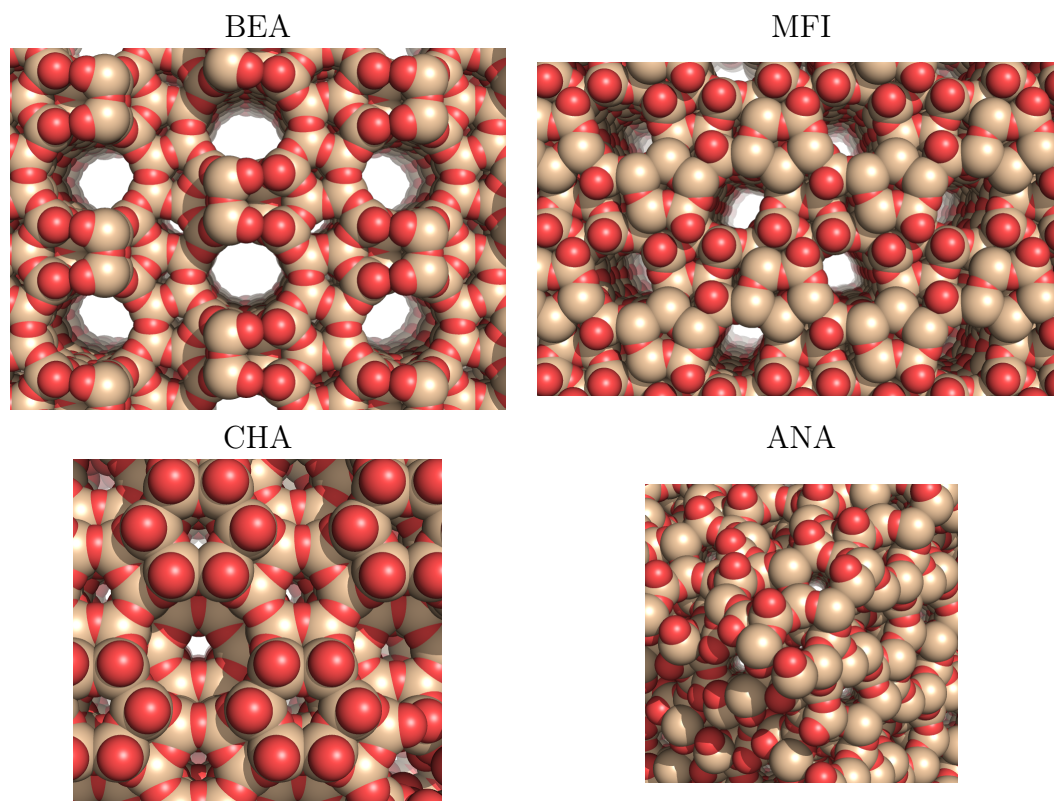


Figure 4.1: Renderings of four different zeolite frameworks. Oxygen atoms are red, and Silicon atoms are brown. The view direction of each crystal structure is selected to show the full size of the largest straight pores. The three-letter identifier is shown for each framework. Framework structures were collected from iza-structure.org, and rendered in PyMOL.

One candidate for a more efficient conversion process is an aqueous approach using hydrogen peroxide as the oxidant. This approach is described, for example, in

Hammond et al. [53]. The catalyst in this approach is a zeolite material.

Zeolites are aluminosilicate materials commonly used as a catalyst medium in the chemical processing industry. Zeolite catalysts are common because they are inexpensive, porous, and highly adsorbent. There are many different zeolite materials; over 240 different crystal frameworks are presently known, and each of these frameworks can have varying ratios of aluminum, silicon, and other elements, so that many different materials can be composed from a single framework. The crystal frameworks are given three-letter identifiers. Some representative renderings to illustrate the variety of frameworks are shown in Figure 4.1.

Rational design of an aqueous methane conversion process would require an understanding of the transport properties of the methane reactant through the aqueous environment in the zeolite material. The ultimate objective of this chapter is to develop a multi-scale multiphysics model that will allow the effective diffusion coefficient to be obtained from knowledge of the zeolite structure and other relevant process variables.

4.2 Theoretical Model

The theoretical model presented herein uses periodic homogenization to obtain an effective diffusion coefficient for the unit cell. While some homogenization calculations are performed here for validation or comparison purposes without information from a smaller scale, one key objective is to incorporate information from atom-scale analyses into the homogenization approach. Toward this end, MD simulations are performed to obtain local values of the diffusion coefficient and potential at many points within the unit cell. Spatial variation in the local diffusion coefficient can be included in the homogenized Fickian diffusion equation or homogenized Smoluchowski equation, but the homogenized Smoluchowski equation is required for calculations that incorporate a potential.

The potential that is relevant in the continuum-scale simulation is not solely an electrostatic potential, as the methane molecule has no net electric charge and negligible electric dipole moment [95]. Rather, the potential of interest is the net result of all inter-molecular interactions between methane and the surrounding water (or even the silicate surface if close enough). In MD simulations, such potentials are often considered for the purpose of estimating energy barriers to chemical reactions or other transitions. For this reason, the potential energy surface is often measured along a given reaction coordinate, which is not necessarily an atomic coordinate or even a geometric parameter. In some cases, reaction coordinates can have more than one dimension. For the transport problem considered here, the spatial location of the methane molecule is the reaction coordinate of interest. The free energy of the system (the Helmholtz or Gibbs free energy, depending on the thermodynamic ensemble) as a function of the reaction coordinate is called the potential energy surface, or the Potential of Mean Force (PMF) [67, 97]. In MD simulations, the short-range inter-molecular interactions are approximated by the force field. This means that changes in the force field can result in changes to the PMF.

The local diffusion coefficient is obtained from MD simulations using an approach described in Daldrop et al. [37], based on earlier work in Hummer [61] and Woolf and Roux [133]. This approach was also previously used by Setny et al. [118]. The theory behind this approach is described briefly here.

First, consider Brownian motion in a harmonic potential. The Langevin equation for this condition is shown in Equation 4.1. Furthermore, consider the limit of strong friction, where the oscillation of the particle in the harmonic potential is overdamped. In the field of stochastic differential equations, this is known as an Ornstein-Uhlenbeck process.

$$M\partial_t\partial_t x_i = -\xi\partial_t x_i - \partial_i U(x_i) + F_i \quad (4.1)$$

where

$$\begin{aligned} M &= \text{particle mass } \llbracket \text{M} \rrbracket \\ x_i &= \text{time-dependent particle position vector } \llbracket \text{L} \rrbracket \\ M\partial_t\partial_t x_i &\rightarrow 0 \text{ in the limit of strong friction (overdamped oscillator)} \\ \xi &= \text{coefficient of friction } \llbracket \frac{\text{M}}{\text{T}} \rrbracket \\ F_i &= \text{force varying randomly in time } \llbracket \text{F} \rrbracket \\ U &= \text{harmonic restraining potential } \llbracket \text{E} \rrbracket \\ &= \frac{1}{2}K(x_i - a_i)^2 \\ K &= \text{spring constant defining harmonic potential strength } \llbracket \frac{\text{F}}{\text{L}} \rrbracket \\ a_i &= \text{position vector for center of harmonic potential } \llbracket \text{L} \rrbracket \\ \partial_i U(x_i) &= K(x_i - a_i) \llbracket \text{F} \rrbracket \end{aligned}$$

Because of the harmonic potential, the MSD will not be proportional time as it is in the unrestrained case (see Section 1.7). Instead, it can be shown that for Brownian motion in a harmonic potential, the coordinate MSD and position ACF are as shown in Equations 4.2 and 4.3, respectively. A more detailed explanation of the source of these equations is provided in Appendix D, Section D.10.

$$\langle q^2 \rangle = \frac{1}{\beta K} \quad (4.2)$$

$$\begin{aligned} \langle q(0)q(t) \rangle &= \langle q^2 \rangle e^{-\frac{t}{\tau}} \\ \tau &= \frac{\xi}{K} \end{aligned} \quad (4.3)$$

Integrating the coordinate ACF with respect to time provides an estimate of τ , which can be used to obtain the local diffusion coefficient, D , through the Einstein relation ($D = 1/\beta\xi$), as shown in Equation 4.4. Relationships like this between a transport coefficient and the integral with respect to time of a time-correlation function are known as Green-Kubo relations [47].

$$\int_0^\infty dt \langle q(0)q(t) \rangle = \langle q^2 \rangle \int_0^\infty dt e^{-\frac{t}{\tau}} = \langle q^2 \rangle \tau = \langle q^2 \rangle \frac{\xi}{K} = \frac{\langle q^2 \rangle}{D\beta K} = \frac{\langle q^2 \rangle^2}{D} \quad (4.4)$$

This approach is used in the simulations of methane diffusing through water by applying a harmonic restraining potential to the methane molecule. In this case, the PMF acts as an additional potential not included in Equation 4.1. Assuming that the gradient of the PMF is small in comparison to the value of K for the restraining potential, the procedure should remain valid. Furthermore, large values of K will confine the methane to a smaller region around the center of the harmonic potential, allowing variations in D to be defined with greater spatial precision. However, large values of K can also invalidate the assumption of overdamping. This can result in oscillatory behavior in the position ACF, making integration more difficult [37]. Here, the value of K for the harmonic potential was selected to be small enough to maintain overdamped behavior, while remaining larger than reasonable magnitudes for the PMF gradient. In the calculations, the actual MSD value is used rather than the theoretical value for a harmonic potential, because the actual potential is the superposition of the harmonic biasing potential and the PMF.

This work differs from previous research in some key ways. Hansen et al. [54] considered the alkylation of benzene within a zeolite catalyst. The reaction and diffusion were considered in the gas phase. Consequently, the Maxwell-Stefan diffusion equations were used rather than Fickian or Smoluchowski diffusion. Information from MD and kinetic Monte Carlo simulations was used to provide inputs to the continuum diffusion model. No PMF was considered. The continuum diffusion model was evaluated analytically rather than numerically. One key focus of the study was to predict reaction rates agreeing with experiment, which is not attempted herein.

Another similar analysis was conducted by Bui et al. [22], where a channel of one nanometer in width was studied in various materials, including silica. The study computed the diffusion coefficient within the channel using the MSD of unrestrained methane. This results in a coefficient value that does not distinguish spatial variations within the channel. No multi-scaling method was applied to the result. In addition to using a metadynamics approach to evaluate the free energy variations within the channel, umbrella sampling was also applied. Finally, the silica structure of the Bui et al. [22] study does not appear to include silanol terminations at the surface. The silanol groups present on the silicate surfaces studied herein would be expected to increase the affinity for water molecules, leading to different results for the water density within the channel, and consequently affecting the PMF and diffusion coefficients. Similar to the results presented below, the study found anisotropy in the diffusion coefficient, with differing coefficients for directions perpendicular to the silica face than parallel to it.

4.3 Silicate Channel System

In addition to the zeolite framework geometries, a simpler system geometry was developed to investigate the proposed theoretical model. The simpler system consists of a silicate solid with parallel nanoscale channels, as shown in Figure 4.2. The silicate structures provided in Emami et al. [43, 44] were used to construct this geometry in the MD simulations.

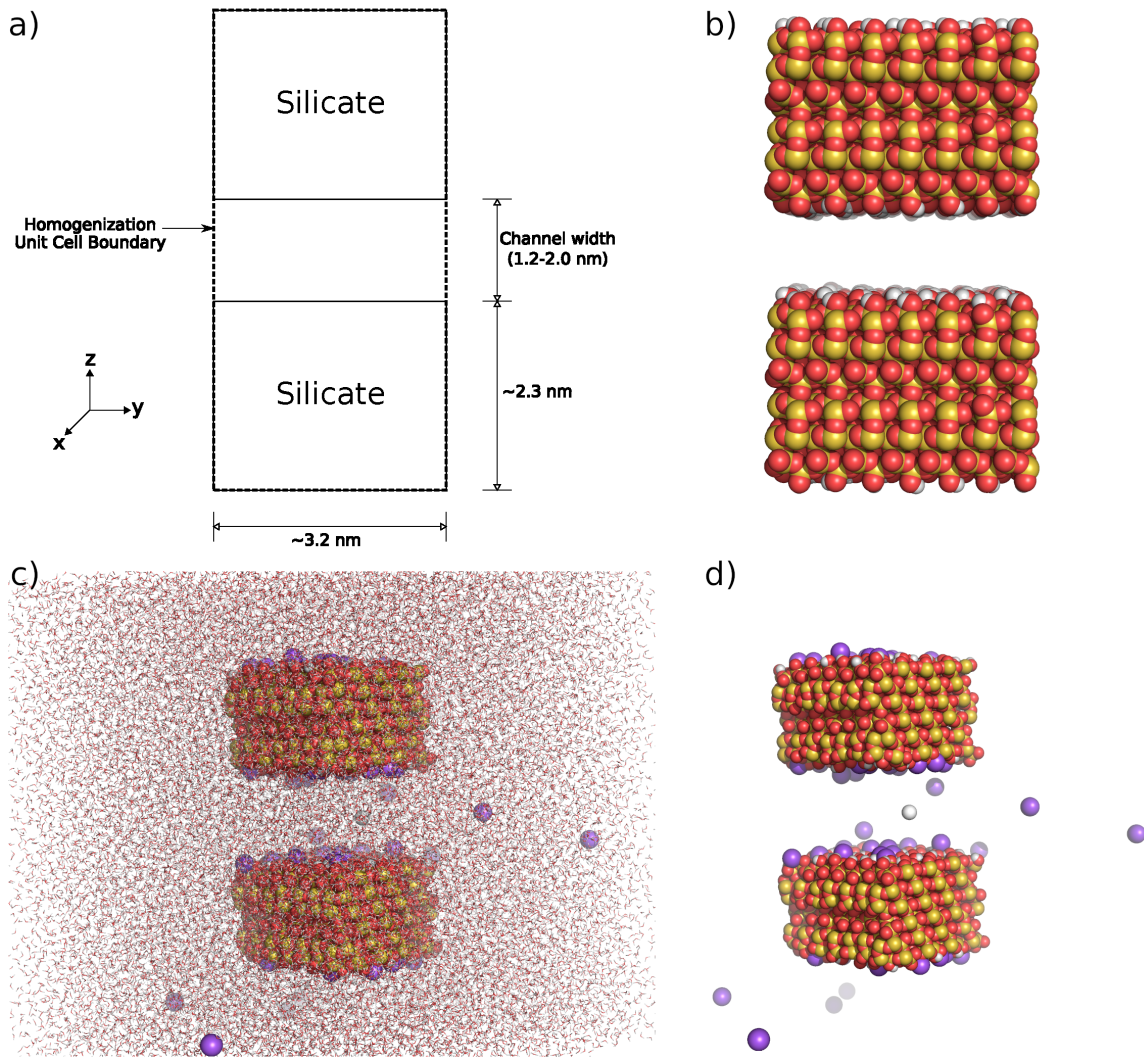


Figure 4.2: Geometry of the silicate channel model. a) Sketch showing key dimensions and coordinate axes. b) Rendering of the 1.2 nm channel along the X-axis in the fully protonated condition. c) Oblique rendering of the 2.0 nm channel with 27% de-protonation after solvation and equilibration. d) Same view as (c) without water molecules. The methane molecule is visible in white, near mid-channel.

The surface of the silicate structures differs chemically from the bulk silicate structure by the presence of hydrogen atoms bonded to the surficial oxygen atoms. These silanol terminations on the surface would be expected to more favorably attract polar solvents such as water, causing spatial variations in the water density near the silicate surface. These silanol groups can also be chemically modified, by replacing them with a different functional group. De-protonation is studied herein by replacing the hydrogen atoms with sodium ions, which are allowed to migrate away from the silicate face, leaving a negatively charged oxygen atom behind. Three different levels of de-protonation are provided in the structures from Emami et al. [43]: 0%, 27%, and 50%. Simulations were conducted for each of these de-protonation levels. By

influencing the water density near the channel surface, such chemical modifications are expected to alter the transport properties within the channel.

4.4 Methods

Molecular dynamics simulations were conducted in `gromacs`. The OPLS-AA SPC water model was used for the explicit solvent. The united atom approximation was selected for the methane molecule, on the basis of the results presented in Bhatia and Nicholson [14]. The non-bonded force field parameters for methane were taken from Jorgensen et al. [66], which used the same functional form for the 12-6 Lennard-Jones potential as `gromacs`, so that only unit conversions of the parameters were required. While the combining rule noted in Jorgensen et al. [66] is the geometric average, the arithmetic average is used herein. The force field parameters for silica were taken from Emami et al. [43, 44], and converted to the units and functional form used in `gromacs`. Specifically, the functional form of the 12-6 Lennard-Jones potential for non-bonded interactions in Emami et al. [43] is given by Equation 4.5, while the functional form used by `gromacs` is shown in Equation 4.6. In both equations, E is the interaction energy, and r is the separation distance between the two atoms. The two functional forms can be used to represent the same interaction potential by computing the `gromacs` parameters from the parameters provided by Emami et al. [43] using the relationships of Equation 4.7.

$$E = \epsilon_{\text{amber}} \left(\left(\frac{\sigma_{\text{amber}}}{r} \right)^{12} - 2 \left(\frac{\sigma_{\text{amber}}}{r} \right)^6 \right) \quad (4.5)$$

$$E = 4\epsilon_{\text{gromacs}} \left(\left(\frac{\sigma_{\text{gromacs}}}{r} \right)^{12} - \left(\frac{\sigma_{\text{gromacs}}}{r} \right)^6 \right) \quad (4.6)$$

$$\begin{aligned} \epsilon_{\text{gromacs}} &= \epsilon_{\text{amber}} \\ \sigma_{\text{gromacs}} &= 2^{-1/6} \sigma_{\text{amber}} \end{aligned} \quad (4.7)$$

To confirm the proper conversion of the non-bonded force field parameters, the same method was used to convert the parameters from an AMBER input file to the corresponding `gromacs` input file parameters for an AMBER force field. This comparison involves an additional step, because the AMBER force field parameters specify the van der Waals radius of each atom, and the depth of the potential well, rather than specifying σ_{amber} and ϵ_{amber} directly. The additional calculation is relatively simple, because the functional form of Equation 4.5 used by AMBER has a well depth that is equal to ϵ_{amber} , with the point of minimum potential energy located at $r = \sigma_{\text{amber}}$. At this minimum, the separation distance r between two identical atoms would be twice the van der Waals radius. Thus, σ_{amber} is simply twice the specified van der Waals radius, and ϵ_{amber} is equal to the depth of the potential well. Using this information, the `gromacs` parameters for the AMBER96 and AMBER99 force fields were successfully reproduced.

Following solvation, energy minimization was performed for 50,000 steps, and then velocities were randomly assigned according to a Maxwell distribution. The

system was equilibrated in the NVT ensemble for 0.1 nanoseconds, using the Nosé-Hoover thermostat. This was followed by 0.1 nanoseconds of equilibration in the NPT ensemble, using the Berendsen barostat and modified Berendsen thermostat. Production runs followed, using the NVT ensemble with the Nosé-Hoover thermostat. The production runs had a duration of 2 nanoseconds, except where noted otherwise. In all analysis steps, electrostatic interactions were evaluated using the PME method. The dynamic runs used a time-step of 2 femtoseconds, with hydrogen bonds converted to constraints maintained by the LINCS algorithm.

The harmonic restraining potential applied to the methane molecule used a K of 300 kJ/(mol nm²), for each direction. To prevent global translations, rotations, or deformations of the silicate bodies within the simulation unit cell, each atom of the silicate material was placed in a harmonic restraining potential with K of 1000 kJ/(mol nm²), for each direction. This includes the hydrogen atoms on the surficial silanol groups, which may potentially have affected the solvent-surface interactions under study.

Simulations of the solvated silicate channel without methane were used to calculate the spatial variation of water density within the channel. Water density was calculated from the water molecule trajectories using the `MDAnalysis` package [49, 90] (which uses `NumPy` [128]). The production runs for the water density calculations were 128 nanoseconds in duration.

Based on the water density results, portions of the channel were selected for detailed measurement of the local diffusion coefficient and PMF for methane. An x -plane was chosen, with dimensions in the z -direction fully extending across the channel from one silicate face to the other. The selected area also extended 0.6 nanometers in the y -direction. A different region was selected for each channel geometry and de-protonation level. The regions were chosen so as to include areas of both high and low water density at the channel boundaries.

PMF values were computed using the two-dimensional version of `wham` [52] (Version 2.0.10.1), which implements the Weighted Histogram Analysis Method (WHAM) [79, 80, 112]. The y and z coordinates of the molecule were used as the reaction coordinates in this approach.

Local diffusion coefficients were calculated using the integral in Equation 4.4. Position ACFs were calculated by `gromacs`, which returns the ACF function normalized by the MSD as illustrated in Equation 4.8.

$$\text{normalized ACF}(t) = \frac{1}{\langle q^2 \rangle} \langle q(0)q(t) \rangle \quad (4.8)$$

Observations of typical normalized ACF results showed that, in addition to the exponential decay predicted by Equation 4.3, there was also an short-duration Gaussian superimposed on the ACF for small values of time. Accordingly, the functional form in Equation 4.9 was selected as being a generally representative form, with fitting constants A , α , and σ . The analytical integral of this form is shown in Equation 4.10.

$$\text{normalized ACF}_{\text{fit}}(t) = Ae^{-t/\sigma} + (1 - A)e^{-\alpha t^2} \quad (4.9)$$

$$\tau = \int_0^{\infty} dt (\text{normalized ACF}_{\text{fit}}(t)) = A\sigma + \frac{1-A}{2} \sqrt{\frac{\pi}{\alpha}} \quad (4.10)$$

Following calculation of a normalized ACF from methane trajectory data, a `python` script using the `NumPy` package [128] fit the analytical function of Equation 4.9 to the normalized ACF data. The analytical integration of the normalized ACF was then calculated from Equation 4.10. To confirm a successful fit, the integral of the normalized ACF was also obtained numerically using the trapezoidal rule over the first 25 picoseconds. Cases where the numerical and analytical integrations differed by more than 25% were discarded from the data set.

As noted in Section 4.9, the diffusion coefficients computed from the methane ACFs were generally consistent for the x and y directions, but different in the z direction. Ultimately, the effective diffusion coefficient for only the x and y directions is desired, as the z direction would be impervious. Furthermore, the channel itself is identical in the x and y directions, so the expected results for these two directions would be identical. Accordingly, the homogenization process used an isotropic local diffusion coefficient, which was computed as the arithmetic average of the x and y results from the MD simulations.

As noted in Section 4.5, the local diffusion coefficient results from MD were normalized to the bulk value predicted by the same method. In any cases where the normalized result was greater than 2.0, the result was limited to this value.

The finite element meshes for homogenization were created in `gmsht` [48]. The FEM analysis was conducted with `python` code relying on version 2019.1.0 of the `FEniCS` package [2, 84]. Homogenization of the Smoluchowski equation was implemented with the assistance of the Slotboom transformation. Following this transformation, the governing PDE has the same form as the Fickian diffusion equation. This allows the same weak form presented for homogenized Fickian diffusion in Appendix D, Section D.3 to be used here as well, with \bar{D} used in place of D in both the corrector problem and REV integral. As noted in Appendix D, Section D.11, this results in an effective value of \bar{D} , which changes when the potential is shifted by a constant value. In contrast, a physically measurable diffusion coefficient would not be changed by this operation. Accordingly, the transformation described in Appendix D, Section D.12 to recover the gauge-independent effective diffusion coefficient was attempted. Calculation of the effective diffusion coefficient using the integrated flux from the solution of the Smoluchowski equation, as described in Appendix D, Section D.8, was also used for comparison purposes.

In homogenization, the boundary conditions for the unit cell are that the corrector function should be periodic, with period matching the unit cell [12]. The `python` scripts using `FEniCS` were able to implement periodic boundary conditions for two-dimensional problems. While `FEniCS` supports periodic boundary conditions in three-dimensions, the programming effort required is considerably greater. Consequently, periodic boundary conditions were implemented for two-dimensional unit cells only. For three-dimensional unit cells, Dirichlet boundary conditions were used instead, with the corrector set to zero at the boundaries. While this is technically a periodic condition, it may be too restrictive for the corrector functions in some

cases. Generally, this boundary condition is appropriate for situations where barriers to diffusion within the unit cell are located away from the cell boundaries.

4.5 Validation Analyses for Molecular Simulations

MD simulations were conducted to validate the approach presented in Section 4.2 for obtaining the local diffusion coefficient. These validation simulations include a single methane molecule in bulk water, to facilitate comparison with experimental results presented in Witherspoon and Saraf [132].

The validation simulation was conducted with two different force fields: the force field described in Section 4.4 derived from Emami et al. [43], and the GROMOS 53A6 force field [94] used by Daldrop et al. [37] in their validation. Each simulation was 16 ns in duration, and was conducted at a temperature of 298 K.

The coordinate MSD values from the two simulations are shown with the theoretical value in Table 4.1. Both force fields gave MSD results that approximated the theoretical result of $1/\beta K$ for a purely harmonic potential, and the two simulation values were in agreement with one another.

Table 4.1: MSD results from simulations of methane in bulk water.

Direction	Theoretical Result (nm ²)	Selected Force Field (nm ²)	GROMOS 53A6 Force Field (nm ²)
x	0.0083	0.0081	0.0081
y	0.0083	0.0079	0.0081
z	0.0083	0.0083	0.0079

An example positional ACF curve from each simulation is shown in Figure 4.3. The diffusion coefficient for methane in bulk water was then calculated in both simulations from the ACF and MSD for each direction. The results are shown in Table 4.2. The GROMOS 53A6 force field matches the experimental results quite well, as reported by Daldrop et al. [37]. The selected force field overestimates the diffusion coefficient by roughly 60%, because it gives a slightly lower curve for the ACF as shown in Figure 4.3. Accordingly, local diffusion coefficient values computed using the selected force field should be normalized by the bulk value presented here for correct interpretation. Specifically, the local diffusion coefficient values are divided by 3.0×10^{-5} cm²/sec (equivalent to 3.0 nm²/nsec) to report the ratio of local diffusion to bulk diffusion.

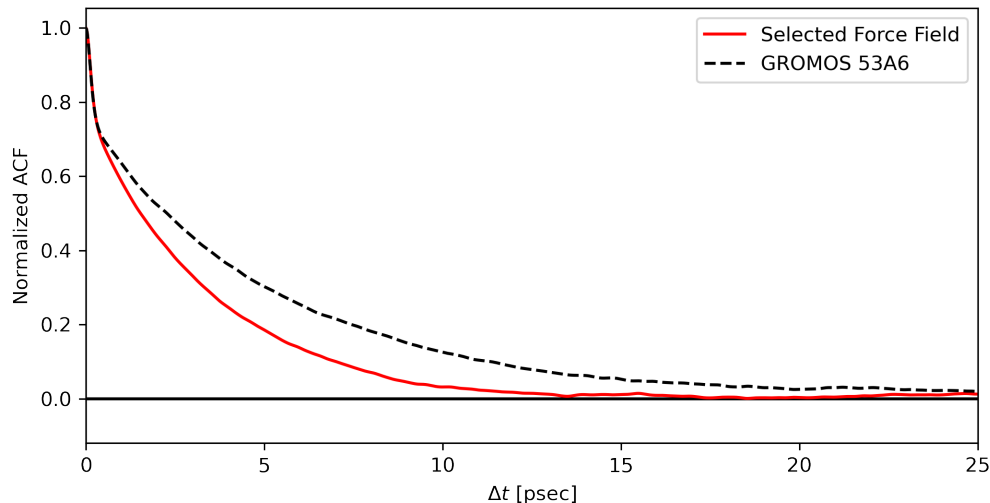


Figure 4.3: Comparison of position Autocorrelation Functions using two different force fields. The ACF values are normalized to their respective coordinate MSD values. Both curves are for the z-direction. The selected force field is described in Section 4.2. The results from the GROMOS 53A6 force field provide a diffusion coefficient that matches the result from physical measurement.

Table 4.2: Diffusion coefficient results from simulations of methane in bulk water.

Direction	Experimental Result [132] ($1 \times 10^{-5} \text{cm}^2/\text{sec}$)	Selected Force Field ($1 \times 10^{-5} \text{cm}^2/\text{sec}$)	GROMOS 53A6 Force Field ($1 \times 10^{-5} \text{cm}^2/\text{sec}$)
x	1.88	3.13	1.91
y	1.88	2.96	1.73
z	1.88	3.06	1.85
Mean Value	1.88	3.05	1.83
Sample Standard Deviation	n/a	0.09	0.09
Coefficient of Variation	n/a	3%	5%

As a further validation of the local diffusion coefficient, an alternative method was also used for the simulation of methane in bulk water. In these simulations, the methane was not restrained. As indicated in Frenkel and Smit [47], a diffusing particle without restraint is expected to have a MSD that increases linearly with time. The derivative of the MSD with respect to time is $2N_d D$. For the simulations of unrestrained methane in bulk water, the MSD was plotted against time and fit to a linear increase, with the diffusion coefficient calculated from this fit. Results from three trials (trial A, trial B, and trial C), are shown in Figure 4.4. The resulting diffusion coefficients are shown in Table 4.3. Notably, the MSD approach for unre-

strained methane exhibited greater variation in the diffusion coefficient than the ACF approach for restrained methane.

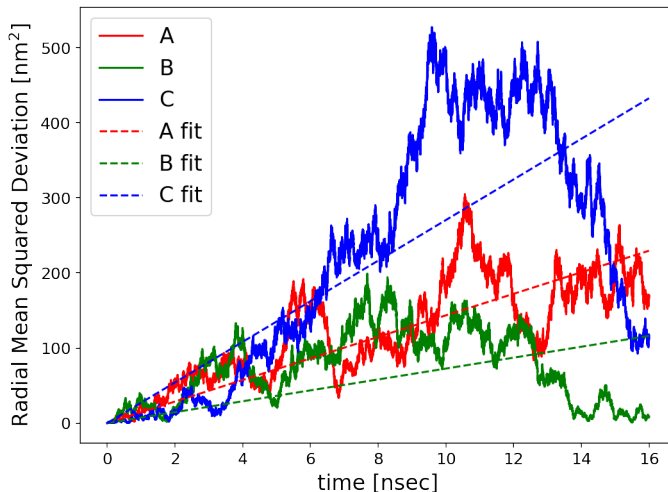


Figure 4.4: Calculation of diffusion coefficient from MSD, for three different trials. Each simulation had a duration of 16 ns.

Table 4.3: Diffusion coefficient results from unrestrained methane simulations in bulk water.

Trial	Result from MSD ($1 \times 10^{-5} \text{cm}^2/\text{sec}$)
Trial A	2.39
Trial B	1.21
Trial C	4.51
Mean of Trials	2.70
Sample Standard Deviation	1.67
Coefficient of Variation	62%

Figure 4.5 summarizes the validation results by averaging over the directional components. As noted above, the ACF calculation using the GROMOS 53A6 force field agreed with the experimental results of Witherspoon and Saraf [132]. The ACF and MSD approaches using the selected force field gave notably higher diffusion coefficient values, but were in general agreement with one another. Accordingly, the selected force field is assumed to give diffusion coefficients that are proportional, but not identical, to the expected results of experiment. This proportionality is applied to the results by normalizing to the bulk water diffusion result as described above.

An additional validation can be performed using the simulation of methane in bulk water. At sufficient distance from the restrained methane molecule, the number

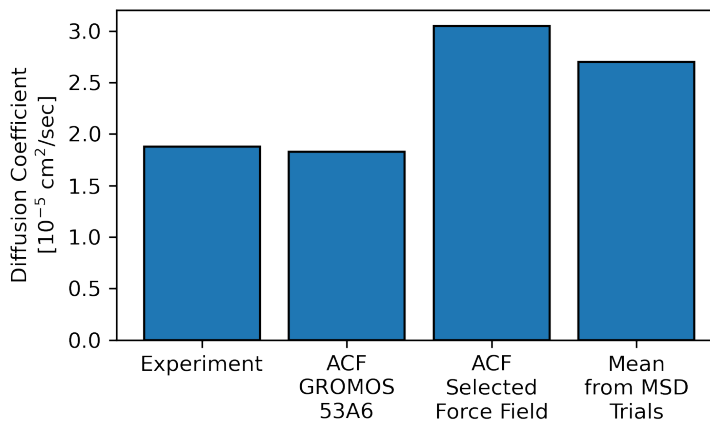


Figure 4.5: Comparison of diffusion coefficient for methane in bulk water from different methods.

density of the water molecules should approach the bulk value. The water density along a line passing through the center of the restraining potential for the methane molecule is shown in Figure 4.6. Two different simulation durations are shown: 16 nanoseconds and 64 nanoseconds. Both results show that the water density is depressed in the immediate vicinity of the methane molecule. But, as expected, the bulk density is recovered at sufficient distance. The oscillations about this value are slightly reduced in the longer simulation. Based on these results, a simulation duration of 128 nanoseconds was selected for the water density calculations within the methane channel.

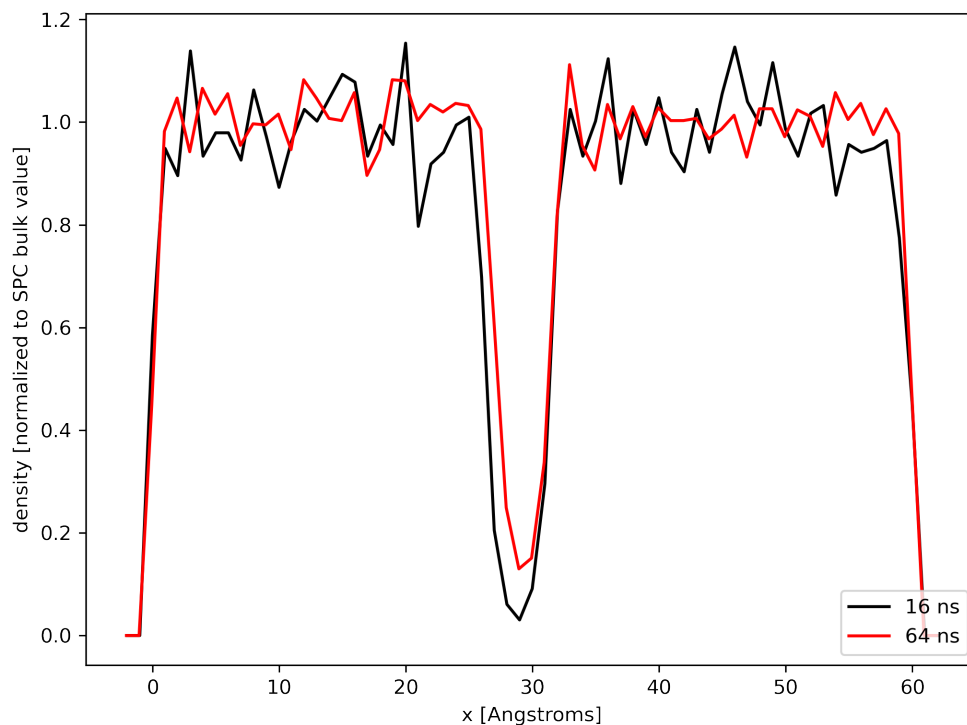


Figure 4.6: Water density along a line for simulations of a methane molecule in bulk water, showing the results of simulations with two different durations. For both simulations, the water density was calculated with a 1 \AA spatial resolution. The depression in the middle is due to the exclusion area of the restrained methane molecule.

4.6 Validation Analyses for Homogenization of Fickian Diffusion

A simple, idealized model was developed to confirm that the homogenization approach can properly account for changes in the effective diffusion coefficient due to varying porosity of the material. This model is sufficiently simple that the effective diffusion coefficient can be readily obtained by other means. In particular, the objective was to create a porous structure with tunable porosity that would have a predetermined effective porosity in each direction. This can be achieved by a cubic unit cell with one square pore in each direction, with the pores intersecting at the center of the unit cell. This geometry, and a finite element mesh thereof, is shown in Figure 4.7. The effective porosity in each direction is the ratio of the pore area to the area of the corresponding face of the unit cell.

The homogenization calculation for Fickian diffusion was performed on this idealized model with a variety of porosity values. The local diffusion coefficient was isotropic and spatially invariant, with a value equal to the bulk diffusion coefficient.

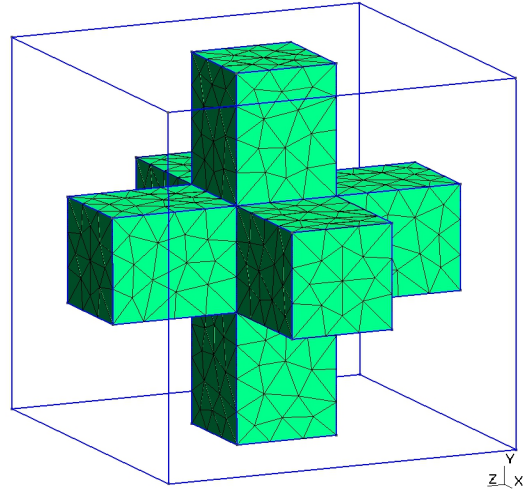


Figure 4.7: Unit cell for the idealized geometry, showing the finite element mesh of the pore space.

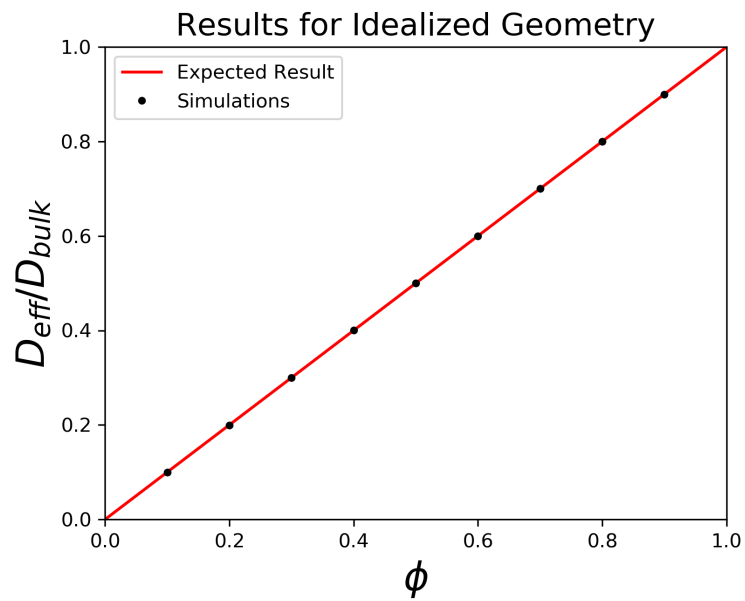


Figure 4.8: Result of homogenization of the idealized geometry.

The results of this set of simulations is shown in Figure 4.8. The effective diffusion coefficients predicted by homogenization matches the assigned effective porosity. Thus, the homogenization procedure successfully produces the expected results for this idealized system.

4.7 Validation Analyses for the Homogenized Smoluchowski Equation

Having validated the homogenized Fickian diffusion model, a validation is needed to confirm the correct solution and interpretation of the homogenized Smoluchowski equation. A simulation of an infinite lattice of cylinders was used for this purpose. This validation problem was previously used for the same purpose in Kekenos-Huskey et al. [69]. Specifically, the problem domain consists of a two-dimensional, square unit cell. A circular inclusion is centered within the cell. Homogenization of the Fickian diffusion equation can predict the effective diffusion coefficient for the unit cell when the inclusion is fully obstructive. This is shown by the black dots in Figure 4.9. Note that the homogenization results are below the upper bounds obtained from two different methods. First, an upper bound was taken assuming that the effective diffusion coefficient (as a fraction of the bulk diffusion coefficient) increases linearly with the porosity. This is an upper bound because the tortuosity and constrictivity factors from Equation 1.19 are both taken as unity in this approach. A better upper bound can be obtained from the Hashin-Shtrikman bounds presented in Auriault et al. [7], which are based on the earlier work in Hashin and Shtrikman [56]. To use this model to validate the homogenized Smoluchowski equation, the fully obstructive inclusion is replaced with a region of variable potential. For low potentials, the effect of the circular region should be minimal, especially at high porosity. But as the potential increases, the results should approach those of the obstructive case. The results shown in Figure 4.9 match these expectations.

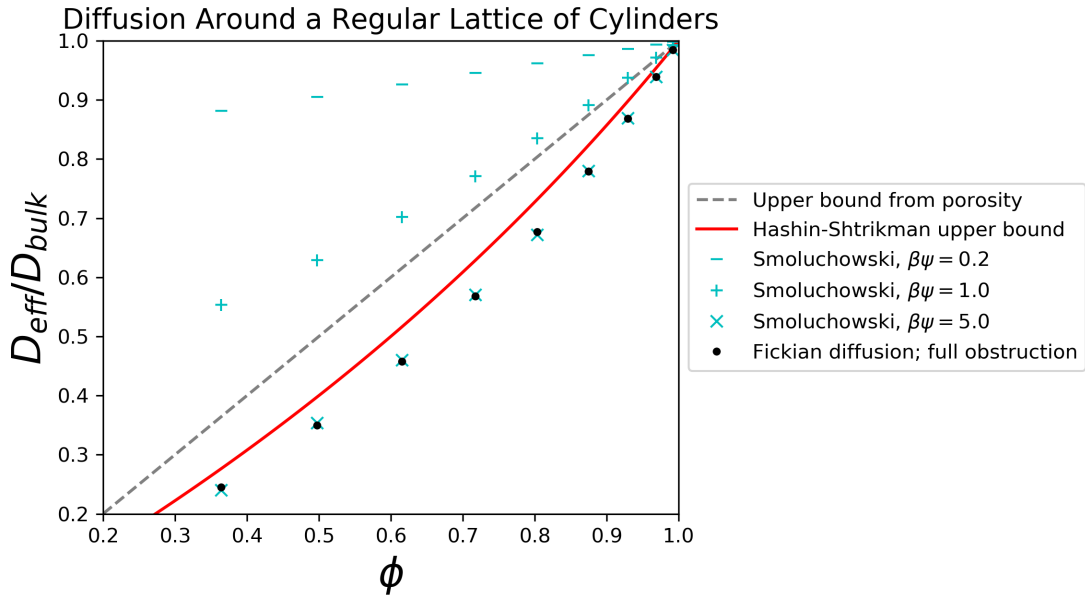


Figure 4.9: Validation of the homogenized Smoluchowski equation using diffusion around a regular lattice of cylinders. As the potential is increased in the Smoluchowski equation, the result approaches the Fickian homogenization result for obstructive inclusions.

In this example, the potential is zero at the boundary of the REV. Consequently, the Ξ functional as described in Appendix D, Section D.12 would be 1. In such a case, \overline{D} and D are equivalent at the larger scale.

4.8 Results of Homogenization for Zeolites

Finite element meshes for the pore space within the BEA and MFI zeolite frameworks were constructed from the relevant crystal structure information files. This process involved the use of GAMer [82, 81]. The resulting mesh for the BEA framework is shown in Figure 4.10.

Homogenization of these meshes was successfully completed for the case of a spatially invariant local diffusion coefficient. The results of this homogenization are contrasted with the validation model in Figure 4.11. The difference between the zeolite homogenization results and the idealized geometry result at the same porosity can be attributed to the geometry of the zeolite pores.

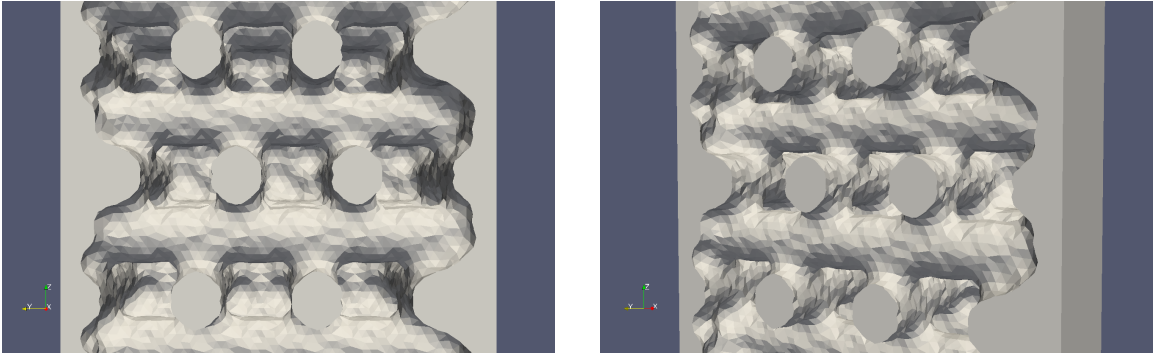


Figure 4.10: Face-on and oblique views of the finite element mesh for the BEA zeolite framework.

The homogenization results can also be compared to the empirical predictions of Equation 1.19. The constrictivity, δ , would be 1 in this case because the local diffusion coefficient is equal to the diffusion coefficient in bulk fluid at all locations inside the pores. In the strictest application of this equation, the geometry of the zeolite pores would influence both the effective porosity, ϵ , and the tortuosity, τ , and both of these factors could vary with direction. In this case, however it is more instructive to use the porosity as the effective porosity in all directions, and attribute all remaining geometrical factors to an effective tortuosity, τ_{eff} , as indicated in Equation 4.11.

$$\frac{D_{\text{eff}}}{D_{\text{fluid}}} = \frac{\phi}{\tau_{\text{eff}}} \quad (4.11)$$

Using Equation 4.11, the effective tortuosity can be computed from the homogenization results. The results of this calculation are shown in Table 4.4

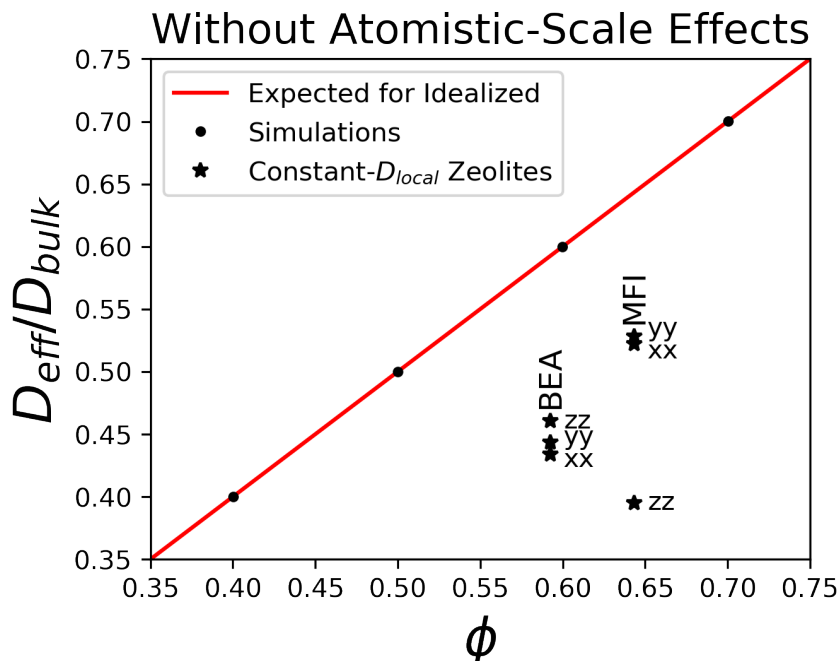


Figure 4.11: Results of homogenization of the zeolite meshes, with constant D_{local} . The red line shows the results of the validation simulation for an idealized geometry discussed in Section 4.6, which shows the effects of porosity alone. The difference between the idealized geometry and the zeolite framework with constant D_{local} reflects the contribution of the tortuosity of the zeolite pores.

Table 4.4: Results of effective tortuosity calculation.

Component	BEA	MFI
xx	1.37	1.23
yy	1.34	1.22
zz	1.29	1.63

The results for the BEA framework are somewhat unexpected. In Figure 4.10, the pores in the x and y directions appear to be generally continuous, while the pores in the z direction have lateral offsets. In contrast, the homogenization results show a higher effective diffusion coefficient (and less effective tortuosity) in the z direction. This result is currently still unexplained. One possibility is that the unexpected behavior is caused by issues with the finite element mesh, as described below.

The finite element mesh poses some challenges for the simulations. First, the mesh boundary is some distance away from the framework supercell boundary, artificially increasing the porosity of the mesh by some amount. Also, the mesh boundary is non-conforming in a periodic sense, so that periodic boundary conditions cannot be applied. Instead, Dirichlet boundary conditions are used as an approximation. If the mesh boundaries are sufficiently far from obstacles to diffusion, this approximation should provide reasonable accuracy. The mesh also contains multiple unit cells in

order to reduce the impact of this issue.

4.9 Results of Molecular Simulations in Silicate Channel

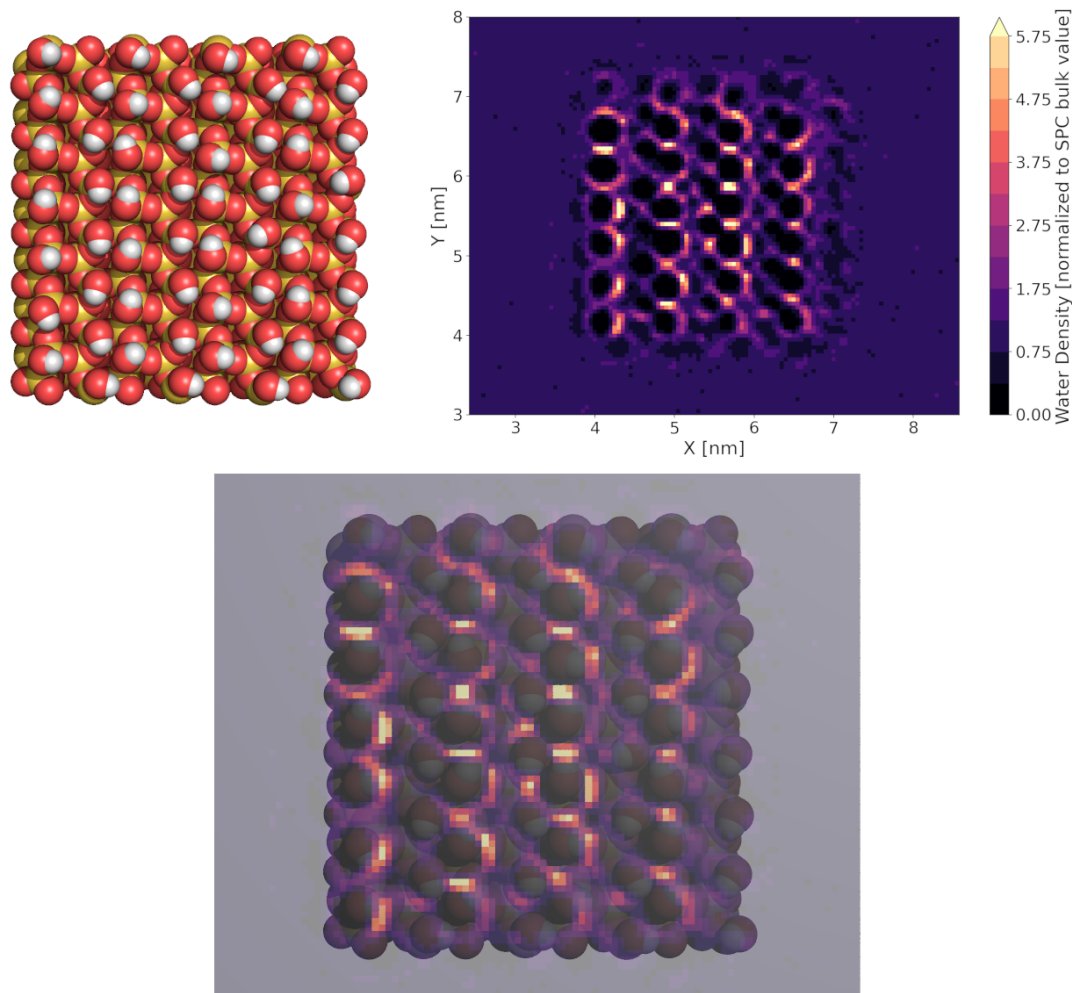


Figure 4.12: Water density near the silicate face from the MD simulation with a channel width of 1.6 nm. Top left: rendering of the silicate face. Top right: water density results for the plane at $z = 4.775$ nm, which is approximately where the water density values reach a local maximum in some areas. Bottom: scaled overlay of the silicate structure and the water density data. The water molecule positions are referenced to the center of their oxygen atoms, so the density is highest around the silanol terminations of the silicate surface. The water density was calculated at a spatial resolution of 0.5 \AA , from 128 nanoseconds of simulation data.

Figures 4.12 and 4.13 show the water density in the MD simulation for the 1.6 nm channel. Figure 4.12 shows the water density calculated near the silicate face, and illustrates that the oxygen atoms of the water molecules are generally attracted to the silanol terminations on the silicate surface. Figure 4.13 shows the water density in the

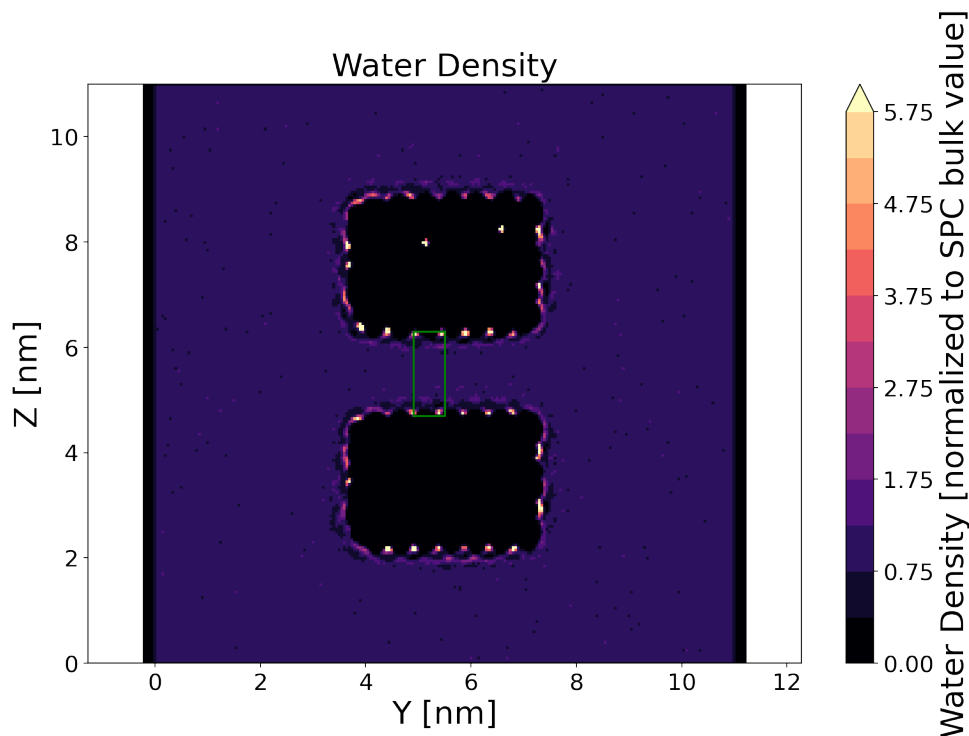


Figure 4.13: Water density in the MD silicate simulation with a channel width of 1.6 nm. The $x = 5.75$ nm plane is shown. The black areas of near-zero water density are occupied by the silicate slabs. Large fluctuations in water density are seen around the silicate. Bulk water density is observed through most of the remaining simulation volume. The green rectangle shows the region of the channel selected for measurement of the local diffusion coefficient and PMF. The water density was calculated at a spatial resolution of 0.5 \AA , from 128 nanoseconds of simulation data.

plane used for subsequent data collection. From this data, a portion of the channel that included areas of both high and low water density was selected for measurement of the local diffusion coefficient and PMF. The portion of the plane selected for such measurements is also shown in Figure 4.13.

Figure 4.14 shows the position ACF obtained at three locations within the 1.6 nm channel. The curve for the bulk simulation described in Section 4.5 is also shown for comparison purposes. The ACF curve for the bulk simulation is more smooth because of the longer simulation duration, 16 ns, compared to 2 ns for the simulations in the channel. The ACF curve that most nearly matches the bulk simulation result is from a point near the middle of the channel. Figure 4.14 also shows the local diffusion coefficient results versus position along the channel. Generally, the local diffusion coefficient appears to approach the bulk value near the middle of the channel, and drop off to roughly half this value at locations closer to the channel surfaces.

Figure 4.15 shows the PMF, local diffusion coefficient, and water density across the 1.6 nm channel. The values are averaged in the y -direction, to demonstrate the general trend in values across the channel, rather than values at specific locations. The local

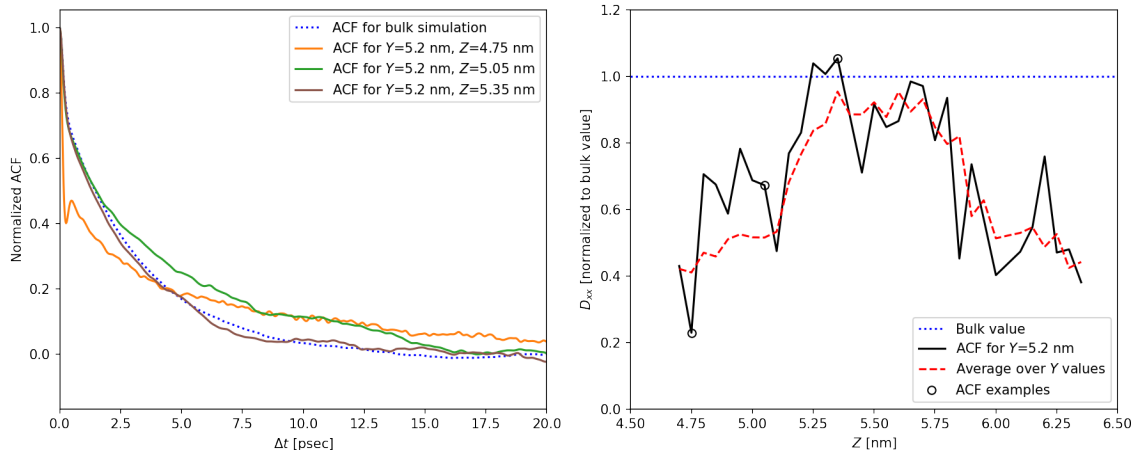


Figure 4.14: Examples of local diffusion coefficient in the 1.6 nm channel. Left: Position autocorrelation function of methane for three different positions in the channel, compared with the bulk simulation result. The bulk simulation curve is more smooth because of a longer simulation duration. Right: Local diffusion coefficient variation across the channel, showing the values along a line across the channel, and also the averages over lines parallel to the channel face. The coordinates are as shown in Figure 4.2.

diffusion coefficient seems to be suppressed near the channel walls, and approaches, but does not match, the bulk diffusion behavior near the center of the channel. This variation in the local diffusion coefficient is symmetric about the channel. In contrast, the PMF appears to be asymmetric within the channel, though still suppressed near the surfaces. The water density seems to oscillate near the channel walls, likely due to solvation layers around the silicate, but the strength of this oscillation reduces quickly with distance from the surface. While not conclusive, these patterns suggest that the local water density, and gradients or other functions thereof, may indeed be a critical driver of variations in the PMF and local diffusion coefficient.

Contour plots of the water density, local diffusion coefficient, and potential of mean force from the MD simulations are shown in Figures 4.16 through 4.20. Each figure shows a different channel width or de-protonation level for the channel. The water density calculation is from 128 nanoseconds of simulation data, at 0.5 Å spatial resolution. D_{local} is taken as the arithmetic average of D_{xx} and D_{yy} values, normalized to the bulk D value. The PMF values are as computed by `wham`. There are similar patterns in all cases. The water density is near its bulk value over most of the channel, but has some localized areas of high water density at nearly consistent spacing along the channel surfaces. This is most likely due to the presence of hydrophilic silanol groups present on the surface in repeating patterns. The local diffusion coefficient results show the same pattern as the results in Figure 4.14 and 4.15: the value is highest near the middle of the channel, where the value is roughly the bulk diffusion coefficient, and then suppressed closer to the channel surfaces. For the 1.2 nm channel width, the local diffusion coefficient appears to be somewhat depressed even near the

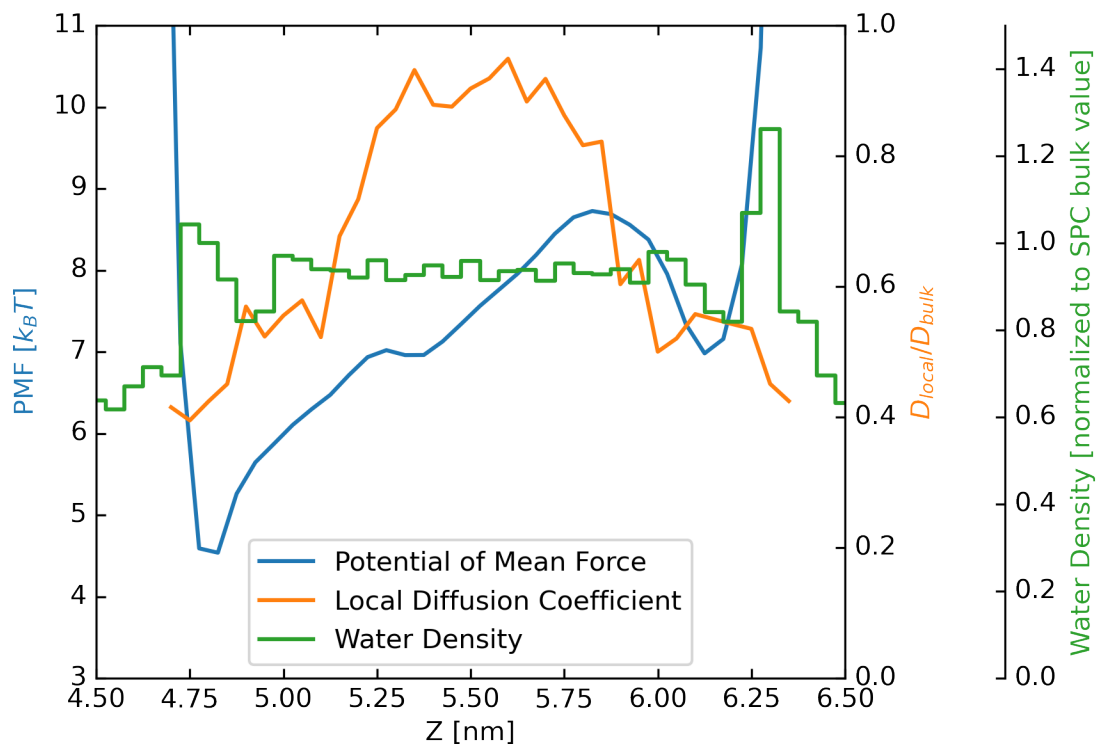


Figure 4.15: Spatial variation of averaged PMF, local diffusion coefficient, and water density in the 1.6 nm channel. The values are averaged over 0.6 nm in the y -direction, for a single value of x , showing the spatial variation in the z -direction (perpendicular to the channel faces).

middle of the channel. The PMF results are generally highest at the channel walls, and lower in the middle of the channel, although localized depressions in the PMF seem to appear at the channel surface in a generally periodic arrangement. In general, the magnitude of the differences in PMF between the highest and lowest values in any channel appear to be larger than would have been expected.

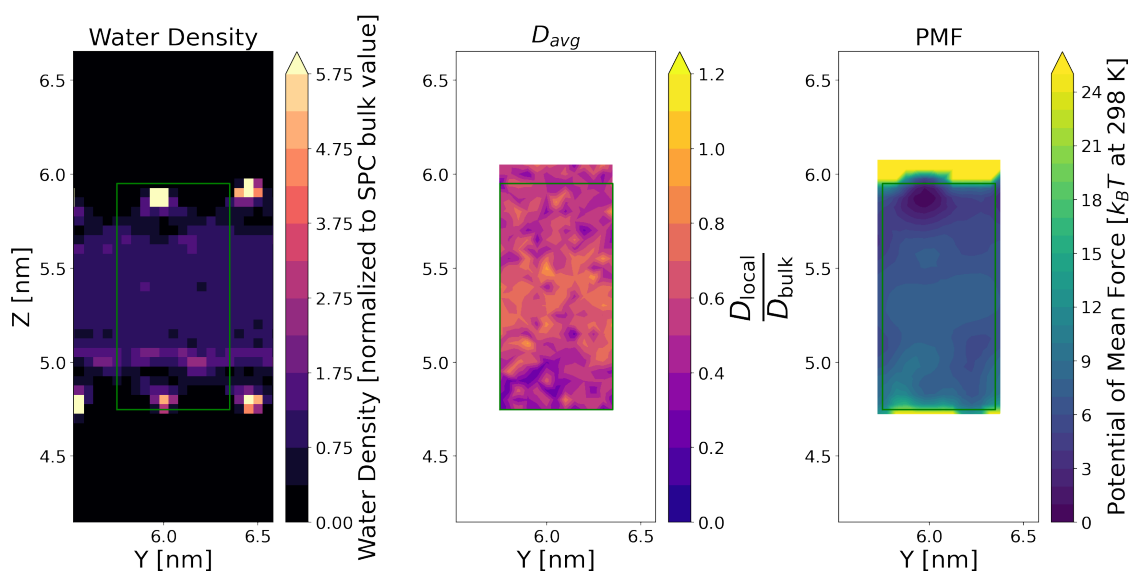


Figure 4.16: Water density, local diffusion coefficient, and potential of mean force for a plane in the 1.2 nm channel, fully protonated. The imposed rectangle shows the limits of data used in the finite element model within the plane.

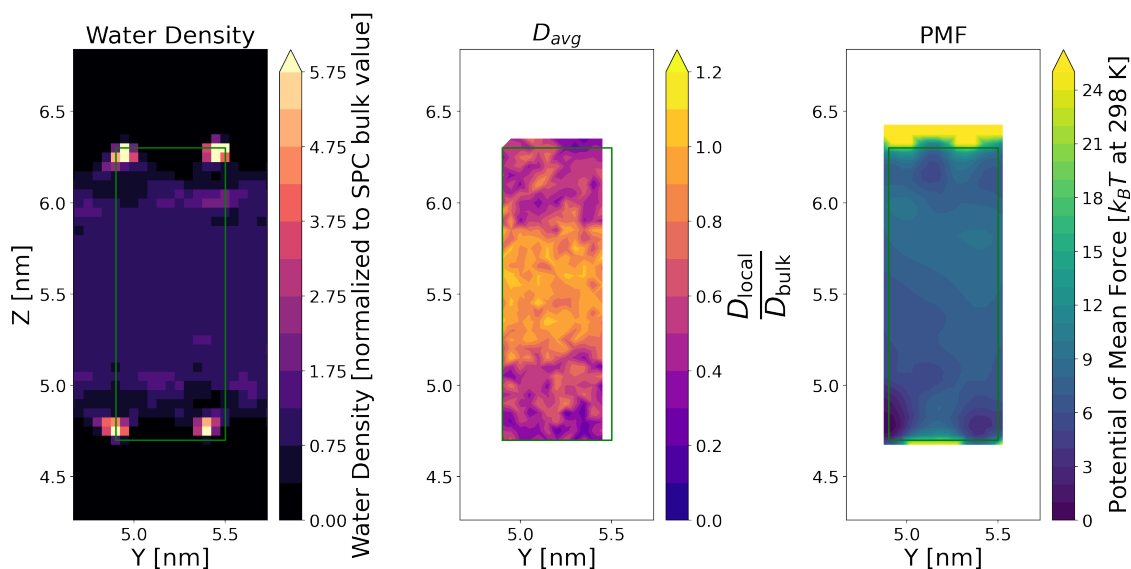


Figure 4.17: Water density, local diffusion coefficient, and potential of mean force for a plane in the 1.6 nm channel, fully protonated. The imposed rectangle shows the limits of data used in the finite element model within the plane.

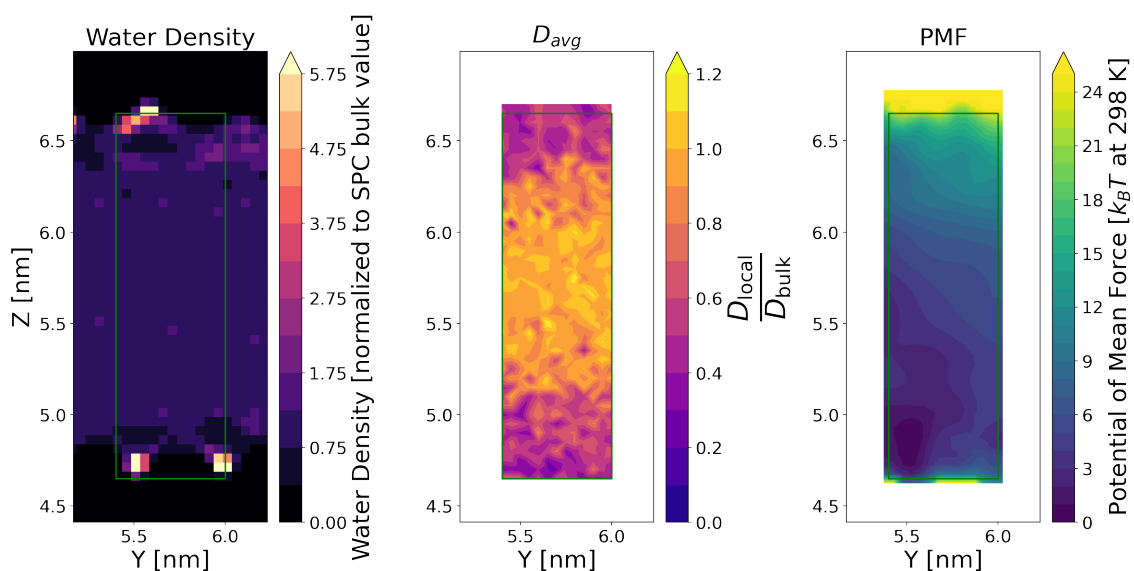


Figure 4.18: Water density, local diffusion coefficient, and potential of mean force for a plane in the 2.0 nm channel, fully protonated. The imposed rectangle shows the limits of data used in the finite element model within the plane.

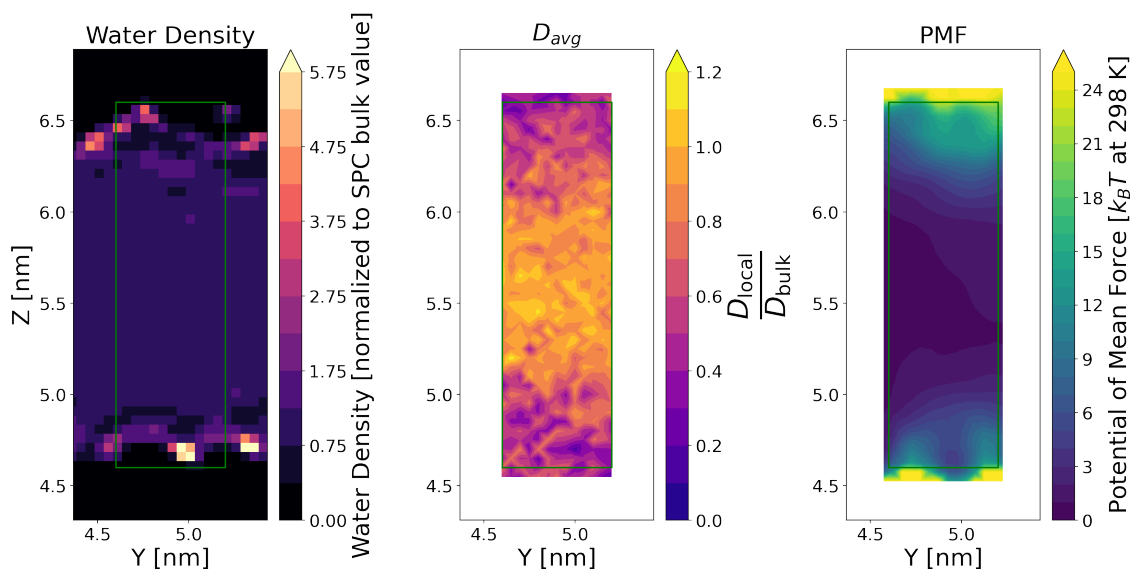


Figure 4.19: Water density, local diffusion coefficient, and potential of mean force for a plane in the 2.0 nm channel, 27% de-protonated. The imposed rectangle shows the limits of data used in the finite element model within the plane.

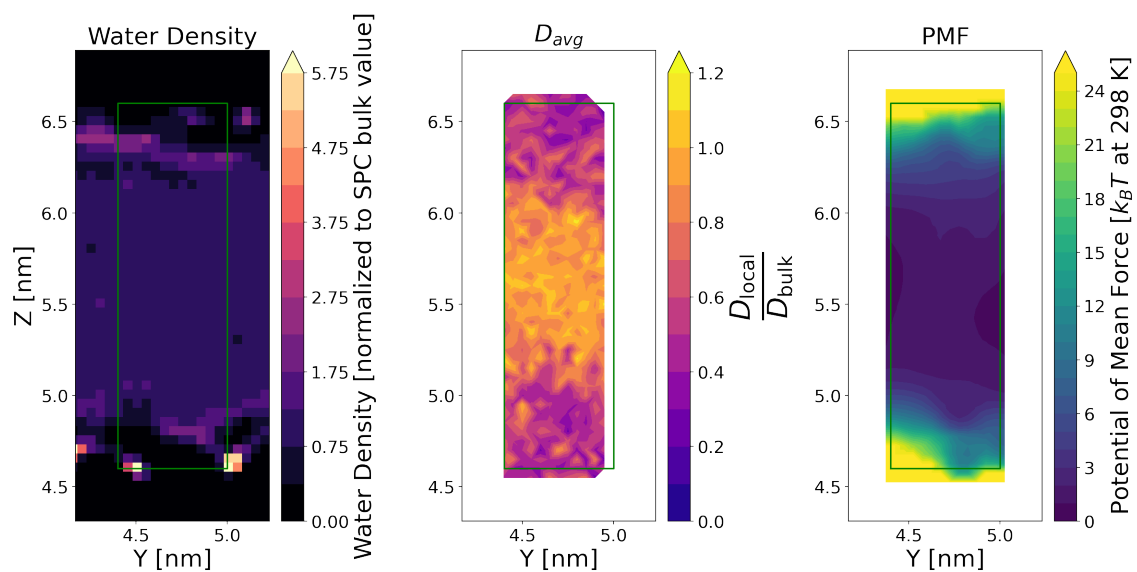


Figure 4.20: Water density, local diffusion coefficient, and potential of mean force for a plane in the 2.0 nm channel, 50% de-protonated. The imposed rectangle shows the limits of data used in the finite element model within the plane.

4.10 Effective Diffusion Coefficients for the Silicate Channel

The PMF results from MD presented in Section 4.9 require some further processing prior to use in homogenization simulations. As noted in Section 2.5, homogenization requires a periodic unit cell. However, the PMF and local diffusion coefficient data from the MD simulations is not periodic over the unit cell selected for homogenization. This can be addressed by reflecting the MD results across the cell boundaries, to produce a symmetric data set. For a two-dimensional unit cell, this requires reflection across two boundaries.

Based on the findings of Appendix D, Sections D.11 and D.12, the effective diffusion coefficient coefficients for the silicate channels were calculated using different methods. First, using the method described in Appendix D, Section D.8, a flux-based calculation was performed by solving the steady-state Smoluchowski equation. Next, the result from homogenization of the Smoluchowski equation using the Slotboom transformation was also computed. The results of homogenization are presented here both with and without division by Ξ as described in Appendix D, Section D.12.

Figure 4.21 presents the effective diffusion coefficient results for different channel wall separation distances, and Figure 4.22 presents the results for different levels of silica surface protonation.

The effective diffusion coefficient results computed by homogenization without the application of the Ξ factor differ markedly from the results using the other approaches. This is in agreement with the interpretation of the homogenization results as a gauge-dependent effective \bar{D} , rather than a physically measurable effective diffusion coefficient. Indeed, the results from the flux-based calculation and the homogenization results after application of Ξ are in much better agreement. Still, the results of the flux-based calculation and the results of homogenization after the application of Ξ are not identical. The possibility that the functional form of Ξ used here is not generally valid cannot be ruled out, but the differences here are small enough that other possibilities may be considered. In particular, Ξ depends on an exponential function of the potential. Small differences between the actual potential and the FEM interpolation of the potential could be greatly amplified by this exponential dependence, reducing the accuracy with which Ξ can be evaluated in the FEM approach. The difference in the results for the 1.2 nanometer channel, however, seem larger than would be expected if this was the only source of disagreement. An alternative possibility is that the definition of the average gradient used in the flux-based calculation of Appendix D, Section D.12 is not compatible with the large-scale steady-state solution of the Smoluchowski equation. An alternative definition would not only alter the results of the flux-based calculation here, but might also give another form of Ξ that would be more generally appropriate.

Overall, the results that use a constant PMF are physically reasonable, and the different methods are in agreement. However, the results for the simulations that use the MD-derived PMF values are not as physically reasonable. This is true for both methods of evaluating the effective diffusion coefficient coefficient. As such, it would seem that the PMF values obtained from the MD simulations are not physically reasonable. As noted in Section 4.9, there was more variation in the PMF throughout

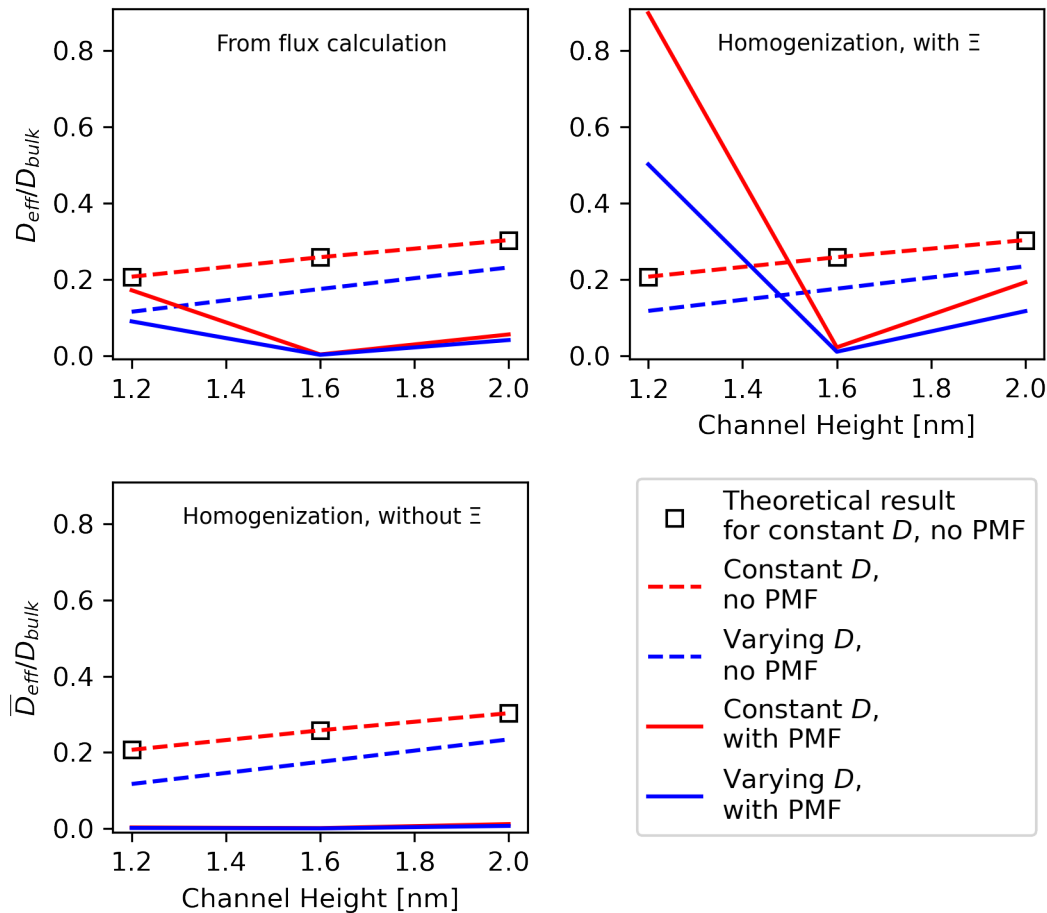


Figure 4.21: Predicted effective diffusion coefficient for a silicate channel as a function of wall separation. Upper left: results from a flux calculation without homogenization. Upper right: results from homogenization and application of Ξ . Lower left: results from homogenization as gauge-dependent \bar{D} , prior to application of Ξ . Lower right: legend. For the case of a uniform diffusion coefficient, the problem can be solved analytically (open squares). The results shown with red lines represent simulations with a constant local diffusion coefficient, while results with blue lines represent simulations where the local diffusion coefficient was obtained from the MD simulations. Dashed lines represent simulations where the PMF was constant (zero), while solid lines represent simulations where the PMF was obtained from the MD simulations.

the channel than would have been expected. This results in larger forces on the diffusing particles, leading to greater influence of the PMF on the effective diffusion coefficient than would have been expected.

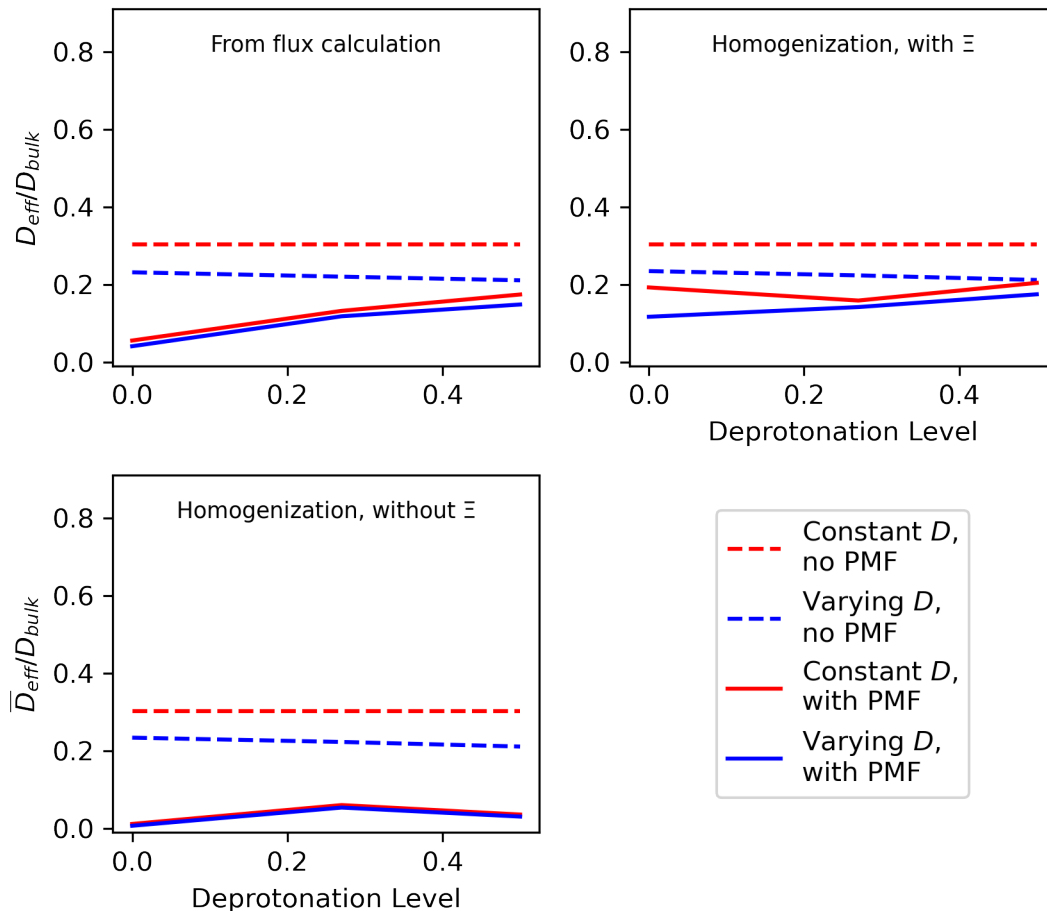


Figure 4.22: Predicted effective diffusion coefficient for a silicate channel as a function of de-protonation level. Upper left: results from a flux calculation without homogenization. Upper right: results from homogenization and application of Ξ . Lower left: results from homogenization as gauge-dependent \bar{D} , prior to application of Ξ . Lower right: legend. The results shown with red lines represent simulations with a constant local diffusion coefficient, while results with blue lines represent simulations where the local diffusion coefficient was obtained from the MD simulations. Dashed lines represent simulations where the PMF was constant (zero), while solid lines represent simulations where the PMF was obtained from the MD simulations.

4.11 Discussion and Conclusion

This chapter has illustrated the use of multi-scale modeling techniques in a multi-physics setting. Again, the analyses used progressed from simple analyses that could be validated using other approaches to applications in more complex settings. The ultimate goal is the application of these techniques to the problem of methane conversion into methanol in an aqueous reaction-diffusion system with zeolite catalysts. Toward that end, there are additional features that will need to be included.

As noted in Section 4.8, the ability to create accurate and robust finite element

meshes of the pore space in zeolite crystals is a critical requirement for the homogenization analyses. The techniques to develop such meshes lie in the realm of computational geometry. While the `gmsh` software package might not be capable of producing the desired meshes, other software packages such as `CGAL` could potentially be used.

The MD simulations used to generate the results in Section 4.9 were 2 ns in duration. Longer simulation durations could potentially reduce the amount of statistical “noise” in the results. Towards this end, the adequacy of the simulation durations could be assessed by using block averaging techniques to obtain estimates for the uncertainty in the local diffusion coefficient and PMF results. This information would be helpful for investigations into why the PMF data gives physically unreasonable effective diffusion coefficient results.

Common zeolite catalysts differ from the silicate channel not only in geometry, but also in chemical composition. For example, one common zeolite material ZSM-5, is an aluminosilicate zeolite of the MFI framework [74]. In fact, various chemical compositions of ZSM-5 have been prepared [111]. The force field of Emami et al. [43][44] does not have parameters for all the atomic species present in this wide variety of materials. For detailed computational studies of particular zeolitic materials, material-specific force fields derived from electronic structure calculations may be required.

One restriction of the ACF calculation method for the local diffusion coefficient as presented in Sections 4.2 and 4.4 is that it can only compute the diagonal terms of the diffusion coefficient matrix. This is not a significant issue for the silicate channel geometry described in Section 4.3, as the principal axes of the diffusion coefficient matrix are very likely to match the coordinate axes of the system, such that the off-diagonal terms are indeed zero. However, the geometry of the zeolite frameworks is more complicated, and so the principal axes may differ from the coordinate axes at some locations in the system. Without an estimate of the off-diagonal terms, the errors created by their omission cannot be detected. If an extension of the ACF calculation procedure for off-diagonal terms cannot be found in the literature, there is a relatively simple approach that can be used without excessive additional computation. Specifically, rotation of the coordinate system in which the methane trajectories are expressed would allow calculation of the diagonal terms of the matrix in this rotated coordinate system. The off-diagonal terms can be computed from estimates of the diagonal terms in two different coordinate systems.

Chapter 5 Summary, Conclusions, and Speculation

5.1 Summary and Review: Successes and Limitations of the Methods

This work has focused on the application of multi-scale multiphysics simulations to diffusive transport models in biochemical systems and aqueous-phase chemical processing. These same techniques can be applied to a wide variety of other systems, and there are related techniques that are also available. The models described herein were successful in some ways, but limited in others.

The FEM does provide an accurate, robust, and computationally efficient means of solving not only the Fickian and Smoluchowski diffusion equations, but also the corrector problems and REV integrals required by homogenization theory. The reactive boundary condition provided a relatively simple means of incorporating chemical reactions into a diffusion model. Difficulties encountered in the FEM solutions were largely from specific limitations of the software and hardware, rather than general issues with the approach itself. The success in the application of the FEM illustrates why this approach has grown so incredibly popular in a wide variety of applications.

Homogenization theory was very successful here in obtaining effective diffusion coefficients for purely Fickian diffusion problems. In settings with an imposed potential that also influenced the transport behavior of the system, homogenization of the Smoluchowski equation using the Slotboom transformation was complicated by the need to reverse the Slotboom transformation for the larger-scale result. More general methods for the post-homogenization inverse transformation require further investigation.

While only limited use was made herein of MD techniques, the effectiveness of MD approach can be assessed for the problems covered herein. With suitable techniques for post-processing molecular trajectories, local properties of interest within the system can be obtained using this technique. However, there were two significant limitations encountered. First, the force fields used by the MD simulations are intended to work for obtaining certain types of results under particular sets of conditions. As experienced here, using a force field under different conditions, or for obtaining different result variables, can cause discrepancies with experimental observations. Secondly, the MD simulations were computationally demanding. Typical MD performance rates encountered here were around 100 nanoseconds per node, per day, using nodes with multiple CPUs and GPUs. Each simulation of a single methane position had a duration of 2 nanoseconds. Over the various channel widths and deprotonation levels, a total of 2380 different methane positions were simulated. The total simulation time was thus 4.76 microseconds, requiring roughly 47.6 node-days of computation. The actual calculation duration was shortened by the simultaneous use of multiple nodes. As a ratio of two units of time, the unit of nanoseconds per day is actually a dimensionless number. Specifically, as there are 8.64×10^{13} nanoseconds in 24 hours, the unit of nanoseconds per day is a dimensionless value of approximately 1.16×10^{-14} . This means that a simulation running at a rate of 100 nanoseconds per

day is running at a rate of 1.16×10^{-12} times the speed of reality.

5.2 Speculation: The Possibility of Novel Algorithms

Force-field MD has proved to be a tremendously powerful technique, and is now routinely used to study biochemical systems as well as systems like the silicate channel considered here. One limitation of this technique is that events such as chemical reactions, which alter the electronic structure, would also require a change in the force field for proper evaluation. For example, models to assess the catalytic efficiency of a given system at the macroscopic scale would encounter this limitation. While electronic structure investigations alone can provide useful insight into such systems, the kinds of statistical information provided by MD simulations requires more particles than can reasonably be included in an electronic structure calculation. Methods for allowing force fields to accurately represent changes such as chemical reactions are under active investigation [117]. An alternative approach is to combine the methods of electronic structure calculations into dynamic simulations of chemical systems. This approach is known as *ab-initio* MD [62].

Of course, both electronic structure calculations and MD simulations are computationally intensive. While the techniques employed in *ab-initio* MD calculations have better computational efficiency than simple combinations of electronic structure and MD simulations, the computational demands are still greater than for force-field MD, which is already significant. The computational intensity of *ab-initio* MD restricts the time and length scales to which it can be applied [1].

One possible way of attaining both greater accuracy and greater speed in molecular simulations may be to incorporate multi-scaling techniques at the level of the fundamental algorithms employed. For example, multi-scaling in the time domain, if it could be achieved, might allow simulations to use significantly larger time-steps. Multi-scaling in the spatial domain might allow the approximation of an array of discrete particles by means of spatially-varying functions, which could then be treated using FEM and similar approaches. One consequence of such techniques might be that additional physical behaviors that currently emerge from the models would have to be explicitly included instead, making use of concepts from multiphysics models. While purely hypothetical, such ideas suggest that there may be meritorious approaches to improving both accuracy and speed that have not previously been investigated.

For any such algorithm attempting to simultaneously improve both the accuracy and speed of molecular simulations, the following features would be desirable. First, the algorithm should be designed for implementation on parallel hardware (multiple CPUs and possibly even GPUs). The era of single-process algorithms is rapidly drawing to a close. Secondly, to the extent possible, the approximations employed in the algorithm should be tunable, such that the end user can select the level of approximation best suited for the computational resources available and the required level of accuracy. Next, the effectiveness of the algorithm should be judged, at least in part, by the scaling behavior of its time and resource requirements with respect to the size of the simulated system. The system size includes variables such as the number of particles, the system volume, and the duration of the simulation. Similarly,

the effectiveness of the algorithm should also be judged by the the scaling behavior of its time and resource requirements with respect to the reciprocal of some measure of the allowable error in the calculation. For example, a calculation that halves the error may double the time or memory requirements, but should not quadruple them. Finally, an ideal algorithm would be applicable for simulations at both temperatures above absolute zero and at temperatures approaching it, even if the computational resources required are not the same for such calculations. These recommendations could be considered as design goals in the development of algorithms.

An algorithm meeting the description above may not be possible. But searching for such algorithms may not be substantially more difficult than searching for continued improvements to the existing algorithms. The electronic structure and MD algorithms that exist today are the result of decades of optimization. As such, these algorithms may be approaching their eventual local optimum in terms of their accuracy and computational efficiency. This would mean that continued efforts to improve the existing algorithms might offer diminishing returns. Exploring the vast search space of other possible algorithms may be the only way to continue to achieve significant improvement. Such situations are known as an *inventor's paradox*: sometimes more ambitious goals are easier to obtain than smaller ones [101].

5.3 Conclusion: Continuing the Search for Useful Approximations

The history of human civilization is sometimes divided into eras by the advancement in the kinds of materials that could be created. These divisions are illustrated by terms such as Stone Age, Bronze Age, and Iron Age, each of which is named after a material newly available during the era [26]. While such divisions are not applied to modern civilization, the ability to create materials with desired properties is critical to many fields of engineering and technology.

The increasing need for advanced materials results in an increasing need to be able to understand and predict their properties. The methods discussed herein are one possible approach to this process: combining theories describing different physical phenomena and linking the predicted behavior at one scale of time and length to characteristic properties at a larger scale. Other approaches include the direct formulation of theories at a single scale to explain and predict observed phenomena. More recently, machine learning and artificial intelligence techniques have been applied to similar problems [35]. (In fact, some electronic structure calculations performed by the author were used as training input for such a model by Khmaissia et al. [73].)

The chief advantage of the multi-scale multiphysics approach is that the necessary physical laws are already well-established. The chief difficulties are the approximations necessary to render problems computationally tractable without sacrificing the desired level of accuracy. Indeed, as noted by Dirac in 1929 [41]:

The underlying physical laws necessary for the mathematical theory of a large part of physics and the whole of chemistry are thus completely known, and the difficulty is only that the exact application of these laws leads to equations much too complicated to be soluble. It therefore be-

comes desirable that approximate practical methods of applying quantum mechanics should be developed, which can lead to an explanation of the main features of complex atomic systems without too much computation.

Nearly a century later, the search for such approximate methods continues.

Appendices

Appendix A Glossary of Acronyms

ACF Autocorrelation Function	viii, 47, 48, 51, 52, 53, 54, 55, 63, 72, 119
ADP Adenosine Diphosphate.....	41, 85
AMP Adenosine Monophosphate.....	41, 85
ATP Adenosine Triphosphate.....	41, 44, 85
DFT Density Functional Theory	iii, iv, 16, 17
FEM Finite Element Method	iii, v, 14, 19, 20, 21, 22, 52, 69, 73, 74, 80, 83, 86, 87, 92, 95, 96
HF Hartree-Fock.....	16, 17, 85
LPB Linearized Poisson-Boltzmann.....	32, 33, 34
MC Monte Carlo.....	17, 18, 19, 87
MD Molecular Dynamics ..	iii, viii, 17, 18, 19, 44, 46, 47, 48, 52, 53, 62, 63, 64, 69, 70, 71, 72, 73, 74, 75, 85, 86, 87, 88
MSD Mean-Squared Displacement	vii, viii, 9, 12, 47, 48, 51, 53, 54, 55, 83, 85, 119
NPT Number, Pressure, and Temperature.....	19, 51
NVE Number, Volume, and Energy	19
NVT Number, Volume, and Temperature.....	19, 51
PDE Partial Differential Equation .	14, 19, 20, 21, 22, 23, 52, 83, 85, 86, 87, 88, 91, 93, 101
PME Particle Mesh Ewald	18, 51
PMF Potential of Mean Force.....	46, 48, 51, 63, 64, 65, 69, 70, 71, 72
QMC Quantum Monte Carlo	16, 17, 88
REV Representative Elementary Volume..	22, 23, 24, 52, 60, 73, 82, 85, 86, 88, 92, 93, 94, 103, 109, 110, 112, 120, 121, 127, 128
VACF Velocity Autocorrelation Function.....	9
WHAM Weighted Histogram Analysis Method.....	51, 89

Appendix B Glossary of Mathematical Notation

Notation	Description	Page List
$\langle \dots \rangle$	Ensemble average of the quantity within the brackets	9, 12, 47, 51, 83, 119, 120
$\llbracket \dots \rrbracket$	Units or dimensions of the quantity within the brackets	2, 8, 12, 14, 27, 47, 79, 80, 81, 82, 83, 84, 118, 119
$ \dots $	Magnitude or volume of the quantity within the bars	22, 95, 109, 113, 120, 121, 125, 126, 129
#	Units or dimensions of an integer quantity	12, 81, 82, 83
1	Units of a dimensionless quantity	12, 80, 83
E	Units or dimensions of energy, equivalent to $\llbracket \frac{ML^2}{T^2} \rrbracket$	14, 47, 79, 80, 118
F	Units or dimensions of force, equivalent to $\llbracket \frac{ML}{T^2} \rrbracket$	8, 47, 118
L	Units or dimensions of length	2, 8, 12, 14, 27, 47, 79, 80, 81, 82, 83, 84, 118, 119
M	Units or dimensions of mass	8, 47, 79, 80, 118
Q	Units or dimensions of electric charge	80, 84
T	Units or dimensions of time	8, 12, 14, 47, 79, 80, 81, 82, 118
∂_t	Partial derivative with respect to time $\llbracket \frac{1}{T} \rrbracket$	5, 6, 8, 9, 14, 47, 90, 91, 92, 117, 118, 119
∂_j	Gradient operator in index notation $\llbracket \frac{1}{L} \rrbracket$	5, 6, 7, 8, 10, 11, 12, 22, 32, 33, 47, 90, 91, 92, 94, 95, 96, 97, 98, 99, 101, 102, 103, 104, 109, 110, 111, 112, 113, 114, 116, 117, 118, 120, 121, 125, 126, 127, 128

Notation	Description	Page List
β	$\frac{1}{k_B T}$ for Boltzmann constant k_B and absolute temperature T $\llbracket \frac{1}{E} \rrbracket$	7, 8, 47, 53, 91, 116, 119, 121, 123, 124, 125, 126, 127, 128, 129, 130
$\partial\Omega$	The entire boundary of the problem domain, a closed surface for $N_d=3$, a closed curve for $N_d=2$	117
ϵ	Separation of scales parameter, $\frac{\ell_c}{L_c}$ $\llbracket 1 \rrbracket$	22
ϕ	Free volume fraction (porosity), ratio of volume of voids to total volume $\llbracket 1 \rrbracket$	10, 29, 30, 31, 60, 87
$\phi_M(x_i)$	Pre-defined basis function used in the FEM approximation	19, 20, 21
Γ	A specific boundary of the problem domain, a surface for $N_d=3$, a curve for $N_d=2$	6, 81, 82, 92, 99, 129
Γ_D	A boundary surface of the problem domain with a Dirichlet boundary condition imposed	92
Γ_N	A boundary surface of the problem domain with a Neumann boundary condition imposed	92, 96, 97
κ	A constant appearing in the linearized Poisson-Boltzmann equation $\llbracket \frac{1}{L} \rrbracket$	32, 80
λ_D	The inverse of κ $\llbracket L \rrbracket$	32
ξ	Friction coefficient for viscous drag force $\llbracket \frac{M}{T} \rrbracket$	8, 47, 118, 119, 120
Ξ	Hypothetical conversion factor between effective D and \bar{D} from homogenization $\llbracket 1 \rrbracket$	60, 69, 70, 71, 121, 129, 130
Φ	Electric potential as a scalar field $\llbracket \frac{E}{Q} \rrbracket$	32, 116
w_j	The corrector function in the corrector problem from homogenization, with opposite sign of χ_j $\llbracket L \rrbracket$	95, 97
χ_j	The corrector function in the corrector problem from homogenization $\llbracket L \rrbracket$	22, 80, 94, 95, 96, 97, 101, 102, 103, 104, 105, 109, 110, 111, 112, 113, 114, 120, 121, 125, 126, 127, 128
Ψ	Potential energy field from unspecified source $\llbracket E \rrbracket$	7, 8, 91, 121
Ω	All space within the problem domain, a volume for $N_d=3$, an area for $N_d=2$	20, 21, 22, 80, 91, 92, 94, 95, 96, 97, 109, 113, 117, 119, 120, 121, 125, 126
\mathcal{A}	Arbitrary linear differential operator	20, 21

Notation	Description	Page List
c	Concentration of a substance as a scalar field $\left[\left[\frac{\#}{\text{L}^{(N_d)}} \right] \right]$	5, 6, 7, 8, 10, 11, 33, 90, 93, 94, 98, 99, 100, 105, 106, 107, 108, 109, 122, 123, 124, 127
\bar{c}	Slotboom-transformed concentration field $\left[\left[\frac{\#}{\text{L}^{(N_d)}} \right] \right]$	8, 33, 34, 122, 123, 124, 126, 127
c_S	Concentration of species S , as a scalar field $\left[\left[\frac{\#}{\text{L}^{(N_d)}} \right] \right]$	6, 12, 90, 91, 92, 116, 117
\bar{c}_S	Slotboom-transformed concentration field of species S $\left[\left[\frac{\#}{\text{L}^{(N_d)}} \right] \right]$	116, 117, 118
$d\Gamma$	Differential element for domain boundary Γ , area for $N_d=3$, length for $N_d=2$ $\left[\left[\text{L}^{(N_d-1)} \right] \right]$	6, 83, 92, 96, 97, 99, 117, 118, 129
$d\Omega$	Differential domain element, volume for $N_d=3$, area for $N_d=2$ $\left[\left[\text{L}^{N_d} \right] \right]$	20, 21, 22, 91, 92, 95, 96, 97, 109, 113, 117, 119, 120, 121, 125, 126
D	Fickian diffusion coefficient $\left[\left[\frac{\text{L}^{(N_d-1)}}{\text{T}} \right] \right]$	5, 6, 7, 8, 9, 11, 22, 40, 47, 48, 52, 60, 80, 91, 92, 93, 94, 95, 96, 97, 98, 99, 100, 101, 102, 103, 104, 105, 109, 110, 113, 114, 116, 121, 130
\bar{D}	Slotboom-transformed Fickian diffusion coefficient $\left[\left[\frac{\text{L}^{(N_d-1)}}{\text{T}} \right] \right]$	8, 33, 34, 52, 60, 69, 70, 71, 80, 117, 120, 121, 123, 125, 127, 130
\bar{D}_S	Slotboom-transformed Fickian diffusion coefficient of species S $\left[\left[\frac{\text{L}^{(N_d-1)}}{\text{T}} \right] \right]$	116, 117, 118
D_{local}	Diffusion coefficient at a given point in the pore space of a porous medium $\left[\left[\frac{\text{L}^{(N_d-1)}}{\text{T}} \right] \right]$	viii, 61, 64

Notation	Description	Page List
D_{eff}	Effective diffusion coefficient for a porous medium $\left[\frac{\text{L}^{(N_d-1)}}{\text{T}} \right]$	9, 10, 22, 24, 60, 94, 95, 98, 99, 100, 101, 104, 105, 109, 110, 112, 113, 120, 121, 123, 125, 126, 127, 128, 129, 130
f_R	Functional form of rate law for reaction R (such as a product of all reactant concentrations raised to a power), units vary depending on the form of the rate law, $\llbracket k_R f_R \rrbracket = \left[\frac{\#}{\text{L}^{(N_d)\text{T}}} \right]$	82, 90, 91, 92
g_{Sj}	A generalization of the concentration gradient vector for species S , used to provide a general equation representing either Fickian or Smoluchowski diffusion $\left[\frac{\#}{\text{L}^{(N_d+1)}} \right]$	91, 92
i, j, k	Index over spatial dimensions, starting at 1 unless specified otherwise	5, 6, 7, 8, 11, 20, 33, 79, 91, 101
j_i	Flux of a substance as a vector field $\left[\frac{\#}{\text{L}^{(N_d-1)\text{T}}} \right]$	5, 6, 7, 8, 10, 11, 98, 99, 100, 123
j_{Si}	Flux of species S , as a vector field $\left[\frac{\#}{\text{L}^{(N_d-1)\text{T}}} \right]$	6, 12, 90, 91, 116, 117
J_Γ	Total flux of a substance through surface Γ as a scalar value $\left[\frac{\#}{\text{T}} \right]$	6, 99
$J_{\Gamma S}$	Total flux of species S through surface Γ , as a scalar value $\left[\frac{\#}{\text{T}} \right]$	6, 39, 40
k_R	Reaction rate coefficient for reaction R , units vary depending on the form of the rate law, $\llbracket k_R f_R \rrbracket = \left[\frac{\#}{\text{L}^{(N_d)\text{T}}} \right]$	82, 90, 91, 92
ℓ_c	Characteristic length for the smaller scale (REV) in homogenization $\llbracket \text{L} \rrbracket$	22, 80
L_c	Characteristic length for the larger scale in homogenization $\llbracket \text{L} \rrbracket$	22, 80
M	Index over the FEM interpolating functions	20

Notation	Description	Page List
n_{Γ_i}	Unit normal vector to the boundary element $d\Gamma$ $[[L]]$	6, 92, 96, 97, 117
N_d	Number of spatial dimensions $[[\#]]$	9, 11, 12, 14, 17, 54, 80, 81, 82, 83, 119
N_{dof}	Number of degrees of freedom in the algebraic system of the FEM approximation $[[\#]]$	19, 20, 21, 83
$N_{\text{reactions}}$	Number of different chemical reactions considered $[[\#]]$	90, 91, 92
N_{species}	Number of different chemical species in solution $[[\#]]$	12, 90, 91
p_{RS}	Stoichiometric coefficient for species S on product side of reaction R , must be zero or larger $[[1]]$	83, 90
q	The position of a particle in one of the N_d Cartesian coordinate variables $[[L]]$	9, 47, 51, 83, 118, 119, 120
$\langle q^2 \rangle$	Mean-Squared Displacement (MSD) of a single coordinate for a particle $[[L^2]]$	47, 51, 119, 120
$R(x_i)$	Residual error in the PDE from the FEM approximation	20
R	Index over the chemical reactions	82, 83, 90, 91, 92
$\langle r_i r_i \rangle$	Radial Mean-Squared Displacement (MSD) of particle $[[L^2]]$	9, 12
r_{RS}	Stoichiometric coefficient for species S on reactant side of reaction R , must be zero or larger $[[1]]$	83, 90
n_{RS}	Net stoichiometric coefficient for species S in reaction R , $p_{RS} - r_{RS}$, may be negative, zero, or positive $[[1]]$	90, 91, 92
S	Index over the diffusing species	6, 12, 81, 82, 83, 84, 90, 91, 92, 116, 117
$u(x_i)$	Exact solution to a PDE	20
$\tilde{u}(x_i)$	Approximate solution to a PDE	19, 20, 21
$v(x_i)$	An arbitrary test function	20, 95, 96, 97
$v_L(x_i)$	One of N_{dof} test functions used in the FEM approximation	21
v_S	Scalar test function associated with species S	91, 92, 117, 118

Notation	Description	Page List
x_i	Spatial coordinate vector $[[L]]$	19, 20, 21, 47, 80, 83, 118
X_S	Chemical symbol for species S	90
z_S	Electric charge of species S $[[Q]]$	116

Appendix C Glossary of Terms

- adenosine** A nucleotide molecule, also used in ATP, ADP, and AMP. 41
- adsorption** A process where molecules are attracted to the surface of a solid, in contrast to absorption, where the molecules are drawn into the bulk of the solid. 46
- anisotropy** A condition in which behavior varies with direction. 4, 91, 92, 98
- anomalous diffusion** Diffusion where the MSD is not linearly proportional to time, so a Fickian diffusion coefficient cannot be defined. 12
- barostat** In MD simulations, a procedure of varying the volume of the system to maintain a constant pressure. 19
- basis set** A set of single particle wave-functions used to define many-particle wave-functions. 16, 85
- behavioral properties** Material properties that quantify the response of a material to different imposed conditions. 1
- binary diffusion** Diffusion involving only two chemical species. 12
- CGAL** “Computational Geometry Algorithms Library”, a software library for computational geometry (see <https://www.cgal.org/>). 72
- coarse-graining** An approach of solving a large-scale problem by reducing the resolution of the solution. 21
- constitutive law** A mathematical model that quantifies a relationship between a condition imposed on a material and some response. 4
- corrector function** The solution of the corrector problem in homogenization. 22, 80, 94, 95, 97, 102
- corrector problem** A PDE to be solved on the REV in homogenization. 22, 24, 52, 80, 92, 94, 95, 96, 101, 114
- correlation energy** The energy difference between the true electronic ground state and the HF ground state in the limit of a large basis set. 16
- descriptive properties** Material properties defining the nature, structure, or composition of a material. 1

- diagonalize** To transform a symmetric, positive-definite matrix such that its only nonzero entries are on the diagonal. 11
- Dirichlet boundary condition** A PDE boundary condition specifying the value of the solution at a boundary location. 21, 40, 80, 92
- discretization** Transformation of a problem to find a continuous function to a problem of finding a finite set of discrete values. 19
- effective diffusion coefficient** The diffusion coefficient appropriate for use at a larger analysis scale than the REV. 9, 22, 23, 24, 25, 29, 30, 35, 39, 46, 52, 58, 59, 69, 70, 72, 73, 92, 95, 97, 98, 99, 100, 101, 103, 104, 107, 109, 112, 113, 114, 120, 121, 122, 123, 124, 125, 126, 127
- Einstein relation** The relationship between the Langevin friction coefficient and the Fickian diffusion coefficient, as discovered by Einstein. 8, 47
- electronic structure** The solution to the time-independent Schrödinger Equation for the electrons of an atom, molecule, ion, crystal, etc. 15, 88
- essential boundary condition** A boundary condition imposed on the FEM solution through the selection or shifting of interpolating functions. 21
- FEniCS** A finite element software package useable from python (see <https://fenicsproject.org/>). 2, 29, 39, 52
- flux** A vector describing the movement of a given quantity at every point in the problem domain. 6
- force field** A group of relations defining forces applied to atoms due to covalent bonds and other short-range interactions in molecular simulations. 18, 46, 88
- free volume fraction** Synonym for porosity. 10
- gmsh** A software package for creating finite element meshes (see <http://gmsh.info/>). 52, 72
- gromacs** A Molecular Dynamics software package (see <http://www.gromacs.org/>). 2, 50, 51
- hierarchical multi-scale model** A multi-scale model where information is transferred from smaller scales up to larger scales only. 3
- homogenization** Multi-scale technique based on asymptotic expansion. 3, 21, 88
- integrated flux** The net flux across a boundary surface (internal or external) in a problem. 6, 39, 40, 123, 124
- isotropy** A condition in which behavior is the same in all directions. 4

Langevin equation A stochastic differential equation of motion for a particle undergoing Brownian motion. 8

material properties Coefficients of a mathematical model that quantify the description or behavior of a material. 1

MDAnalysis A software package for processing Molecular Dynamics simulation data, useable from `python` (see <https://www.mdanalysis.org/>). 51

multiphysics The combination of mathematical models from different fields of study, and the interactions between such models. 3

multi-scale A model or problem involve more than one relevant scale of length, time, energy, etc. 3

natural boundary condition A boundary condition that must be included in the weak form in the FEM. 21

Neumann boundary condition A PDE boundary condition specifying the normal component of the gradient of the solution at a boundary location. 21, 40, 80, 92

numerical method A means of solving a numerical model. 14

numerical model A mathematical model using numerical data rather than only analytical expressions. 14, 87

NumPy An array library for the `python` programming language (see <https://numpy.org/>). 51, 52

order The power to which the reactant concentration is raised in the rate law for a reaction. 90

orthotropy A conceptually simple anisotropic condition in which the principal directions are all mutually orthogonal. 11

particle In this work, an atom, ion, or molecule undergoing diffusion or in MD or MC simulations. 6, 18, 87

point defect Where an atom or small group of atoms within a unit cell is displaced, replaced, or inserted. 23

porosity Ratio of the volume of voids to the total volume, ϕ . 10, 27, 30, 35, 59, 60, 86

porous media A solid interlaced with pore spaces. 9

PyMOL A software package for visualizing the structure of molecules and crystals (see <https://pymol.org/2/>). 45

python An interpreted computer programming language popular in the field of scientific programming (see <https://www.python.org/>). 2, 52, 86, 87

quantum chemistry The field of chemistry concerned with the electronic structure problem. 15

random checkerboard A two-dimensional stochastic homogenization problem with square unit cells taking on one of two isotropic diffusion coefficients at random. 25

reaction coordinate An independent variable for a potential energy surface. 46, 51

signal transduction The processes by which biochemical information is transmitted. 26

sign problem The difficulties involved in QMC due to the fermion antisymmetry requirement. 17

steady-state A condition where concentration is constant with respect to time, though it may still vary spatially. 7, 93

stochastic homogenization An extension of the homogenization technique to allow random variations of the otherwise periodic structure. 23

Stokes's Law A formula for the Langevin friction coefficient of a sphere moving through a viscous fluid. 8

supercell An REV consisting of multiple unit cells, rather than just one. 23, 24

test function An arbitrary function used in variational calculus. 20, 83

thermodynamic current One of the quantities related by a constitutive law (linear combinations of state variables defining the entropy [38]) . 4

thermodynamic force One of the quantities related by a constitutive law (time derivatives of state variables defining the entropy [38]) . 4

thermostat In MD simulations, a procedure for varying the total energy of the system to maintain a constant temperature. 19

trajectory The record of atom and ion positions over time in MD simulations. 18

transferability The idea that force parameters for a given bond are the same for all molecules containing that bond, a fundamental requirement for the validity of force fields in MD simulations. 18

variational form See weak form. 19

weak form A PDE converted to an integral problem by variational calculus. 19, 20, 22, 52, 88, 91, 95, 97, 116

wham A software package for conducting Weighted Histogram Analysis Method (WHAM) calculations (see http://membrane.urmc.rochester.edu/?page_id=126). 51, 64

Appendix D Mathematical Derivations

D.1 Reaction-Diffusion Systems

Consider a system in which species concentrations change not only due to diffusion, but also due to chemical reactions. The chemical reactions add new terms to the equation for $\partial_t c$.

For $N_{\text{reactions}}$ chemical reactions indexed by R , we write each reaction in the form



where r_{RS} and p_{RS} are the stoichiometric coefficients of the reactants and products, respectively, and X_S represents species S .

Note that reversible reactions must be considered as two separate reactions: the forward reaction and reverse reaction.

The rate of each reaction is described by its rate law. Rate laws are defined here by both a rate constant, k_R , and a rate function, f_R , which is a function of the concentration of all reactant species for the reaction. To provide a consistent set of arguments to these functions, we consider the rate functions to potentially depend instead on all species concentrations, writing them as $f_R = f_R(c_1, c_2, \dots)$. Typical rate laws include products of the reactant concentrations, with each concentration raised to a power known as the *order* of the reaction for the given species. Because of its dependence on the concentrations, f_R will vary spatially.

Using this notation, the change in the concentration of each species due to the presence of the chemical reactions alone is written as

$$\partial_t c_S = \sum_{R=1}^{N_{\text{reactions}}} (p_{RS} - r_{RS}) k_R f_R(c_1, c_2, \dots) \quad (\text{D.2})$$

Defining a net stoichiometric coefficient $n_{RS} = p_{RS} - r_{RS}$, which will be positive for reactions producing a species and negative for reactions consuming it, this becomes

$$\partial_t c_S = \sum_{R=1}^{N_{\text{reactions}}} n_{RS} k_R f_R(c_1, c_2, \dots) \quad (\text{D.3})$$

For systems where both reaction and diffusion take place, the two processes are usually assumed to be uncoupled: the change in concentration is simply the sum of the change due to diffusion and the change due to reaction. That is,

$$\partial_t c_S = -\partial_i j_{Si} + \sum_{R=1}^{N_{\text{reactions}}} n_{RS} k_R f_R(c_1, c_2, \dots) \quad (\text{D.4})$$

D.2 Weak Forms for Unhomogenized Diffusion Equations

Chapter 1 introduced PDEs describing the diffusion of a chemical species through a solvent. In D.1, this was extended to include production and consumption of new molecules or ions of a given species through chemical reactions. Here, the general weak form for these cases is derived. Both reaction and diffusion are included, and the diffusion coefficient is permitted to be anisotropic and spatially variant.

First, we express the particle flux in a general form:

$$j_{Si} = -D_{Sij}g_{Sj} \quad (\text{D.5})$$

where g_{Sj} is selected from the diffusion equation as follows:

$$\begin{aligned} \text{for Fick's Law:} & \quad g_{Sj} = \partial_j c_S \\ \text{for the Smoluchowski equation:} & \quad g_{Sj} = \partial_j c_S + \beta c_S \partial_j \Psi \\ \text{for the Smoluchowski exponential form:} & \quad g_{Sj} = e^{-\beta \Psi} \partial_j (e^{\beta \Psi} c_S) \end{aligned} \quad (\text{D.6})$$

Substituting this definition of the flux into Equation D.4 for the time-derivative of the concentration, we obtain the governing PDE:

$$\partial_t c_S = \partial_i D_{Sij} g_{Sj} + \sum_{R=1}^{N_{\text{reactions}}} n_{RS} k_R f_R \quad (\text{D.7})$$

There is one such PDE for each species, S , forming a set of N_{species} equations for the N_{species} unknowns, c_S . Note that whether this equation is linear or nonlinear depends on the linearity of g_{Sj} and f_R . For example, a typical reaction rate law, where the concentrations of the reactants are raised to various powers and multiplied together, would result in a nonlinear PDE.

The weak form of the equation is obtained by multiplying by a species-specific test function, v_S .

$$\int_{\Omega} d\Omega \partial_t c_S v_S = \int_{\Omega} d\Omega \partial_i (D_{Sij} g_{Sj}) v_S + \sum_{R=1}^{N_{\text{reactions}}} n_{RS} k_R \int_{\Omega} d\Omega f_R v_S \quad (\text{D.8})$$

We seek to perform an integration by parts for the first term on the right hand side. Applying the product rule,

$$\partial_i (D_{Sij} g_{Sj} v_S) = \partial_i (D_{Sij} g_{Sj}) v_S + D_{Sij} g_{Sj} \partial_i v_S \quad (\text{D.9})$$

Rearranging:

$$\partial_i (D_{Sij} g_{Sj}) v_S = \partial_i (D_{Sij} g_{Sj} v_S) - D_{Sij} g_{Sj} \partial_i v_S \quad (\text{D.10})$$

Integrating over the problem domain:

$$\int_{\Omega} d\Omega \partial_i (D_{Sij} g_{Sj}) v_S = \int_{\Omega} d\Omega \partial_i (D_{Sij} g_{Sj} v_S) - \int_{\Omega} d\Omega D_{Sij} g_{Sj} \partial_i v_S \quad (\text{D.11})$$

Applying the divergence theorem to the first term on the right hand side:

$$\int_{\Omega} d\Omega \partial_i (D_{Sij} g_{Sj}) v_S = \sum_{\Gamma} \int_{\Gamma} d\Gamma n_{\Gamma i} D_{Sij} g_{Sj} v_S - \int_{\Omega} d\Omega D_{Sij} g_{Sj} \partial_i v_S \quad (\text{D.12})$$

where the sum is over all boundaries, Γ , of the problem domain, Ω .

If the boundary conditions consist only of Dirichlet and Neumann boundary conditions, then the boundary condition term may be expressed as

$$\sum_{\Gamma} \int_{\Gamma} d\Gamma n_{\Gamma i} D_{Sij} g_{Sj} v_S = \sum_{\Gamma_D} \int_{\Gamma_D} d\Gamma n_{\Gamma i} D_{Sij} g_{Sj} v_S + \sum_{\Gamma_N} \int_{\Gamma_N} d\Gamma n_{\Gamma i} D_{Sij} g_{Sj} v_S \quad (\text{D.13})$$

For the Dirichlet boundary surfaces, where the concentration, c_S , is known, the corresponding test function, v_S , must be zero. Consequently, the Dirichlet boundary surface terms drop out of the equation. The boundary condition sum is therefore only over the Neumann boundary surfaces:

$$\int_{\Omega} d\Omega \partial_i (D_{Sij} g_{Sj}) v_S = \sum_{\Gamma_N} \int_{\Gamma_N} d\Gamma n_{\Gamma i} D_{Sij} g_{Sj} v_S - \int_{\Omega} d\Omega D_{Sij} g_{Sj} \partial_i v_S \quad (\text{D.14})$$

The integration by parts of the term in Equation D.8 is now complete. Substituting this result into Equation D.8, the weak form of the general anisotropic reaction-diffusion equation is:

$$\boxed{\begin{aligned} & \sum_{\Gamma_N} \int_{\Gamma_N} d\Gamma n_{\Gamma i} D_{Sij} g_{Sj} v_S \\ & - \int_{\Omega} d\Omega D_{Sij} g_{Sj} \partial_i v_S \\ & + \sum_{R=1}^{N_{\text{reactions}}} n_{RS} k_R \int_{\Omega} d\Omega f_{RV} v_S = \int_{\Omega} d\Omega \partial_i c_S v_S \end{aligned}} \quad (\text{D.15})$$

Weak forms suitable for use in FEM applications can be derived from Equation D.15 by substitution of the appropriate expression for g_{Sj} from Equation D.6. Special cases such as no reactions, isotropic diffusion, or a spatially invariant diffusion coefficient can also be derived from Equation D.15.

D.3 Homogenization of Fickian Diffusion

Here, the homogenized corrector problem for steady-state Fickian diffusion, and the REV integral to obtain the effective diffusion coefficient. The formulas derived here allow for the local diffusion coefficient, D , to vary in space and be anisotropic. The general formulas for similar equations are provided in Bensoussan et al. [12]. This

section follows the same procedure, and specializes the general formulas to the problem Fickian diffusion. Note that Bensoussan et al. [12] uses different notation than has been used herein. The equations in this section must necessarily make use of both forms of notation, as the purpose is to equate the variables and operators appearing in Bensoussan et al. [12] to those used herein. To reduce confusion, expressions or equations coming directly from Bensoussan et al. [12] are enclosed in curly braces, such as $\{A^\epsilon\}$.

In the two-scale homogenization procedure, x represents the large-scale coordinate (such as distance measured in meters), and y represents the small-scale coordinate (such as distance measured in nanometers). Accordingly, the REV is denoted by Y . In this section, partial derivatives must explicitly indicate which coordinate scale they are taken with respect to, as well as the direction thereof.

The PDE to homogenize is Fick's law under steady-state conditions:

$$\frac{\partial}{\partial x_i} \left(D_{ij} \frac{\partial c}{\partial x_j} \right) = 0 \quad (\text{D.16})$$

The first step is to express Equation D.16 in the form of equation 1.1.5 of Bensoussan et al. [12]:

$$\{A^\epsilon u_\epsilon = f\} \quad (\text{D.17})$$

By comparison, this requires:

$$\{A^\epsilon\} = \frac{\partial}{\partial x_i} \left(D_{ij} \frac{\partial}{\partial x_j} \right) \quad (\text{D.18})$$

$$\{u_\epsilon\} = c \quad (\text{D.19})$$

$$\{f\} = 0 \quad (\text{D.20})$$

From equation 1.1.3 of of Bensoussan et al. [12], $\{A^\epsilon\}$ as

$$\left\{ A^\epsilon = -\frac{\partial}{\partial x_i} \left(a_{ij} \left(\frac{x}{\epsilon} \right) \frac{\partial}{\partial x_j} \right) + a_0 \left(\frac{x}{\epsilon} \right) \right\} \quad (\text{D.21})$$

Consequently,

$$\{a_{ij}\} = -D_{ij} \quad (\text{D.22})$$

$$\{a_0\} = 0 \quad (\text{D.23})$$

Equation 2.2.3 of of Bensoussan et al. [12] provides

$$\left\{ A_1 = -\frac{\partial}{\partial y_i} \left(a_{ij}(y) \frac{\partial}{\partial y_j} \right) \right\} \quad (\text{D.24})$$

$$\left\{ A_2 = -\frac{\partial}{\partial y_i} \left(a_{ij}(y) \frac{\partial}{\partial x_j} \right) - \frac{\partial}{\partial x_i} \left(a_{ij}(y) \frac{\partial}{\partial y_j} \right) \right\} \quad (\text{D.25})$$

$$\left\{ A_3 = -\frac{\partial}{\partial x_i} \left(a_{ij}(y) \frac{\partial}{\partial x_j} \right) + a_0 \right\} \quad (\text{D.26})$$

Which, in this case, yields

$$\{A_1\} = -\frac{\partial}{\partial y_i} \left(-D_{ij} \frac{\partial}{\partial y_j} \right) \quad (\text{D.27})$$

$$\{A_2\} = -\frac{\partial}{\partial y_i} \left(-D_{ij} \frac{\partial}{\partial x_j} \right) - \frac{\partial}{\partial x_i} \left(-D_{ij} \frac{\partial}{\partial y_j} \right) \quad (\text{D.28})$$

$$\{A_3\} = -\frac{\partial}{\partial x_i} \left(-D_{ij} \frac{\partial}{\partial x_j} \right) + 0 \quad (\text{D.29})$$

And so, from equation 2.2.17 of Bensoussan et al. [12], the equation to solve on the unit cell (Y) for vector χ is

$$\left\{ A_1 \chi^j = -\frac{\partial}{\partial y_i} a_{ij}(y) \right\} \quad (\text{D.30})$$

which becomes

$$-\frac{\partial}{\partial y_i} \left(-D_{ik} \frac{\partial}{\partial y_k} \right) \chi_j = -\frac{\partial}{\partial y_i} (-D_{ij}) \quad (\text{D.31})$$

$$\boxed{\frac{\partial}{\partial y_i} \left(D_{ik} \frac{\partial \chi_j}{\partial y_k} \right) = \frac{\partial}{\partial y_i} D_{ij}} \quad (\text{D.32})$$

Equation D.32 is the homogenized corrector problem for Fickian diffusion, with χ_j as the unknown corrector function. And from the homogenized result in equation 2.2.20 of Bensoussan et al. [12],

$$\left\{ -\frac{1}{|Y|} \left(\int_Y \left(a_{ij} - a_{ik} \frac{\partial \chi^j}{\partial y_k} \right) dy \right) \frac{\partial^2 u}{\partial x_i \partial x_j} + \frac{1}{|Y|} \left(\int_Y a_0(y) dy \right) u = f \right\} \quad (\text{D.33})$$

This becomes

$$D_{ij}^{\text{eff}} \frac{\partial^2 c}{\partial x_i \partial x_j} + 0 = 0 \quad (\text{D.34})$$

with

$$D_{ij}^{\text{eff}} = -\frac{1}{|Y|} \int_Y dY \left(-D_{ij} + D_{ik} \frac{\partial \chi_j}{\partial y_k} \right) \quad (\text{D.35})$$

$$\boxed{D_{ij}^{\text{eff}} = \frac{1}{|Y|} \int_Y dY \left(D_{ij} - D_{ik} \frac{\partial \chi_j}{\partial y_k} \right)} \quad (\text{D.36})$$

Returning to the notation of Chapter 2, and with the REV as the problem domain, Ω , Equations D.32 and D.36 become Equations D.37 and D.38, respectively.

$$\boxed{\partial_i (D_{ik} \partial_k \chi_j) = \partial_i D_{ij}} \quad (\text{D.37})$$

$$\boxed{D_{ij}^{\text{eff}} = \frac{1}{|\Omega|} \int_{\Omega} d\Omega (D_{ij} - D_{ik} \partial_k \chi_j)} \quad (\text{D.38})$$

Note that some references, including Anantharaman et al. [3], Anantharaman and Le Bris [4], and Costeauc [30], use the opposite sign convention to define the corrector function. That is, the corrector function may be defined as $w_j = -\chi_j$. Provided that the appropriate signs are changed in both Equations D.37 and D.38, the resulting expressions are equivalent:

$$\boxed{-\partial_i (D_{ik} \partial_k w_j) = \partial_i D_{ij}} \quad (\text{D.39})$$

$$\boxed{D_{ij}^{\text{eff}} = \frac{1}{|\Omega|} \int_{\Omega} d\Omega (D_{ij} + D_{ik} \partial_k w_j)} \quad (\text{D.40})$$

D.4 Weak Form for Homogenized Fickian Diffusion

The objective of this section is to derive the weak form for the corrector problem of Equation 2.12, so that the effective diffusion coefficient can be obtained from FEM simulations described in Section 2.4.

Starting from Equation 2.12:

$$\partial_i (D_{ik} \partial_k \chi_j) = \partial_i D_{ij} \quad (\text{D.41})$$

First, to obtain a scalar-valued functional, take the scalar product of a vector-valued test function, v_j , with the terms of this equation, and integrate the result over the problem domain.

$$\int_{\Omega} d\Omega v_j \partial_i (D_{ik} \partial_k \chi_j) = \int_{\Omega} d\Omega v_j (\partial_i D_{ij}) \quad (\text{D.42})$$

Numerical solvers often seek the roots of a given function, so it is convenient to express this in the form of Equation D.43.

$$\int_{\Omega} d\Omega v_j \partial_i (D_{ik} \partial_k \chi_j) - \int_{\Omega} d\Omega v_j (\partial_i D_{ij}) = 0 \quad (\text{D.43})$$

While this weak form could be used, it has two undesirable features:

- A second derivative of χ_j is involved.
- Derivatives of the local diffusion coefficient, D , are involved, which is problematic when there are discontinuities in D , such as in the example of Section D.5.

Accordingly, it is advantageous to apply integration by parts, to shift the gradient operators to the test function.

For the first term in Equation D.43, note the following product rule:

$$\partial_i (v_j D_{ik} \partial_k \chi_j) = (\partial_i v_j) (D_{ik} \partial_k \chi_j) + v_j \partial_i (D_{ik} \partial_k \chi_j) \quad (\text{D.44})$$

Rearranging,

$$v_j \partial_i (D_{ik} \partial_k \chi_j) = \partial_i (v_j D_{ik} \partial_k \chi_j) - (\partial_i v_j) (D_{ik} \partial_k \chi_j) \quad (\text{D.45})$$

Integrating over the domain,

$$\int_{\Omega} d\Omega v_j \partial_i (D_{ik} \partial_k \chi_j) = \int_{\Omega} d\Omega \partial_i (v_j D_{ik} \partial_k \chi_j) - \int_{\Omega} d\Omega (\partial_i v_j) (D_{ik} \partial_k \chi_j) \quad (\text{D.46})$$

Applying the Divergence Theorem (Gauss's Theorem) [6, 93] to the first term on the right hand side, and rearranging the factors in the second term,

$$\int_{\Omega} d\Omega v_j \partial_i (D_{ik} \partial_k \chi_j) = \sum_{\Gamma_N} \int_{\Gamma_N} d\Gamma n_{\Gamma i} v_j D_{ik} \partial_k \chi_j - \int_{\Omega} d\Omega D_{ik} (\partial_i v_j) (\partial_k \chi_j) \quad (\text{D.47})$$

For the second term in Equation D.43, note the following product rule:

$$\partial_i (D_{ij} v_j) = (\partial_i D_{ij}) v_j + D_{ij} (\partial_i v_j) \quad (\text{D.48})$$

Rearranging,

$$(\partial_i D_{ij}) v_j = \partial_i (D_{ij} v_j) - D_{ij} (\partial_i v_j) \quad (\text{D.49})$$

Integrating over the domain,

$$\int_{\Omega} d\Omega (\partial_i D_{ij}) v_j = \int_{\Omega} d\Omega \partial_i (D_{ij} v_j) - \int_{\Omega} d\Omega D_{ij} (\partial_i v_j) \quad (\text{D.50})$$

Applying the Divergence Theorem to the first term on the right hand side,

$$\int_{\Omega} d\Omega (\partial_i D_{ij}) v_j = \sum_{\Gamma_N} \int_{\Gamma_N} d\Gamma n_{\Gamma i} D_{ij} v_j - \int_{\Omega} d\Omega D_{ij} (\partial_i v_j) \quad (\text{D.51})$$

This completes the integrations by parts. Substituting the results of Equations D.47 and D.51 into Equation D.43, the resulting weak form is:

$$\boxed{\begin{aligned} & \sum_{\Gamma_N} \int_{\Gamma_N} d\Gamma n_{\Gamma i} v_j D_{ik} \partial_k \chi_j - \int_{\Omega} d\Omega D_{ik} (\partial_i v_j) (\partial_k \chi_j) \\ & - \sum_{\Gamma_N} \int_{\Gamma_N} d\Gamma n_{\Gamma i} D_{ij} v_j + \int_{\Omega} d\Omega D_{ij} (\partial_i v_j) \end{aligned}} = 0 \quad (\text{D.52})$$

Equation D.52 is a weak form of the corrector problem suitable for implementation in FEM software.

One special case of D.52 is when the local diffusion coefficient is isotropic: $D_{ij} = D\delta_{ij}$. In this case, the weak form simplifies to Equation D.53.

$$\boxed{\begin{aligned} \sum_{\Gamma_N} \int_{\Gamma_N} d\Gamma D n_{\Gamma_i} v_j \partial_i \chi_j - \int_{\Omega} d\Omega D (\partial_i v_j) (\partial_i \chi_j) \\ - \sum_{\Gamma_N} \int_{\Gamma_N} d\Gamma D n_{\Gamma_i} v_i + \int_{\Omega} d\Omega D (\partial_i v_i) \end{aligned}} = 0 \quad (\text{D.53})$$

Note that an overall negative sign can be applied to this equation, and the result would still be a valid solution. This can be a source of confusion when comparing weak forms between different codes, and a source of errors when implementing extensions to a given code.

This sign convention issue is further complicated by the possibility of an alternate sign convention for the corrector function, $w_j = -\chi_j$, as noted in Section D.3. For convenience of comparisons, the weak form from Equation D.53, under both of these changes of sign, becomes

$$\boxed{\begin{aligned} \sum_{\Gamma_N} \int_{\Gamma_N} d\Gamma D n_{\Gamma_i} v_j \partial_i w_j - \int_{\Omega} d\Omega D (\partial_i v_j) (\partial_i w_j) \\ + \sum_{\Gamma_N} \int_{\Gamma_N} d\Gamma D n_{\Gamma_i} v_i - \int_{\Omega} d\Omega D (\partial_i v_i) \end{aligned}} = 0 \quad (\text{D.54})$$

D.5 Effective Diffusion Coefficient of Bi-Layered Media

As an example to demonstrate and verify the homogenization approach, consider diffusion of a single chemical species through a medium consisting of alternating layers of two isotropic materials. For simplicity, the problem is defined in only two dimensions. The unit cell for such a medium is depicted in Figure D.1. The objective is to obtain the effective diffusion coefficient for this medium. Naturally, this problem could be generalized to multiple layers, but the essential features of the problem are illustrated with only two layers, without the additional mathematical complications.

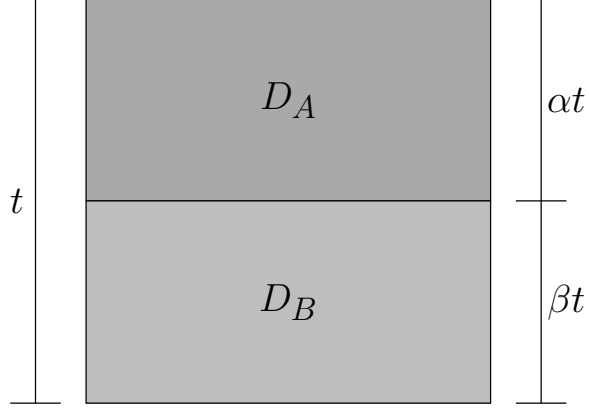


Figure D.1: Unit cell for a medium consisting of two isotropic layers with diffusion coefficients D_A and D_B . The total thickness of the unit cell is t , with layer thickness values αt and βt .

Because of the layered structure, the medium may behave anisotropically. If the coordinate system axes are aligned with the layer axes (that is, the axes are parallel and perpendicular to the layers), the off-diagonal terms of the effective diffusion coefficient, D_{ij}^{eff} , should be zero. Consequently, Fick's first law will have the form shown in Equation D.55.

$$\begin{bmatrix} j_1 \\ j_2 \end{bmatrix} = - \begin{bmatrix} D_{11}^{\text{eff}} & 0 \\ 0 & D_{22}^{\text{eff}} \end{bmatrix} \begin{bmatrix} \partial_1 c \\ \partial_2 c \end{bmatrix} \quad (\text{D.55})$$

Diffusion in the directions of the coordinate axes are thus decoupled, as shown in Equation D.56.

$$\begin{aligned} j_1 &= -D_{11}^{\text{eff}} \partial_1 c \\ j_2 &= -D_{22}^{\text{eff}} \partial_2 c \end{aligned} \quad (\text{D.56})$$

D_{11}^{eff} and D_{22}^{eff} should depend only on the diffusion coefficients of layers, D_A and D_B , and the relative thickness of the two layers. For a unit cell of thickness t , the thickness values of the layers are αt and βt for materials A and B, respectively. Thus, $\alpha + \beta = 1$.

In this simple problem, the effective diffusion coefficient can be found without homogenization theory. The approach used here is similar to the approach used for the hydraulic conductivity of layered porous media in Bear [11].

First, solve for D_{11}^{eff} by considering diffusion in the direction parallel to the layers. Because of the decoupling of the two directions, the concentration varies only in the parallel direction as well. Thus, both layers are subjected to the same concentration gradient, $\partial_1 c$ but will have different fluxes, j_{A1} and j_{B1} , as shown in Equation D.57.

$$\begin{aligned} j_{A1} &= -D_A \partial_1 c \\ j_{B1} &= -D_B \partial_1 c \end{aligned} \quad (\text{D.57})$$

The total flux through the unit cell in the parallel direction, J_1 , can be obtained by integrating the vector flux field over any line perpendicular to the layers.

$$J_1 = \int_{\Gamma} d\Gamma j_1 \quad (\text{D.58})$$

Because the flux is constant within each layer, this integral simplifies to

$$J_1 = \alpha t j_{A1} + \beta t j_{B1} \quad (\text{D.59})$$

In terms of the average flux, $\frac{J_1}{t}$, and substituting the expressions from D.57, this becomes

$$\frac{J_1}{t} = -\alpha D_A \partial_1 c - \beta D_B \partial_1 c \quad (\text{D.60})$$

Bringing out the common factors, this is

$$\frac{J_1}{t} = -(\alpha D_A + \beta D_B) \partial_1 c \quad (\text{D.61})$$

The desired effective diffusion coefficient, D_{11}^{eff} , must satisfy

$$\frac{J_1}{t} = -D_{11}^{\text{eff}} \partial_1 c \quad (\text{D.62})$$

Comparing Equations D.61 and D.62, the effective diffusion coefficient is

$$\boxed{D_{11}^{\text{eff}} = \alpha D_A + \beta D_B} \quad (\text{D.63})$$

The effective diffusion coefficient parallel to the layers is therefore simply the weighted average of the isotropic coefficients of the layers.

Next, solve for D_{22}^{eff} by considering diffusion in the direction perpendicular to the layers. In this case, the flux through each layer must be identical:

$$j_{A2} = j_{B2} = j_2 \quad (\text{D.64})$$

Consequently, each layer must have a different value of the concentration gradient. That is, the concentration will vary linearly within each layer, but the slope of this linear variation will be different for each material.

From Fick's Law within each material, then,

$$j_2 = -D_A (\partial_1 c)_A = -D_B (\partial_1 c)_B \quad (\text{D.65})$$

Each concentration gradient is the total change in concentration within the layer, divided by the layer thickness:

$$\begin{aligned} (\partial_1 c)_A &= \frac{\Delta_A c}{\alpha t} \\ (\partial_1 c)_B &= \frac{\Delta_B c}{\beta t} \end{aligned} \quad (\text{D.66})$$

And so Equation D.65 becomes

$$j_2 = -D_A \frac{\Delta_{AC}}{\alpha t} = -D_B \frac{\Delta_{BC}}{\beta t} \quad (\text{D.67})$$

The effective diffusion coefficient is defined by

$$j_2 = -D_{22}^{\text{eff}} \frac{\Delta c}{t} \quad (\text{D.68})$$

where the total change in concentration, Δc , is the sum of the change in each layer:

$$\Delta c = \Delta_{AC} + \Delta_{BC} \quad (\text{D.69})$$

and dividing this by the total thickness of the unit cell, t , results in:

$$\frac{\Delta c}{t} = \frac{\Delta_{AC}}{t} + \frac{\Delta_{BC}}{t} \quad (\text{D.70})$$

Solving Equations D.67 and D.68 for the terms in Equation D.70,

$$\frac{\Delta_{AC}}{t} = -\frac{j_2 \alpha}{D_A} \quad (\text{D.71})$$

$$\frac{\Delta_{BC}}{t} = -\frac{j_2 \beta}{D_B} \quad (\text{D.72})$$

$$\frac{\Delta c}{t} = -\frac{j_2}{D_{22}^{\text{eff}}} \quad (\text{D.73})$$

Substituting these expressions into Equation D.70:

$$-\frac{j_2}{D_{22}^{\text{eff}}} = -\frac{j_2 \alpha}{D_A} - \frac{j_2 \beta}{D_B} \quad (\text{D.74})$$

which simplifies to

$$\frac{1}{D_{22}^{\text{eff}}} = \frac{\alpha}{D_A} + \frac{\beta}{D_B} \quad (\text{D.75})$$

Thus, the effective diffusion coefficient perpendicular to the layers is the inverse of the sum of the inverses of the diffusion coefficients. This expression can be rewritten as

$$\boxed{D_{22}^{\text{eff}} = \frac{D_A D_B}{\beta D_A + \alpha D_B}} \quad (\text{D.76})$$

In analogy to Ohm's Law, when expressed in terms of conductance rather than resistance, the effective diffusion coefficient adds linearly for layers in parallel, and adds as the inverse of inverses for layers in series.

The complete effective diffusion coefficient matrix for the two layers is

$$D_{ij}^{\text{eff}} = \begin{bmatrix} \alpha D_A + \beta D_B & 0 \\ 0 & \frac{D_A D_B}{\beta D_A + \alpha D_B} \end{bmatrix} \quad (\text{D.77})$$

This same problem can also be solved using periodic homogenization, as described in Section 2.5. The corrector problem is given in Equation 2.12. Within each layer, the material is isotropic:

$$D_{ij}^{\text{layer}} = D^{\text{layer}} \delta_{ij} \quad (\text{D.78})$$

Under this condition, the corrector problem becomes

$$\partial_i (D^{\text{layer}} \delta_{ij} \partial_k \chi_j) = \partial_i D^{\text{layer}} \delta_{ij} \quad (\text{D.79})$$

Applying the Kronecker deltas results in

$$\partial_i (D^{\text{layer}} \partial_i \chi_j) = \partial_j D^{\text{layer}} \quad (\text{D.80})$$

The corrector problem in each direction is then

$$\partial_i (D^{\text{layer}} \partial_i \chi_1) = \partial_1 D^{\text{layer}} = 0 \quad (\text{D.81})$$

$$\partial_i (D^{\text{layer}} \partial_i \chi_2) = \partial_2 D^{\text{layer}} \quad (\text{D.82})$$

where $\partial_1 D^{\text{layer}} = 0$ because each layer is continuous in the parallel direction.

Expanding the implied sums:

$$\partial_1 (D^{\text{layer}} \partial_1 \chi_1) + \partial_2 (D^{\text{layer}} \partial_2 \chi_1) = 0 \quad (\text{D.83})$$

$$\partial_1 (D^{\text{layer}} \partial_1 \chi_2) + \partial_2 (D^{\text{layer}} \partial_2 \chi_2) = \partial_2 D^{\text{layer}} \quad (\text{D.84})$$

Applying the product rule, with $\partial_1 D^{\text{layer}} = 0$:

$$D^{\text{layer}} \partial_1 \partial_1 \chi_1 + (\partial_2 D^{\text{layer}}) \partial_2 \chi_1 + D^{\text{layer}} \partial_2 \partial_2 \chi_1 = 0 \quad (\text{D.85})$$

$$D^{\text{layer}} \partial_1 \partial_1 \chi_2 + (\partial_2 D^{\text{layer}}) \partial_2 \chi_2 + D^{\text{layer}} \partial_2 \partial_2 \chi_2 = \partial_2 D^{\text{layer}} \quad (\text{D.86})$$

Within a given layer, D^{layer} is constant. However, at the interfaces between layers, the derivative $\partial_2 D^{\text{layer}}$ is not zero. In fact, because D^{layer} changes abruptly at the interfaces, $\partial_2 D^{\text{layer}}$ does not exist at these locations. The corrector problem can therefore be expressed as a set of PDEs within the layers, and a set of boundary conditions applying at the interface between them. In fact, the PDE within a layer is the same for both layers and both components:

$$D^{\text{layer}} \partial_1 \partial_1 \chi_j + D^{\text{layer}} \partial_2 \partial_2 \chi_j = 0 \quad (\text{D.87})$$

Removing the common factor of D^{layer} , this equation indicates that each component of the corrector satisfies a Laplace equation within each material.

$$\partial_1 \partial_1 \chi_j + \partial_2 \partial_2 \chi_j = 0 \quad (\text{D.88})$$

Because this Laplace equation is satisfied within each material, the equations for the interface conditions may be simplified to

$$(\partial_2 D^{\text{layer}}) \partial_2 \chi_1 = 0 \quad (\text{D.89})$$

$$(\partial_2 D^{\text{layer}}) \partial_2 \chi_2 = \partial_2 D^{\text{layer}} \quad (\text{D.90})$$

Because of the discontinuity, the partial derivatives ∂_2 , which do not exist at the interfaces, must be replaced with differences across the interface:

$$\partial_2 D^{\text{layer}} \rightarrow D^+ - D^- \quad (\text{D.91})$$

$$\partial_2 \chi_j \rightarrow \chi_j^+ - \chi_j^- \quad (\text{D.92})$$

$$\partial_2 \partial_2 \chi_j \rightarrow (\partial_2 \chi_j)^+ - (\partial_2 \chi_j)^- \quad (\text{D.93})$$

$$(\partial_2 D^{\text{layer}}) \partial_2 \chi_j \rightarrow D^+ (\partial_2 \chi_j)^+ - D^- (\partial_2 \chi_j)^- \quad (\text{D.94})$$

where the superscripts of plus and minus denote the quantities above and below the interface, respectively.

The interface condition equations are therefore

$$D^+ (\partial_2 \chi_1)^+ - D^- (\partial_2 \chi_1)^- = 0 \quad (\text{D.95})$$

$$D^+ (\partial_2 \chi_2)^+ - D^- (\partial_2 \chi_2)^- = D^+ - D^- \quad (\text{D.96})$$

Note that these conditions allow χ_j itself to be continuous across the interfaces; only $\partial_2 \chi_j$ need have a discontinuity.

Furthermore, the equations for χ_1 can be satisfied by a constant function, as derivatives of zero satisfy the Laplace equation in each layer and the interface condition as well. Because the corrector function can be shifted by an arbitrary constant, zero is an acceptable value for the constant function itself.

$$\boxed{\chi_1 = 0} \quad (\text{D.97})$$

Thus, only the solution of χ_2 remains.

There are two interfaces:

- at $x_2 = \beta t$, where material A is above the interface, and B is below ($+ \rightarrow A$, $- \rightarrow B$), and
- at the unit cell boundary $x_2 = 0$, which is periodically identical to $x_2 = t$, where material B is above the interface, and A is below ($+ \rightarrow B$, $- \rightarrow A$).

Define the solution χ_2 within layers A and B as χ_{A2} and χ_{B2} , respectively. These functions must satisfy the Laplace equations, the interface condition equations at each interface, and the periodicity requirements.

$$\text{within A:} \quad \partial_1 \partial_1 \chi_{A2} + \partial_2 \partial_2 \chi_{A2} = 0 \quad (\text{D.98})$$

$$\text{within B:} \quad \partial_1 \partial_1 \chi_{B2} + \partial_2 \partial_2 \chi_{B2} = 0 \quad (\text{D.99})$$

$$\text{at } x_2 = \beta t: \quad D_A (\partial_2 \chi_{A2})|_{x_2=\beta t} - D_B (\partial_2 \chi_{B2})|_{x_2=\beta t} = D_A - D_B \quad (\text{D.100})$$

$$\text{at } x_2 = 0 \text{ and } x_2 = t: \quad D_B (\partial_2 \chi_{B2})|_{x_2=0} - D_A (\partial_2 \chi_{A2})|_{x_2=t} = D_B - D_A \quad (\text{D.101})$$

$$\text{at } x_2 = \beta t: \quad \chi_{A2}|_{x_2=\beta t} = \chi_{B2}|_{x_2=\beta t} \quad (\text{D.102})$$

$$\text{at } x_2 = \beta t: \quad \chi_{A2}|_{x_2=t} = \chi_{B2}|_{x_2=0} \quad (\text{D.103})$$

These equations define χ_2 up to a shift by an arbitrary constant. The solution is

$$\chi_{A2} = -\beta M (t - x_2) \quad (\text{D.104})$$

$$\chi_{B2} = -\alpha M x_2 \quad (\text{D.105})$$

$$M = \frac{D_A - D_B}{\beta D_A + \alpha D_B} \quad (\text{D.106})$$

The relevant partial derivatives are

$$\partial_2 \chi_{A2} = \beta M \quad \partial_2 \chi_{B2} = -\alpha M \quad (\text{D.107})$$

$$\partial_2 \partial_2 \chi_{A2} = 0 \quad \partial_2 \partial_2 \chi_{B2} = 0 \quad (\text{D.108})$$

The solution is demonstrated by substitution into Equations D.98 through D.103:

$$\text{within A:} \quad 0 + 0 = 0 \quad (\text{D.109})$$

$$\text{within B:} \quad 0 + 0 = 0 \quad (\text{D.110})$$

$$\text{at } x_2 = \beta t: \quad D_A \beta M + D_B \alpha M = D_A - D_B \quad (\text{D.111})$$

$$\text{at } x_2 = 0 \text{ and } x_2 = t: \quad -D_B \alpha M + D_A \beta M = D_B - D_A \quad (\text{D.112})$$

$$\text{at } x_2 = \beta t: \quad -\alpha \beta M t = -\alpha \beta M t \quad (\text{D.113})$$

$$\text{at } x_2 = \beta t: \quad 0 = 0 \quad (\text{D.114})$$

Equations D.111 and D.112 are related by an overall negative sign. The simplification of these equations, starting with the substitution of M , is

$$\frac{\beta D_A (D_A - D_B) + \alpha D_B (D_A - D_B)}{\beta D_A + \alpha D_B} = D_A - D_B \quad (\text{D.115})$$

$$1 (D_A - D_B) = D_A - D_B \quad (\text{D.116})$$

Thus, the solution is confirmed.

Next, the solution for χ_j must be substituted into the REV integral of Equation 2.13, to obtain the effective diffusion coefficient matrix. Breaking the integral into the

sum of integrals over the material layers, applying the condition of isotropy within the materials ($D_{ij} = D^{\text{layer}}\delta_{ij}$), and noting that χ_j varies only in the x_2 direction, the expression for the effective diffusion coefficient becomes:

$$D_{ij}^{\text{eff}} = \frac{1}{t} \left(D_A \int_{\beta t}^t dx_2 (\delta_{ij} - \partial_i \chi_{Aj}) + D_B \int_0^{\beta t} dx_2 (\delta_{ij} - \partial_i \chi_{Bj}) \right) \quad (\text{D.117})$$

Applying the indices to evaluate all four terms of the effective diffusion coefficient:

$$D_{11}^{\text{eff}} = \frac{1}{t} \left(D_A \int_{\beta t}^t dx_2 (\delta_{11} - \partial_1 \chi_{A1}) + D_B \int_0^{\beta t} dx_2 (\delta_{11} - \partial_1 \chi_{B1}) \right) \quad (\text{D.118})$$

$$D_{12}^{\text{eff}} = \frac{1}{t} \left(D_A \int_{\beta t}^t dx_2 (\delta_{12} - \partial_1 \chi_{A2}) + D_B \int_0^{\beta t} dx_2 (\delta_{12} - \partial_1 \chi_{B2}) \right) \quad (\text{D.119})$$

$$D_{21}^{\text{eff}} = \frac{1}{t} \left(D_A \int_{\beta t}^t dx_2 (\delta_{21} - \partial_2 \chi_{A1}) + D_B \int_0^{\beta t} dx_2 (\delta_{21} - \partial_2 \chi_{B1}) \right) \quad (\text{D.120})$$

$$D_{22}^{\text{eff}} = \frac{1}{t} \left(D_A \int_{\beta t}^t dx_2 (\delta_{22} - \partial_2 \chi_{A2}) + D_B \int_0^{\beta t} dx_2 (\delta_{22} - \partial_2 \chi_{B2}) \right) \quad (\text{D.121})$$

Applying the Kronecker deltas and noting that $\chi_1 = 0$ and $\partial_1 \chi_2 = 0$:

$$D_{11}^{\text{eff}} = \frac{1}{t} \left(D_A \int_{\beta t}^t dx_2 (1 - 0) + D_B \int_0^{\beta t} dx_2 (1 - 0) \right) \quad (\text{D.122})$$

$$D_{12}^{\text{eff}} = \frac{1}{t} \left(D_A \int_{\beta t}^t dx_2 (0 - 0) + D_B \int_0^{\beta t} dx_2 (0 - 0) \right) \quad (\text{D.123})$$

$$D_{21}^{\text{eff}} = \frac{1}{t} \left(D_A \int_{\beta t}^t dx_2 (0 - 0) + D_B \int_0^{\beta t} dx_2 (0 - 0) \right) \quad (\text{D.124})$$

$$D_{22}^{\text{eff}} = \frac{1}{t} \left(D_A \int_{\beta t}^t dx_2 (1 - \partial_2 \chi_{A2}) + D_B \int_0^{\beta t} dx_2 (1 - \partial_2 \chi_{B2}) \right) \quad (\text{D.125})$$

Thus, the off-diagonal terms, D_{12}^{eff} and D_{21}^{eff} , are clearly zero. This matches the result of the analytical solution. Only the diagonal terms of the matrix remain.

Taking the integrals in Equation D.122:

$$D_{11}^{\text{eff}} = \frac{1}{t} \left(D_A \int_{\beta t}^t dx_2 + D_B \int_0^{\beta t} dx_2 \right) \quad (\text{D.126})$$

$$= \frac{1}{t} (D_A \alpha t + D_B \beta t) \quad (\text{D.127})$$

$$= \alpha D_A + \beta D_B \quad (\text{D.128})$$

which matches the analytical result from Equation D.63.

Substituting the derivatives of χ_2 into Equation D.125:

$$D_{22}^{\text{eff}} = \frac{1}{t} \left(D_A \int_{\beta t}^t dx_2 (1 - \beta M) + D_B \int_0^{\beta t} dx_2 (1 + \alpha M) \right) \quad (\text{D.129})$$

$$= \frac{1}{t} (D_A \alpha t (1 - \beta M) + D_B \beta t (1 + \alpha M)) \quad (\text{D.130})$$

$$= \alpha D_A (1 - \beta M) + \beta D_B (1 + \alpha M) \quad (\text{D.131})$$

Substituting the expression for M from Equation D.106:

$$D_{22}^{\text{eff}} = \alpha D_A \left(1 - \beta \frac{D_A - D_B}{\beta D_A + \alpha D_B} \right) + \beta D_B \left(1 + \alpha \frac{D_A - D_B}{\beta D_A + \alpha D_B} \right) \quad (\text{D.132})$$

$$= \alpha D_A \frac{\beta D_A + \alpha D_B - \beta (D_A - D_B)}{\beta D_A + \alpha D_B} + \beta D_B \frac{\beta D_A + \alpha D_B + \alpha (D_A - D_B)}{\beta D_A + \alpha D_B} \quad (\text{D.133})$$

$$D_{22}^{\text{eff}} = \alpha D_A \frac{\alpha D_B + \beta D_B}{\beta D_A + \alpha D_B} + \beta D_B \frac{\beta D_A + \alpha D_A}{\beta D_A + \alpha D_B} \quad (\text{D.134})$$

$$= \alpha D_A \frac{D_B}{\beta D_A + \alpha D_B} + \beta D_B \frac{D_A}{\beta D_A + \alpha D_B} \quad (\text{D.135})$$

$$= \frac{\alpha D_A D_B + \beta D_A D_B}{\beta D_A + \alpha D_B} \quad (\text{D.136})$$

$$= \frac{D_A D_B}{\beta D_A + \alpha D_B} \quad (\text{D.137})$$

which matches the analytical result from Equation D.76.

The homogenization prediction therefore matches the analytical result without homogenization:

$$D_{ij}^{\text{eff}} = \begin{bmatrix} \alpha D_A + \beta D_B & 0 \\ 0 & \frac{D_A D_B}{\beta D_A + \alpha D_B} \end{bmatrix} \quad (\text{D.138})$$

D.6 Effective Diffusion Coefficient in an Example with Spatially Varying D_{local}

This section presents an example problem of homogenized Fickian diffusion in a two-dimensional unit cell, where the local diffusion coefficient varies in space. Index notation will not be used in this section.

The unit cell geometry is illustrated in Figure D.2. The side lengths of the unit cell are denoted by the variables a and L , as shown. The boundary conditions are

$$\begin{aligned} c \left(x = -\frac{L}{2} \right) &= c_L \\ c \left(x = +\frac{L}{2} \right) &= c_R \end{aligned} \quad (\text{D.139})$$

These conditions impose an average concentration gradient of

$$\frac{\Delta c}{L} = \frac{c_R - c_L}{L} \quad (\text{D.140})$$

across the unit cell.

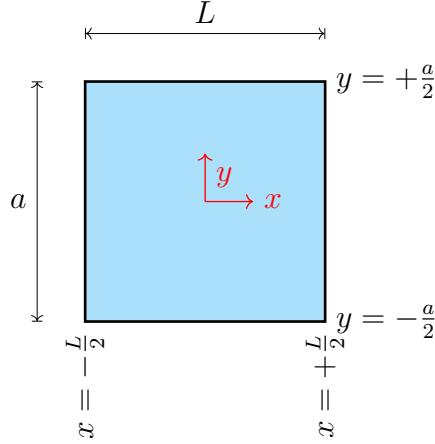


Figure D.2: Unit cell for the example Fickian diffusion problem.

First, consider a spatially varying diffusion coefficient of the form

$$D_{\text{local}}(x, y) = D_{\text{local}}(y) = D_0 (1 + \alpha^2 y^2) \quad (\text{D.141})$$

where D_0 is the diffusion coefficient along the line $y = 0$, and α is a constant with units of inverse length.

The steady-state Fickian diffusion equation for this situation is

$$\frac{\partial}{\partial x} \left(D_{\text{local}} \frac{\partial c}{\partial x} \right) + \frac{\partial}{\partial y} \left(D_{\text{local}} \frac{\partial c}{\partial y} \right) = 0 \quad (\text{D.142})$$

For the given form of D_{local} ,

$$\begin{aligned} \frac{\partial}{\partial x} (D_{\text{local}}) &= 0 \\ \frac{\partial}{\partial y} (D_{\text{local}}) &= D_0 2\alpha^2 y \end{aligned} \quad (\text{D.143})$$

Following expansion of the outer partial derivatives and removal of D_0 as a common factor on all terms, the governing equation becomes

$$(1 + \alpha^2 y^2) \left(\frac{\partial^2 c}{\partial x^2} + \frac{\partial^2 c}{\partial y^2} \right) + 2\alpha^2 y \frac{\partial c}{\partial y} = 0 \quad (\text{D.144})$$

The solution of this equation with the given boundary conditions is simply

$$c = c_L + \frac{c_R - c_L}{L} x \quad (\text{D.145})$$

That is, the concentration varies linearly between the left and right boundaries.

The flux of interest is

$$j_x = -D_{\text{local}} \frac{\partial c}{\partial x} = -D_{\text{local}} \frac{c_R - c_L}{L} = D_0 (1 + \alpha^2 y^2) \frac{c_L - c_R}{L} \quad (\text{D.146})$$

Integrating this flux over a vertical line through the unit cell gives

$$J = \int_{-\frac{a}{2}}^{\frac{a}{2}} dy j_x = D_0 \frac{c_L - c_R}{L} \int_{-\frac{a}{2}}^{\frac{a}{2}} dy (1 + \alpha^2 y^2) = D_0 \frac{c_L - c_R}{L} a \left(1 + \frac{\alpha^2 a^2}{12}\right) \quad (\text{D.147})$$

Using this flux in Equation D.223, the effective diffusion coefficient is

$$D_{xx}^{\text{eff}} = -\frac{J L}{a \Delta c} = -D_0 \frac{c_L - c_R}{L} \left(1 + \frac{\alpha^2 a^2}{12}\right) \frac{L}{c_R - c_L} \quad (\text{D.148})$$

$$\boxed{D_{xx}^{\text{eff}} = D_0 \left(1 + \frac{\alpha^2 a^2}{12}\right)} \quad (\text{D.149})$$

In this case, the result is actually equivalent to the spatial average of D_{local} over the unit cell:

$$\frac{1}{aL} \int_{-\frac{L}{2}}^{\frac{L}{2}} dx \int_{-\frac{a}{2}}^{\frac{a}{2}} dy D_{\text{local}} = \frac{D_0}{a} \int_{-\frac{a}{2}}^{\frac{a}{2}} dy (1 + \alpha^2 y^2) = D_0 \left(1 + \frac{\alpha^2 a^2}{12}\right) \quad (\text{D.150})$$

This is analogous to one case presented in Section D.5, but this equivalence is not generally true for all D_{local} variations, as will be shown by the following example.

Now consider a spatially varying diffusion coefficient of the form

$$D_{\text{local}}(x, y) = D_{\text{local}}(x) = D_0 (1 + \alpha^2 x^2) \quad (\text{D.151})$$

This form has partial derivatives

$$\begin{aligned} \frac{\partial}{\partial x} (D_{\text{local}}) &= D_0 2\alpha^2 x \\ \frac{\partial}{\partial y} (D_{\text{local}}) &= 0 \end{aligned} \quad (\text{D.152})$$

After cancellation of the common factor D_0 , this results in a governing Fickian diffusion equation of

$$(1 + \alpha^2 x^2) \left(\frac{\partial^2 c}{\partial x^2} + \frac{\partial^2 c}{\partial y^2} \right) + 2\alpha^2 x \frac{\partial c}{\partial x} = 0 \quad (\text{D.153})$$

This equation can be solved with $c(x, y) = c(x)$, for which

$$\frac{\partial c}{\partial y} = 0 \quad (\text{D.154})$$

Then, defining

$$f = \frac{dc}{dx} \quad (\text{D.155})$$

the governing equation becomes

$$(1 + \alpha^2 x^2) \frac{df}{dx} + 2\alpha^2 x f = 0 \quad (\text{D.156})$$

$$\frac{df}{f} = -\frac{2\alpha^2 x}{1 + \alpha^2 x^2} f \quad (\text{D.157})$$

The equation is thus separable.

$$\int \frac{1}{f} df = -2\alpha^2 \int \frac{x}{1 + \alpha^2 x^2} dx \quad (\text{D.158})$$

A general form for the right-hand integral can be found in Gradshteyn et al. [50], as formula 2.103.5, for the case where $\alpha^2 > 0$, which requires only that α be real-valued. The result of the integrals is therefore

$$\ln |f| = -\ln |1 + \alpha^2 x^2| + \ln K_1 = \ln \frac{K_1}{|1 + \alpha^2 x^2|} \quad (\text{D.159})$$

Where $\ln K_1$ is the integration constant.

Exponentiating both sides, and taking the positive branch yields the solution

$$f = \frac{dc}{dx} = \frac{K_1}{1 + \alpha^2 x^2} \quad (\text{D.160})$$

Separating variables again and integrating both sides,

$$c = K_1 \int \frac{1}{1 + \alpha^2 x^2} dx \quad (\text{D.161})$$

This integral is also tabulated in Gradshteyn et al. [50] or Leithold [83]. The solution is

$$c(x) = \frac{K_1}{\alpha} \arctan(\alpha x) + K_2 \quad (\text{D.162})$$

where K_2 is the integration constant.

Applying the boundary conditions to solve for the integration constants,

$$\begin{aligned} K_2 &= \frac{c_L + c_R}{2} \\ K_1 &= \frac{c_R - c_L}{2 \arctan\left(\frac{\alpha L}{2}\right)} \alpha \end{aligned} \quad (\text{D.163})$$

The flux of interest is

$$j_x = -D_{\text{local}} \frac{\partial c}{\partial x} = -D_0 (1 + \alpha^2 x^2) \frac{c_R - c_L}{2 \arctan\left(\frac{\alpha L}{2}\right)} \frac{\alpha}{1 + \alpha^2 x^2} \quad (\text{D.164})$$

$$j_x = -D_0 \frac{c_R - c_L}{2 \arctan\left(\frac{\alpha L}{2}\right)} \alpha \quad (\text{D.165})$$

Integrating this flux over a vertical line through the unit cell gives

$$J = \int_{-\frac{a}{2}}^{\frac{a}{2}} dy j_x = -D_0 \frac{c_R - c_L}{2 \arctan\left(\frac{\alpha L}{2}\right)} \alpha a \quad (\text{D.166})$$

Again using the integrated flux in Equation D.223, the effective diffusion coefficient is

$$D_{xx}^{\text{eff}} = -\frac{J}{a} \frac{L}{\Delta c} = D_0 \frac{c_R - c_L}{2 \arctan\left(\frac{\alpha L}{2}\right)} \alpha \frac{L}{c_R - c_L} \quad (\text{D.167})$$

$$\boxed{D_{xx}^{\text{eff}} = D_0 \frac{\alpha L}{2 \arctan\left(\frac{\alpha L}{2}\right)}} \quad (\text{D.168})$$

In this case, the result is not the spatial average of the diffusion coefficient, but instead the inverse of the spatial average of the inverse:

$$\frac{1}{aL} \int_{-\frac{L}{2}}^{\frac{L}{2}} dx \int_{-\frac{a}{2}}^{\frac{a}{2}} dy \frac{1}{D_{\text{local}}} = \frac{1}{L} \int_{-\frac{L}{2}}^{\frac{L}{2}} dx \frac{1}{D_0 (1 + \alpha^2 x^2)} \quad (\text{D.169})$$

Using the same tabulated integrals as before, this is

$$\frac{1}{aL} \int_{-\frac{L}{2}}^{\frac{L}{2}} dx \int_{-\frac{a}{2}}^{\frac{a}{2}} dy \frac{1}{D_{\text{local}}} = \frac{1}{D_0 L} \frac{1}{\alpha} (\arctan(\alpha x)|_{x=\frac{L}{2}}^{x=-\frac{L}{2}}) \quad (\text{D.170})$$

Because arctan is an anti-symmetric function, this is

$$\frac{1}{aL} \int_{-\frac{L}{2}}^{\frac{L}{2}} dx \int_{-\frac{a}{2}}^{\frac{a}{2}} dy \frac{1}{D_{\text{local}}} = \frac{1}{D_0 \alpha L} 2 \arctan\left(\frac{\alpha L}{2}\right) \quad (\text{D.171})$$

And the inverse of this matches the result above.

Both of these problems can also be solved analytically using homogenization theory. From Equation D.38, the REV integral is

$$D_{ij}^{\text{eff}} = \frac{1}{|\Omega|} \int_{\Omega} d\Omega (D_{ij} - D_{ik} \partial_k \chi_j) \quad (\text{D.172})$$

For a case where D_{local} is isotropic,

$$D_{ij}(x, y) = D_{\text{local}}(x, y) \delta_{ij} \quad (\text{D.173})$$

Under this condition, the REV integral becomes

$$D_{ij}^{\text{eff}} = \frac{1}{|\Omega|} \int_{\Omega} d\Omega D_{\text{local}} (\delta_{ij} - \partial_i \chi_j) \quad (\text{D.174})$$

In this case, the desired component of the effective diffusion coefficient is the x - x component:

$$D_{xx}^{\text{eff}} = \frac{1}{|\Omega|} \int_{\Omega} d\Omega D_{\text{local}} (1 - \partial_x \chi_x) \quad (\text{D.175})$$

For the unit cell defined above, this is

$$D_{xx}^{\text{eff}} = \frac{1}{aL} \int_{-\frac{L}{2}}^{\frac{L}{2}} dx \int_{-\frac{a}{2}}^{\frac{a}{2}} dy D_{\text{local}} (1 - \partial_x \chi_x) \quad (\text{D.176})$$

Only the x -component of the corrector is required by this integral.

From Equation D.37, the corrector problem is

$$\partial_i (D_{ik} \partial_k \chi_j) = \partial_i D_{ij} \quad (\text{D.177})$$

For an isotropic local diffusion coefficient as described above, this becomes

$$\partial_i (D_{\text{local}} \partial_i \chi_j) = \partial_j D_{\text{local}} \quad (\text{D.178})$$

The equation for χ_x is therefore

$$\partial_x (D_{\text{local}} \partial_x \chi_x) + \partial_y (D_{\text{local}} \partial_y \chi_x) = \partial_x D_{\text{local}} \quad (\text{D.179})$$

For the condition where the local diffusion coefficient varies with y only, the partial derivatives are

$$\partial_x D_{\text{local}} = 0 \quad (\text{D.180})$$

$$\partial_y D_{\text{local}} = 2D_0 \alpha^2 y \quad (\text{D.181})$$

The corrector problem is therefore

$$D_0 (1 + \alpha^2 y^2) (\partial_x \partial_x \chi_x + \partial_y \partial_y \chi_x) + 2D_0 \alpha^2 y \partial_y \chi_x = 0 \quad (\text{D.182})$$

This equation can be solved with $\partial_x \chi_x = 0$. The REV integral of Equation D.176 is simply

$$D_{xx}^{\text{eff}} = \frac{1}{aL} \int_{-\frac{L}{2}}^{\frac{L}{2}} dx \int_{-\frac{a}{2}}^{\frac{a}{2}} dy D_{\text{local}} = \frac{D_0}{a} \int_{-\frac{a}{2}}^{\frac{a}{2}} dy (1 + \alpha^2 y^2) \quad (\text{D.183})$$

The result is therefore

$$D_{xx}^{\text{eff}} = D_0 \left(1 + \frac{\alpha^2 a^2}{12} \right) \quad (\text{D.184})$$

This matches the result from Equation D.149.

For the condition where the local diffusion coefficient varies with x only, the partial derivatives are

$$\partial_x D_{\text{local}} = 2D_0 \alpha^2 x \quad (\text{D.185})$$

$$\partial_y D_{\text{local}} = 0 \quad (\text{D.186})$$

The corrector problem is therefore

$$D_0 (1 + \alpha^2 x^2) (\partial_x \partial_x \chi_x + \partial_y \partial_y \chi_x) + 2D_0 \alpha^2 x \partial_x \chi_x = 2D_0 \alpha^2 x \quad (\text{D.187})$$

This equation is solvable with $\partial_y \chi_x = 0$. Defining

$$f = \partial_x \chi_x \quad (\text{D.188})$$

the corrector problem becomes the ordinary differential equation

$$(1 + \alpha^2 x^2) \frac{df}{dx} + 2\alpha^2 x f = 2\alpha^2 x \quad (\text{D.189})$$

This equation can be re-arranged as

$$\frac{df}{dx} + \frac{2\alpha^2 x}{1 + \alpha^2 x^2} (f - 1) = 0 \quad (\text{D.190})$$

Defining

$$g = f - 1 \quad (\text{D.191})$$

and noting that

$$\frac{dg}{dx} = \frac{df}{dx} \quad (\text{D.192})$$

the equation can then be expressed in the form

$$\frac{dg}{dx} = -\frac{2\alpha^2 x}{1 + \alpha^2 x^2} g \quad (\text{D.193})$$

This equation is separable:

$$\int \frac{1}{g} dg = -2\alpha^2 \int \frac{x}{1 + \alpha^2 x^2} dx \quad (\text{D.194})$$

The right-hand side can be integrated using formula 2.103.5 from Gradshteyn et al. [50]. After some further algebra, and selecting the proper branch of an absolute value, the result becomes

$$g = \frac{Q_1}{1 + \alpha^2 x^2} \quad (\text{D.195})$$

where Q_1 is an integration constant. The value of this constant can be obtained from the requirement that χ_x must be periodic.

$$\chi_x = \int \partial_x \chi_x dx = \int f dx = \int (1 + g) dx \quad (\text{D.196})$$

$$\chi_x = \int \left(1 + \frac{Q_1}{1 + \alpha^2 x^2} \right) dx = x + \frac{Q_1}{\alpha} \arctan(\alpha x) + Q_2 \quad (\text{D.197})$$

where Q_2 is an integration constant that does not affect the result. From this result, the values of χ_x at the right and left boundaries are

$$\chi_x \left(x = \frac{L}{2} \right) = \frac{L}{2} + \frac{Q_1}{\alpha} \arctan \left(\frac{\alpha L}{2} \right) + Q_2 \quad (\text{D.198})$$

$$\chi_x \left(x = -\frac{L}{2} \right) = -\frac{L}{2} + \frac{Q_1}{\alpha} \arctan \left(-\frac{\alpha L}{2} \right) + Q_2 \quad (\text{D.199})$$

Because arctan is an anti-symmetric function, the left boundary value is the same as

$$\chi_x \left(x = -\frac{L}{2} \right) = -\frac{L}{2} - \frac{Q_1}{\alpha} \arctan \left(\frac{\alpha L}{2} \right) + Q_2 \quad (\text{D.200})$$

For χ_x to be periodic, these values must satisfy

$$\chi_x \left(x = \frac{L}{2} \right) = \chi_x \left(x = -\frac{L}{2} \right) \quad (\text{D.201})$$

which can also be written as

$$\chi_x \left(x = \frac{L}{2} \right) - \chi_x \left(x = -\frac{L}{2} \right) = 0 \quad (\text{D.202})$$

Substituting the expressions for χ_x at the boundaries into this equation gives

$$L + 2\frac{Q_1}{\alpha} \arctan \left(\frac{\alpha L}{2} \right) = 0 \quad (\text{D.203})$$

Solving for Q_1 , this yields

$$Q_1 = -\frac{\alpha L}{2 \arctan \left(\frac{\alpha L}{2} \right)} \quad (\text{D.204})$$

The REV integral of Equation D.176 involves the expression

$$1 - \partial_x \chi_x = 1 - f = 1 - (1 + g) = -g \quad (\text{D.205})$$

And so, the REV integral becomes

$$D_{xx}^{\text{eff}} = \frac{1}{aL} \int_{-\frac{L}{2}}^{\frac{L}{2}} dx \int_{-\frac{a}{2}}^{\frac{a}{2}} dy D_{\text{local}} (1 - \partial_x \chi_x) = -\frac{1}{L} \int_{-\frac{L}{2}}^{\frac{L}{2}} dx D_{\text{local}} g \quad (\text{D.206})$$

$$D_{xx}^{\text{eff}} = -\frac{1}{L} \int_{-\frac{L}{2}}^{\frac{L}{2}} dx D_0 (1 + \alpha^2 x^2) \frac{Q_1}{1 + \alpha^2 x^2} = -\frac{1}{L} \int_{-\frac{L}{2}}^{\frac{L}{2}} dx D_0 Q_1 \quad (\text{D.207})$$

And so the final result is

$$D_{xx}^{\text{eff}} = -D_0 Q_1 = D_0 \frac{\alpha L}{2 \arctan \left(\frac{\alpha L}{2} \right)} \quad (\text{D.208})$$

which matches the result in Equation D.168.

This example problem with a spatially varying local diffusion coefficient has therefore illustrated that the same result for the effective diffusion coefficient can be obtained from an integrated flux calculation and from homogenization theory.

D.7 Conditions for Symmetry of the Homogenized Diffusion Coefficient Matrix

The purpose of this section is to investigate conditions that would lead to the symmetry of an effective diffusion coefficient computed from Equation 2.13. A symmetric effective diffusion coefficient must satisfy $D_{ij}^{\text{eff}} = D_{ji}^{\text{eff}}$. Equivalently, a symmetric effective diffusion coefficient will satisfy $\Delta_{ij} = 0$, where

$$\Delta_{ij} = D_{ij}^{\text{eff}} - D_{ji}^{\text{eff}} \quad (\text{D.209})$$

Substituting into this expression the domain integral of Equation 2.13,

$$\Delta_{ij} = \frac{1}{|\Omega|} \int_{\Omega} d\Omega (D_{ij} - D_{ik} \partial_k \chi_j) - \frac{1}{|\Omega|} \int_{\Omega} d\Omega (D_{ji} - D_{jk} \partial_k \chi_i) \quad (\text{D.210})$$

Combining the integrals,

$$\Delta_{ij} = \frac{1}{|\Omega|} \int_{\Omega} d\Omega (D_{ij} - D_{ji} + D_{jk} \partial_k \chi_i - D_{ik} \partial_k \chi_j) \quad (\text{D.211})$$

As noted in Section 1.7 the local diffusion coefficient, D_{ij} , is usually symmetric. (If not, there is little hope of symmetry at larger scales.) Thus, $D_{ij} - D_{ji} = 0$, and so

$$\Delta_{ij} = \frac{1}{|\Omega|} \int_{\Omega} d\Omega (D_{jk} \partial_k \chi_i - D_{ik} \partial_k \chi_j) \quad (\text{D.212})$$

In the strict sense, this is the necessary condition for symmetry of the effective diffusion coefficient matrix. The integrand may change sign over regions of the problem domain in unpredictable ways, so while this indicates that symmetry of the effective diffusion coefficient matrix is possible, Equation D.212 does not provide a convenient way to assess if a given problem will have a symmetric matrix or not.

Further insight may be gained by considering a condition that is not *necessary*, but is *sufficient* for the symmetry of the matrix. Specifically, consider the condition where the integrand is zero at all locations in the problem domain. That is, if

$$\Delta_{ij} = \frac{1}{|\Omega|} \int_{\Omega} d\Omega f_{ij} \quad (\text{D.213})$$

where

$$f_{ij} = D_{jk} \partial_k \chi_i - D_{ik} \partial_k \chi_j \quad (\text{D.214})$$

then clearly $f_{ij} = 0$ is clearly a sufficient condition (though not necessary) for $\Delta_{ij} = 0$.

Note that f_{ij} is anti-symmetric:

$$f_{ij} = -f_{ji} \quad (\text{D.215})$$

$$f_{ij} = 0 \text{ where } i = j \quad (\text{D.216})$$

To illustrate that f_{ij} is not guaranteed to be zero, consider a two-dimensional problem. In this case, $f_{12} = -f_{21}$ is the only off-diagonal element. Expanding the indices, this element is explicitly:

$$f_{12} = D_{2k}\partial_k\chi_1 - D_{1k}\partial_k\chi_2 \quad (\text{D.217})$$

$$= D_{21}\partial_1\chi_1 - D_{11}\partial_1\chi_2 + D_{22}\partial_2\chi_1 - D_{12}\partial_2\chi_2 \quad (\text{D.218})$$

$$= -D_{11}\partial_1\chi_2 + D_{12}(\partial_1\chi_1 - \partial_2\chi_2) + D_{22}\partial_2\chi_1 \quad (\text{D.219})$$

While the condition $f_{12} = 0$ would result in a symmetric matrix for a two-dimensional problem, the condition is complicated enough that it would not appear to be true in general. Indeed, setting up a two-dimensional problem where this was the case would not be easy.

In summary, there can be situations in which the effective diffusion coefficient matrix is not symmetric, and the most convenient way to assess its symmetry is to solve the corrector problem and then evaluate the effective diffusion coefficient matrix directly. In some cases, such as the example in Section D.5, the result will be symmetric. But in other cases it may not be. The symmetry of the effective diffusion coefficient matrix cannot be guaranteed.

D.8 Effective Diffusion Coefficient from Solution of Fick's Law

For sufficiently simple three-dimensional geometries, the effective diffusion coefficient can be computed directly from the concentration and flux fields obtained by solution of the Fickian diffusion problem at the smaller scale. This section presents the formulas for such calculation. Because this procedure does not rely on homogenization, it can be used to verify homogenization results in some cases. For the purpose of this section, index notation is not used.

To compute the effective diffusion constant, the three-dimensional diffusion problem is considered from the perspective of a simpler one-dimensional diffusion problem. For the application of Section 3.3, the one-dimensional problem is diffusion across the membrane. The Fickian diffusion equation in one dimension can be written as

$$j = -D_{\text{bulk}} \frac{dc}{ds} \quad (\text{D.220})$$

where:

s = position within the one-dimensional domain

j = $j(s)$ = flux at any point, in units of
number of particles per unit area per unit time

D_{bulk} = diffusion constant of the medium, in units of area per unit time

c = $c(s)$ = concentration at any point, in units of
number of particles per unit volume

$\frac{dc}{ds}$ = first spatial derivative of concentration

Note that in the one-dimensional problem, the flux j is a scalar rather than a vector.

The three-dimensional problem is converted to an equivalent one-dimensional problem by integrating over the area of the unit cell, in the two directions perpendicular to the one-dimensional diffusion problem. The total flux across the membrane will be given by:

$$J_{\text{cell}} = -D_{\text{bulk}} \int_{\text{cell}} dA \frac{\partial c}{\partial s} \quad (\text{D.221})$$

Define the effective diffusion constant such that the integrated flux is the same, when used with an the average concentration gradient across the membrane:

$$J_{\text{cell}} = -D_{\text{eff}} A_{\text{cell}} \frac{\Delta c}{\Delta s} \quad (\text{D.222})$$

where:

J_{cell} = integral of flux over the pore, in units of
number of particles per unit time

A_{cell} = area of unit cell

D_{eff} = unknown effective diffusion constant

Δc = change in concentration

Δs = distance over which concentration changes

Re-arranging this equation to solve for the unknown D_{eff} :

$$D_{\text{eff}} = -\frac{J_{\text{cell}} \Delta s}{A_{\text{cell}} \Delta c} \quad (\text{D.223})$$

The integrated flux, J_{model} , is calculated from the model by integrating the ion flux over a surface parallel to the membrane surface. The result should be the same for any such surface capturing the full extents of the model. That is, the integrated flux should be the same when integrating over the model pore as when integrating over the upgradient or downgradient boundary of the model.

Specifically, the integrated flux is calculated as:

$$J_{\text{model}} = \int_{\text{model}} dA \left(\hat{n} \cdot \vec{j} \right) = -D_{\text{bulk}} \int_{\text{model}} dA \left(\hat{n} \cdot \vec{\nabla} c \right) \quad (\text{D.224})$$

where \hat{n} is the directed normal to the surface, and c is the concentration field found by solving the model.

The model of Section 3.3 used two planes of symmetry to reduce the mesh size. Consequently, the flux obtained by integration is only one quarter of the total for the unit cell. That is, $J_{\text{cell}} = 4J_{\text{model}}$. Using the distances defined in Section 3.2, $A_{\text{cell}} = 4LxLy$:

$$D_{\text{eff}} = -\frac{4J_{\text{model}} \Delta s}{4LxLy \Delta c} = -\frac{J_{\text{model}} \Delta s}{LxLy \Delta c} \quad (\text{D.225})$$

For convenience, define the integral

$$I_{\text{gc}} = \int_{\text{model}} dA \left(\hat{n} \cdot \vec{\nabla} c \right) \quad (\text{D.226})$$

then the flux integral is simply

$$J_{\text{model}} = -D_{\text{bulk}} I_{\text{gc}} \quad (\text{D.227})$$

and the effective diffusion constant is

$$D_{\text{eff}} = D_{\text{bulk}} \frac{I_{\text{gc}}}{LxLy} \frac{\Delta s}{\Delta c} \quad (\text{D.228})$$

This can also be written as

$$\frac{D_{\text{eff}}}{D_{\text{bulk}}} = \frac{I_{\text{gc}}}{LxLy} \frac{\Delta s}{\Delta c} \quad (\text{D.229})$$

The values of Δc and Δs are calculated by extracting the concentration result at two points located symmetrically on opposite sides of the membrane. The difference in concentration between these two points is Δc , and the distance between them is Δs .

Slightly different results for the value of D_{eff} could be attained by selecting different pairs of symmetrically located points. The results in Section 3.3 were taken with these two points located along the centerline of the pore, at both faces of the membrane.

D.9 Reactive Boundary Condition

The purpose of this section is to derive the weak form needed to implement the reactive boundary condition described in Section 3.5. The method presented here is similar to that of Song et al. [123].

First, assume the presence of an enzyme that catalyzes the reaction $R+E \rightarrow P+E$, where R is the reactant, P is the product, and E is the enzyme. The reaction is rate-limited by the diffusion of the reactants and products to and from the active site. The reaction can therefore be simulated by equating the flux of reactant to the active site and the flux of product away:

$$-j_{Pi} = j_{Ri} \quad (\text{D.230})$$

The flux of each species is related to its concentration through the Smoluchowski equation, with the potential fully controlled by electrostatics. Assuming an isotropic diffusion constant, D , which is the same for the two species, this gives:

$$j_{Si} = -De^{-\beta z_S \Phi} \partial_i (e^{\beta z_S \Phi} c_S) \quad (\text{D.231})$$

The Slotboom transformation is given by:

$$\bar{D}_S = De^{-\beta z_S \Phi} \quad (\text{D.232})$$

$$\bar{c}_S = c_S e^{\beta z_S \Phi} \quad (\text{D.233})$$

Note that while D is the same for both species, \bar{D}_S is not, because it depends on the species charge.

Applying the Slotboom transformation, the flux definition for each species is:

$$j_{Pi} = -\bar{D}_P \partial_i \bar{c}_P \quad (\text{D.234})$$

$$j_{Ri} = -\bar{D}_R \partial_i \bar{c}_R \quad (\text{D.235})$$

The reactive boundary condition is therefore:

$$\bar{D}_P \partial_i \bar{c}_P = -\bar{D}_R \partial_i \bar{c}_R \quad (\text{D.236})$$

The general weak form for species S of the Smoluchowski equation is

$$\int_{\Omega} d\Omega \partial_t(c_S) v_S = \int_{\partial\Omega} d\Gamma \bar{D}_{Sij} n_{\Gamma i} \partial_j (\bar{c}_S) v_S - \int_{\Omega} d\Omega \bar{D}_{Sij} \partial_j (\bar{c}_S) \partial_i (v_S) \quad (\text{D.237})$$

(Note that c_S on the left hand side is not Slotboom-transformed.)

For isotropic diffusion, this simplifies to

$$\int_{\Omega} d\Omega \partial_t(c_S) v_S = \int_{\partial\Omega} d\Gamma \bar{D}_S n_{\Gamma i} \partial_i (\bar{c}_S) v_S - \int_{\Omega} d\Omega \bar{D}_S \partial_i (\bar{c}_S) \partial_i (v_S) \quad (\text{D.238})$$

The complete weak form, including both species, is therefore

$$\begin{aligned} & \int_{\Omega} d\Omega \partial_t(c_P) v_P + \int_{\Omega} d\Omega \partial_t(c_R) v_R = \\ & \int_{\partial\Omega} d\Gamma \bar{D}_P n_{\Gamma i} \partial_i (\bar{c}_P) v_P + \int_{\partial\Omega} d\Gamma \bar{D}_R n_{\Gamma i} \partial_i (\bar{c}_R) v_R \\ & - \int_{\Omega} d\Omega \bar{D}_P \partial_i (\bar{c}_P) \partial_i (v_P) - \int_{\Omega} d\Omega \bar{D}_R \partial_i (\bar{c}_R) \partial_i (v_R) \end{aligned} \quad (\text{D.239})$$

For the reactive boundary, define a single boundary term, BT , that is the sum of the boundary terms for the two species:

$$BT = \int_{\Gamma_{react}} d\Gamma \bar{D}_P n_{\Gamma i} \partial_i (\bar{c}_P) v_P + \int_{\Gamma_{react}} d\Gamma \bar{D}_R n_{\Gamma i} \partial_i (\bar{c}_R) v_R \quad (\text{D.240})$$

$$BT = \int_{\Gamma_{react}} d\Gamma n_{\Gamma i} (\bar{D}_P \partial_i (\bar{c}_P) v_P + \bar{D}_R \partial_i (\bar{c}_R) v_R) \quad (\text{D.241})$$

Substituting in the reactive boundary condition ($\bar{D}_P \partial_i \bar{c}_P = -\bar{D}_R \partial_i \bar{c}_R$), this becomes

$$BT = \int_{\Gamma_{react}} d\Gamma n_{\Gamma i} (-\bar{D}_R \partial_i (\bar{c}_R) v_P + \bar{D}_R \partial_i (\bar{c}_R) v_R) \quad (\text{D.242})$$

$$BT = \int_{\Gamma_{react}} d\Gamma \bar{D}_R n_{\Gamma i} \partial_i (\bar{c}_R) (v_R - v_P) \quad (\text{D.243})$$

This is the boundary term that should be included in the weak form for each reactive boundary.

Using vector calculus notation, this term is

$$BT = \int_{\Gamma_{react}} d\Gamma \bar{D}_R (\hat{n} \cdot \nabla \bar{c}_R) (v_R - v_P) \quad (D.244)$$

Note that the term could be written equivalently as

$$BT = \int_{\Gamma_{react}} d\Gamma \bar{D}_P (\hat{n} \cdot \nabla \bar{c}_P) (v_P - v_R) \quad (D.245)$$

D.10 Langevin Dynamics in a Harmonic Potential

Consider a particle simultaneously subjected to Brownian motion and overdamped harmonic oscillation, as discussed in Section 4.2. The applicable equation of motion is a Langevin equation. Beginning with Equation 4.1:

$$M \partial_t \partial_t x_i = -\xi \partial_t x_i - \partial_i U(x_i) + F_i \quad (D.246)$$

where

$$\begin{aligned} M &= \text{particle mass} \llbracket \text{M} \rrbracket \\ x_i &= \text{time-dependent particle position vector} \llbracket \text{L} \rrbracket \\ \xi &= \text{coefficient of friction} \llbracket \frac{\text{M}}{\text{T}} \rrbracket \\ F_i &= \text{force varying randomly in time} \llbracket \text{F} \rrbracket \\ U &= \text{harmonic restraining potential} \llbracket \text{E} \rrbracket \\ &= \frac{1}{2} K (x_i - a_i)^2 \\ K &= \text{spring constant defining harmonic potential strength} \llbracket \frac{\text{F}}{\text{L}} \rrbracket \\ a_i &= \text{position vector for center of harmonic potential} \llbracket \text{L} \rrbracket \\ \partial_i U(x_i) &= K (x_i - a_i) \llbracket \text{F} \rrbracket \end{aligned}$$

In the limit of strong friction

$$|\xi \partial_t x_i| \gg |M \partial_t \partial_t x_i| \quad (D.247)$$

Consequently, the overdamped condition may be expressed as

$$M \partial_t \partial_t x_i \rightarrow 0 \quad (D.248)$$

The Langevin equation is the same in each coordinate direction, and there are no terms coupling orthogonal components, so each may be component may be considered independently. Defining $q = x_i - a_i$ such that $U = \frac{1}{2} K q^2$, and with $f = F_i$ for convenience, the equation of motion for a single direction may be expressed as

$$\xi \partial_t q = -Kq + f \quad (D.249)$$

The MSD can be obtained by assuming a steady-state condition. In this condition, the probability distribution for the particle location will be a Boltzmann distribution.

$$p(q) = Ce^{-\beta U} \quad (\text{D.250})$$

where

$$\begin{aligned} p(q) &= \text{probability density of particle at position } q \llbracket \mathbf{L}^{-N_d} \rrbracket \\ C &= \text{normalization constant for probability density} \llbracket \mathbf{L}^{-N_d} \rrbracket \end{aligned}$$

The normalization constant can be found from the requirement that the integral of the probability density is 1.

$$C \int_{\Omega} d\Omega e^{-\frac{1}{2}\beta K q^2} = 1 \quad (\text{D.251})$$

This is a Gaussian integral. The solution is

$$C = \sqrt{\frac{\beta K}{2\pi}} \quad (\text{D.252})$$

The MSD can be calculated directly from the probability distribution.

$$\langle q^2 \rangle = \int_{\Omega} d\Omega p(q) q^2 \quad (\text{D.253})$$

$$\langle q^2 \rangle = \sqrt{\frac{\beta K}{2\pi}} \int_{\Omega} d\Omega q^2 e^{-\frac{1}{2}\beta K q^2} \quad (\text{D.254})$$

This is another Gaussian integral.

$$\langle q^2 \rangle = \sqrt{\frac{\beta K}{2\pi}} \frac{1}{2} \sqrt{\pi} \left(\frac{2}{\beta K} \right)^{\frac{3}{2}} \quad (\text{D.255})$$

$$\boxed{\langle q^2 \rangle = \frac{1}{\beta K}} \quad (\text{D.256})$$

This is the result presented in Equation 4.2. Other derivations of this MSD can be obtained from the equipartition theorem [98, 108].

The ACF can be obtained directly from the Langevin equation. The procedure shown here follows a similar procedure shown in Reif [108]. Equation D.249 is integrated with respect to time over an interval Δt starting at $t = s$.

$$\xi \int_s^{s+\Delta t} dt \partial_t q = -K \int_s^{s+\Delta t} dt q(t) + \int_s^{s+\Delta t} dt f \quad (\text{D.257})$$

From the fundamental theorem of calculus, this is

$$\xi (q(s + \Delta t) - q(s)) = -K \int_s^{s+\Delta t} dt q(t) + \int_s^{s+\Delta t} dt f \quad (\text{D.258})$$

Multiply both sides of this equation by $q(t = 0)$ and take the ensemble average.

$$\xi (\langle q(0)q(s + \Delta t) - q(0)q(s) \rangle) = -K \langle q(0) \int_s^{s+\Delta t} dt q(t) \rangle + \langle q(0) \int_s^{s+\Delta t} dt f \rangle \quad (\text{D.259})$$

The last term is zero because q is independent of f . Divide the remaining terms by Δt and take the limit $\Delta t \rightarrow 0$.

$$\xi \lim_{\Delta t \rightarrow 0} \frac{\langle q(0)q(s + \Delta t) - q(0)q(s) \rangle}{\Delta t} = \lim_{\Delta t \rightarrow 0} -K \frac{\langle q(0) \int_s^{s+\Delta t} dt q(t) \rangle}{\Delta t} \quad (\text{D.260})$$

$$\xi \frac{d}{ds} \langle q(0)q(s) \rangle = -K \langle q(0)q(s) \rangle \quad (\text{D.261})$$

The solution of this differential equation is

$$\langle q(0)q(s) \rangle = C e^{-\frac{K}{\xi} s} \quad (\text{D.262})$$

The integration constant can be found from the requirement that

$$\langle q(0)q(s = 0) \rangle = \langle q^2 \rangle \quad (\text{D.263})$$

$$C = \langle q^2 \rangle \quad (\text{D.264})$$

Replacing the variable s with t :

$$\boxed{\langle q(0)q(t) \rangle = \langle q^2 \rangle e^{-\frac{t}{\tau}}} \quad (\text{D.265})$$

where

$$\boxed{\tau = \frac{\xi}{K}} \quad (\text{D.266})$$

This is the result presented in Equation 4.3.

D.11 Gauge-Dependence in the Homogenized Smoluchowski Equation with the Slotboom Transformation

This section illustrates how the effective diffusion coefficient result of the homogenized Smoluchowski diffusion problem with the Slotboom transformation is affected by shifting the potential by a constant value. The corrector problem for this situation is shown in Equation D.267, and the REV integral is shown in Equation D.268.

$$\partial_i (\bar{D}_{ik} \partial_k \chi_j) = \partial_i \bar{D}_{ij} \quad (\text{D.267})$$

$$\bar{D}_{ij}^{\text{eff}} = \frac{1}{|\Omega|} \int_{\Omega} d\Omega (\bar{D}_{ij} - \bar{D}_{ik} \partial_k \chi_j) \quad (\text{D.268})$$

The potential is shifted by a constant value Λ :

$$\Psi \longrightarrow \Psi + \Lambda \quad (\text{D.269})$$

The effect on \bar{D} is shown in Equation D.270.

$$\bar{D}_{ij} = D_{ij}e^{-\beta\Psi} \longrightarrow D_{ij}e^{-\beta\Psi}e^{-\beta\Lambda} = e^{-\beta\Lambda}\bar{D}_{ij} \quad (\text{D.270})$$

Substituting this into the corrector problem,

$$\partial_i (e^{-\beta\Lambda}\bar{D}_{ik}\partial_k\chi_j) = \partial_i (e^{-\beta\Lambda}\bar{D}_{ij}) \quad (\text{D.271})$$

Because $e^{-\beta\Lambda}$ is spatially invariant, this becomes

$$e^{-\beta\Lambda}\partial_i (\bar{D}_{ik}\partial_k\chi_j) = e^{-\beta\Lambda}\partial_i\bar{D}_{ij} \quad (\text{D.272})$$

The exponential constant on both sides can be canceled out, and so the corrector problem is unaffected by the shift of the potential.

Substituting into the REV integral, however,

$$\bar{D}_{ij}^{\text{eff}} = \frac{1}{|\Omega|} \int_{\Omega} d\Omega (e^{-\beta\Lambda}\bar{D}_{ij} - e^{-\beta\Lambda}\bar{D}_{ik}\partial_k\chi_j) \quad (\text{D.273})$$

$$\bar{D}_{ij}^{\text{eff}} = e^{-\beta\Lambda} \frac{1}{|\Omega|} \int_{\Omega} d\Omega (\bar{D}_{ij} - \bar{D}_{ik}\partial_k\chi_j) \quad (\text{D.274})$$

Thus, $\bar{D}_{ij}^{\text{eff}}$ is scaled by a factor that is exponential in the shift value of the potential. This is consistent with an interpretation of the homogenization result as \bar{D} , which is a gauge-dependent quantity, rather than as D .

If the result of homogenization is \bar{D} rather than D , how can the effective diffusion coefficient be obtained from the homogenized Smoluchowski equation? One possible solution would be to obtain a factor that performs the transformation between these two quantities, analogous to the Slotboom transformation at the smaller scale.

Consider a factor Ξ such that

$$\bar{D}_{\text{eff}} = D_{\text{eff}}\Xi \quad (\text{D.275})$$

Presumably, Ξ would be a scalar constant for the larger scale, but would depend on the potential at the smaller scale. That is, Ξ would be a functional of the potential. If such a functional could be found, then after the homogenized \bar{D} was obtained, the desired effective diffusion coefficient would be obtained by

$$D_{\text{eff}} = \frac{\bar{D}_{\text{eff}}}{\Xi} \quad (\text{D.276})$$

Further insight into this issue, and a possible form of the functional $\Xi(\psi)$ is presented in Section D.12.

D.12 An Example Problem for the Homogenized Smoluchowski Equation

This section presents an example problem of homogenized Smoluchowski diffusion, where the potential includes an explicit additive constant. The problem is sufficiently simple that an effective diffusion coefficient can also be obtained without the use of homogenization theory. Comparing the results of the two methods provides insight into the proper interpretation of the homogenization result.

The problem consists of a two-dimensional unit cell where a single chemical species diffuses while subjected to a potential varying only in one direction. For the purpose of clarity, index notation will not be used in this section.

The problem is illustrated in Figure D.3. The dimensions of the unit cell are a by L , with a potential defined by Equation D.277, where A is a scaling coefficient, and B is the explicit constant shift for the potential. Both of these constants may be freely selected. In particular, changes to B should not affect any physically measurable quantities, including the concentration, c , (although \bar{c} will be affected), the flux, and the resulting effective diffusion coefficient.

$$\psi(y) = Ay^2 + B \quad (\text{D.277})$$

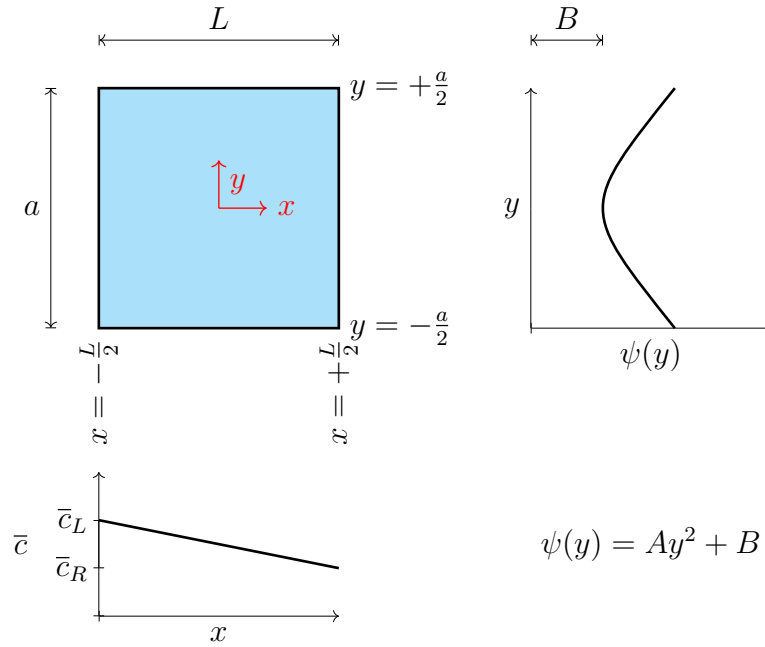


Figure D.3: Unit cell geometry, potential, and solution for the example Smoluchowski diffusion problem.

The boundary conditions for the problem are given by Equation D.278 in terms of the Slotboom-transformed variables. The resulting concentration field will give a Boltzmann distribution for the concentration at each value of x , as shown in Equation D.279 for the boundaries. The local diffusion coefficient, D , is isotropic and spatially

invariant. Under these conditions, the solution of the Slotboom-transformed Smoluchowski diffusion problem is that \bar{c} will vary linearly with y , as shown in Figure D.3.

$$\begin{aligned}\bar{c}\left(x = -\frac{L}{2}\right) &= \bar{c}_L \\ \bar{c}\left(x = +\frac{L}{2}\right) &= \bar{c}_R\end{aligned}\tag{D.278}$$

$$\begin{aligned}c\left(x = -\frac{L}{2}, y\right) &= \bar{c}_L e^{-\beta\psi(y)} \\ c\left(x = +\frac{L}{2}, y\right) &= \bar{c}_R e^{-\beta\psi(y)}\end{aligned}\tag{D.279}$$

The objective here is to obtain the effective diffusion coefficient for the x -direction, D_{xx}^{eff} . First, this can be done using the integrated flux as shown in Section D.8. For this approach, the x -component of the flux, j_x is needed. Starting from the Smoluchowski flux definition, in Slotboom-transformed form,

$$j_x = -\bar{D} \frac{\partial \bar{c}}{\partial x}\tag{D.280}$$

Substituting in the Slotboom-transformed diffusion coefficient and the constant slope of \bar{c} from above, this becomes

$$j_x = -D e^{-\beta\psi(y)} \frac{\bar{c}_R - \bar{c}_L}{L} = D \frac{\bar{c}_L - \bar{c}_R}{L} e^{-\beta\psi(y)}\tag{D.281}$$

The integrated flux of interest is

$$J = \int_{-\frac{a}{2}}^{\frac{a}{2}} dy j_x\tag{D.282}$$

Using the result for j_x from above, this is

$$J = D \frac{\bar{c}_L - \bar{c}_R}{L} \int_{-\frac{a}{2}}^{\frac{a}{2}} dy e^{-\beta\psi(y)}\tag{D.283}$$

Applying the form of the potential from Equation D.277,

$$J = D \frac{\bar{c}_L - \bar{c}_R}{L} \int_{-\frac{a}{2}}^{\frac{a}{2}} dy e^{-\beta(Ay^2+B)}\tag{D.284}$$

This simplifies to

$$J = D \frac{\bar{c}_L - \bar{c}_R}{L} e^{-\beta B} \int_{-\frac{a}{2}}^{\frac{a}{2}} dy e^{-\beta A y^2}\tag{D.285}$$

Defining the Gaussian integral

$$I(A) = \frac{1}{a} \int_{-\frac{a}{2}}^{\frac{a}{2}} dy e^{-\beta A y^2} = 2 \int_0^{\frac{1}{2}} ds e^{-\beta A a^2 s^2}\tag{D.286}$$

The integrated flux is

$$J = D \frac{\bar{c}_L - \bar{c}_R}{L} e^{-\beta B} a I(A)\tag{D.287}$$

From Equation D.223, the effective diffusion coefficient is

$$D_{xx}^{\text{eff}} = -\frac{J}{a} \frac{L}{\Delta c} \quad (\text{D.288})$$

The concentration gradient to be used in Equation D.288 should be the average gradient over the unit cell. (Note: this definition of the large-scale gradient may be inconsistent with the large-scale steady-state solution of the Smoluchowski equation. An alternative definition of the large-scale gradient may be better. This issue is unresolved at the time of this writing.) This can be obtained by taking the average concentration over the boundaries and computing the gradient between these two average concentrations, or by taking the gradient at each value of y and then averaging the gradients over the unit cell. Both approaches give the same average gradient in this case.

First, taking the average concentration at each boundary,

$$c_{\text{average}}(x) = \frac{1}{a} \int_{-\frac{a}{2}}^{\frac{a}{2}} dy \bar{c}(x) e^{-\beta\psi(y)} = \bar{c}(x) \frac{1}{a} \int_{-\frac{a}{2}}^{\frac{a}{2}} dy e^{-\beta\psi(y)} \quad (\text{D.289})$$

and so

$$\frac{\Delta c}{L} = \frac{c_{\text{average}}(x = L/2) - c_{\text{average}}(x = -L/2)}{L} = \frac{\bar{c}_R - \bar{c}_L}{L} \frac{1}{a} \int_{-\frac{a}{2}}^{\frac{a}{2}} dy e^{-\beta\psi(y)} \quad (\text{D.290})$$

For the approach of taking the average of the gradients,

$$\Delta c(y) = c(x = L/2) - c(x = -L/2) = (\bar{c}_R - \bar{c}_L) e^{-\beta\psi(y)} \quad (\text{D.291})$$

and so the average of the gradient over the unit cell is

$$\frac{\Delta c}{L} = \frac{1}{a} \int_{-\frac{a}{2}}^{\frac{a}{2}} dy \frac{\Delta c(y)}{L} = \frac{1}{aL} \int_{-\frac{a}{2}}^{\frac{a}{2}} dy (\bar{c}_R - \bar{c}_L) e^{-\beta\psi(y)} = \frac{\bar{c}_R - \bar{c}_L}{L} \frac{1}{a} \int_{-\frac{a}{2}}^{\frac{a}{2}} dy e^{-\beta\psi(y)} \quad (\text{D.292})$$

As indicated above, this is the same result for the average gradient for both approaches. This expression can be further expanded as

$$\frac{\Delta c}{L} = \frac{\bar{c}_R - \bar{c}_L}{L} e^{-\beta B} \frac{1}{a} \int_{-\frac{a}{2}}^{\frac{a}{2}} dy e^{-\beta A y^2} = \frac{\bar{c}_R - \bar{c}_L}{L} e^{-\beta B} I(A) \quad (\text{D.293})$$

Using this average gradient and the integrated flux from Equation D.287 in Equation D.288, the effective diffusion coefficient is

$$D_{xx}^{\text{eff}} = -\frac{J}{a} \frac{L}{\Delta c} = D \frac{\bar{c}_L - \bar{c}_R}{L} e^{-\beta B} I(A) \frac{L}{-\Delta c} \quad (\text{D.294})$$

$$D_{xx}^{\text{eff}} = D \frac{\bar{c}_L - \bar{c}_R}{L} e^{-\beta B} I(A) \frac{L}{\bar{c}_L - \bar{c}_R} \frac{1}{e^{-\beta B} I(A)} \quad (\text{D.295})$$

$$\boxed{D_{xx}^{\text{eff}} = D} \quad (\text{D.296})$$

This result reflects the fact that the potential does not vary in the x -direction, so there is no force applied to the diffusing particles in this direction. Consequently, the potential has no effect on the effective diffusion coefficient in this direction.

For the homogenization approach, the end result in this case comes from the integral

$$\overline{D}_{xx}^{\text{eff}} = \frac{1}{|\Omega|} \int_{\Omega} d\Omega \left(\overline{D}_{xx} - \overline{D}_{xx} \partial_x \chi_x - \overline{D}_{xy} \partial_y \chi_x \right) \quad (\text{D.297})$$

Because of the isotropic local diffusion coefficient, $\overline{D}_{xx} = \overline{D}$ and $\overline{D}_{xy} = 0$. Thus,

$$\overline{D}_{xx}^{\text{eff}} = \frac{1}{aL} \int_{-\frac{L}{2}}^{\frac{L}{2}} dx \int_{-\frac{a}{2}}^{\frac{a}{2}} dy \left(\overline{D} - \overline{D} \partial_x \chi_x \right) \quad (\text{D.298})$$

This simplifies to

$$\overline{D}_{xx}^{\text{eff}} = \frac{1}{aL} \int_{-\frac{L}{2}}^{\frac{L}{2}} dx \int_{-\frac{a}{2}}^{\frac{a}{2}} dy \overline{D} (1 - \partial_x \chi_x) \quad (\text{D.299})$$

$$\overline{D}_{xx}^{\text{eff}} = \frac{D}{aL} \int_{-\frac{L}{2}}^{\frac{L}{2}} dx \int_{-\frac{a}{2}}^{\frac{a}{2}} dy e^{-\beta\psi(y)} (1 - \partial_x \chi_x) \quad (\text{D.300})$$

Note that only the x -component of the corrector is needed, χ_x . (In fact, only one of its partial derivatives is needed.) The corrector problem corresponding to this component is

$$\partial_x (\overline{D} \partial_x \chi_x) + \partial_y (\overline{D} \partial_y \chi_x) = \partial_x \overline{D} \quad (\text{D.301})$$

Substituting in the expression for \overline{D} , the constant coefficient D cancels out, leaving

$$\partial_x (e^{-\beta\psi(y)} \partial_x \chi_x) + \partial_y (e^{-\beta\psi(y)} \partial_y \chi_x) = \partial_x e^{-\beta\psi(y)} \quad (\text{D.302})$$

Applying the partial derivatives and the product rule,

$$e^{-\beta\psi(y)} \partial_x \partial_x \chi_x + e^{-\beta\psi(y)} \partial_y \partial_y \chi_x + \partial_y (e^{-\beta\psi(y)}) \partial_y \chi_x = 0 \quad (\text{D.303})$$

$$e^{-\beta\psi(y)} \partial_x \partial_x \chi_x + e^{-\beta\psi(y)} \partial_y \partial_y \chi_x - \beta e^{-\beta\psi(y)} \partial_y (\psi(y)) \partial_y \chi_x = 0 \quad (\text{D.304})$$

The exponentials cancel out as well, leaving

$$\partial_x \partial_x \chi_x + \partial_y \partial_y \chi_x - \beta \partial_y (\psi(y)) \partial_y \chi_x = 0 \quad (\text{D.305})$$

This problem can be solved by χ_x of the form

$$\partial_y \chi_x = Q_1 e^{\beta A y^2} \quad (\text{D.306})$$

for constant Q_1 . (In fact, χ_x must be periodic, which requires $Q_1 = 0$.) This solution results in $\partial_x \chi_x = 0$. Substituting this result into Equation D.300, the result becomes

$$\overline{D}_{xx}^{\text{eff}} = \frac{D}{a} \int_{-\frac{a}{2}}^{\frac{a}{2}} dy e^{-\beta\psi(y)} \quad (\text{D.307})$$

This expands to

$$\overline{D}_{xx}^{\text{eff}} = D e^{-\beta B} \frac{1}{a} \int_{-\frac{a}{2}}^{\frac{a}{2}} dy e^{-\beta A y^2} \quad (\text{D.308})$$

In this case, this is equivalent to

$$\overline{D}_{xx}^{\text{eff}} = D \frac{1}{|\Omega|} \int_{\Omega} d\Omega (e^{-\beta\psi}) \quad (\text{D.309})$$

However, this is not a general rule, as the next example will show.

Comparison of the results in Equation D.296 with those of Equation D.308 shows that the result of homogenization depends on the potential, even though the potential has no gradient in the direction of interest. In this case, the result for the effective diffusion coefficient could still be obtained by scaling by the spatial average of the exponential function of the potential. This, however, is not a general result.

The results of this problem are strikingly different for the case where the potential varies in the x -direction, $\psi(x, y) = \psi(x)$. In such a case, the steady-state Smoluchowski equation simplifies to

$$\frac{\partial^2 \bar{c}}{\partial x^2} - \beta \frac{\partial \psi}{\partial x} \frac{\partial \bar{c}}{\partial x} = 0 \quad (\text{D.310})$$

Each term contains at least one derivative of \bar{c} , and the boundary conditions allow \bar{c} to be constant with respect to y . Defining

$$f(x) = \frac{\partial \bar{c}}{\partial x} \quad (\text{D.311})$$

the steady-state Smoluchowski equation becomes the ordinary differential equation

$$\frac{df}{dx} - \beta \frac{d\psi}{dx} f = 0 \quad (\text{D.312})$$

The solution may be of the form

$$f = \frac{d\bar{c}}{dx} = K_1 e^{\beta\psi} \quad (\text{D.313})$$

where K_1 is a constant determined by the boundary conditions. For boundary conditions of constant \bar{c} at the left and right boundaries as indicated above, the solution is

$$K_1 = \frac{\bar{c}_R - \bar{c}_L}{\int_{-\frac{L}{2}}^{\frac{L}{2}} dx e^{\beta\psi}} \quad (\text{D.314})$$

This gives a flux of

$$j_x = -DK_1 \quad (\text{D.315})$$

and the resulting effective diffusion coefficient is

$$D_{xx}^{\text{eff}} = DK_1 \frac{L}{\Delta c} \quad (\text{D.316})$$

In particular, for the potential

$$\psi(x) = Ax^2 + B \quad (\text{D.317})$$

the boundary conditions are

$$\begin{aligned} \bar{c}_R &= c_R e^{\beta\psi(x=\frac{L}{2})} = c_R e^{\beta A \frac{L^2}{4}} e^{\beta B} \\ \bar{c}_L &= c_L e^{\beta\psi(x=-\frac{L}{2})} = c_L e^{\beta A \frac{L^2}{4}} e^{\beta B} \end{aligned} \quad (\text{D.318})$$

This gives a K_1 value of

$$K_1 = \frac{(c_R - c_L) e^{\beta A \frac{L^2}{4}} e^{\beta B}}{\int_{-\frac{L}{2}}^{\frac{L}{2}} dx e^{\beta A x^2} e^{\beta B}} \quad (\text{D.319})$$

Again, the large-scale gradient is based on the average of the concentration at the boundary, which may be inconsistent with the large-scale steady-state solution of the Smoluchowski equation. But with this assumption, the value of the effective diffusion coefficient is

$$D_{xx}^{\text{eff}} = D \frac{L e^{\beta A \frac{L^2}{4}} e^{\beta B}}{e^{\beta B} \int_{-\frac{L}{2}}^{\frac{L}{2}} dx e^{\beta A x^2}} = D \frac{L e^{\beta A \frac{L^2}{4}}}{\int_{-\frac{L}{2}}^{\frac{L}{2}} dx e^{\beta A x^2}} \quad (\text{D.320})$$

Note that this result does not depend on the value of B . Thus, a shift of the potential by a constant value would not affect this result.

For the homogenization approach, the relevant REV integral is

$$\bar{D}_{xx}^{\text{eff}} = \frac{D}{aL} \int_{-\frac{L}{2}}^{\frac{L}{2}} dx \int_{-\frac{a}{2}}^{\frac{a}{2}} dy e^{-\beta\psi(x)} (1 - \partial_x \chi_x) \quad (\text{D.321})$$

and the relevant corrector equation is

$$\partial_x (\bar{D} \partial_x \chi_x) + \partial_y (\bar{D} \partial_y \chi_x) = \partial_x \bar{D} \quad (\text{D.322})$$

where

$$\partial_x (\bar{D}) = D \partial_x e^{-\beta\psi} = -\beta D e^{-\beta\psi} \partial_x \psi = -\beta \bar{D} \partial_x \psi \quad (\text{D.323})$$

The relevant derivative of the potential is

$$\partial_x \psi = 2Ax \quad (\text{D.324})$$

Defining

$$f = \partial_x \chi_x \quad (\text{D.325})$$

and assuming χ_x varies only in the x -direction, the corrector problem becomes the ordinary differential equation

$$-\beta 2Ax f + \frac{df}{dx} = -\beta 2Ax \quad (\text{D.326})$$

The solution is

$$f = \partial_x \chi_x = 1 - G_1 e^{\beta Ax^2} \quad (\text{D.327})$$

where G_1 is a constant that can be obtained from the boundary conditions. Specifically, χ_x must be periodic. In this case, periodicity is enforced by requiring χ_x to be continuous across the unit cell boundaries.

$$\chi_x = \int dx \partial_x \chi_x = \int dx f \quad (\text{D.328})$$

$$\chi_x = x - G_1 \int dx e^{\beta Ax^2} + G_2 \quad (\text{D.329})$$

where G_2 is an arbitrary constant that will not affect the results. The values of χ_x at the right and left boundaries are

$$\chi_x \left(x = \frac{L}{2} \right) = \frac{L}{2} - G_1 \int dx e^{\beta Ax^2} \Big|_{\frac{L}{2}} + G_2 \quad (\text{D.330})$$

$$\chi_x \left(x = -\frac{L}{2} \right) = -\frac{L}{2} - G_1 \int dx e^{\beta Ax^2} \Big|_{-\frac{L}{2}} + G_2 \quad (\text{D.331})$$

The requirement of continuity at the boundary is

$$\chi_x \left(x = \frac{L}{2} \right) = \chi_x \left(x = -\frac{L}{2} \right) \quad (\text{D.332})$$

or, equivalently,

$$\chi_x \left(x = \frac{L}{2} \right) - \chi_x \left(x = -\frac{L}{2} \right) = 0 \quad (\text{D.333})$$

Substituting the expressions for χ_x at the boundaries into this equation gives

$$L - G_1 \int_{-\frac{L}{2}}^{\frac{L}{2}} dx e^{\beta Ax^2} = 0 \quad (\text{D.334})$$

And so, G_1 is thus obtained:

$$G_1 = \frac{L}{\int_{-\frac{L}{2}}^{\frac{L}{2}} dx e^{\beta Ax^2}} \quad (\text{D.335})$$

Substituting these results into the REV integral,

$$\overline{D}_{xx}^{\text{eff}} = \frac{D}{L} \int_{-\frac{L}{2}}^{\frac{L}{2}} dx e^{-\beta Ax^2} e^{-\beta B} (1 - f) \quad (\text{D.336})$$

$$\overline{D}_{xx}^{\text{eff}} = \frac{D}{L} e^{-\beta B} \int_{-\frac{L}{2}}^{\frac{L}{2}} dx e^{-\beta A x^2} G_1 e^{\beta A x^2} = \frac{D}{L} e^{-\beta B} G_1 L = D e^{-\beta B} G_1 \quad (\text{D.337})$$

And so the homogenized result is

$$\boxed{\overline{D}_{xx}^{\text{eff}} = D e^{-\beta B} \frac{L}{\int_{-\frac{L}{2}}^{\frac{L}{2}} dx e^{\beta A x^2}}} \quad (\text{D.338})$$

A summary of the results of the above analyses, normalized to D , is provided in Table D.1.

Table D.1: Results for the example Smoluchowski diffusion problem.

Potential	$\frac{D_{xx}^{\text{eff}}}{D}$ from flux calculation	$\frac{\overline{D}_{xx}^{\text{eff}}}{D}$ from homogenization	$\frac{\overline{D}_{xx}^{\text{eff}}}{D_{xx}^{\text{eff}}}$
$\psi = Ay^2 + B$	1	$e^{-\beta B} \frac{1}{a} \int_{-\frac{a}{2}}^{\frac{a}{2}} dy e^{-\beta Ay^2}$	$e^{-\beta B} \frac{1}{a} \int_{-\frac{a}{2}}^{\frac{a}{2}} dy e^{-\beta Ay^2}$
$\psi = Ax^2 + B$	$\frac{L e^{\beta A \frac{L^2}{4}}}{\int_{-\frac{L}{2}}^{\frac{L}{2}} dx e^{\beta A x^2}}$	$e^{-\beta B} \frac{L}{\int_{-\frac{L}{2}}^{\frac{L}{2}} dx e^{\beta A x^2}}$	$e^{-\beta B} e^{-\beta A \frac{L^2}{4}}$

Is it possible to obtain a general rule for converting $\overline{D}_{xx}^{\text{eff}}$ from homogenization to the value of D_{xx}^{eff} suitable for Fickian diffusion at the larger scale? The results of Table D.1 suggest that it might be possible. Specifically, assuming that the results are of the form

$$\overline{D}_{xx}^{\text{eff}} = D_{xx}^{\text{eff}} \Xi \quad (\text{D.339})$$

where Ξ is a Slotboom transformation factor for the larger scale as discussed in Section D.11, then there is an expression for Ξ that will give the correct results for both examples presented here. Of course, this does not prove that this expression is the general form of Ξ for all cases.

Specifically, the expression for Ξ that works in this example is an average over the unit cell boundary perpendicular to the corrector component in question:

$$\Xi = \frac{1}{|\Gamma_x|} \int_{\Gamma_x} d\Gamma e^{-\beta\psi} \quad (\text{D.340})$$

For this example problem, this is

$$\Xi = \frac{1}{a} \int_{-\frac{a}{2}}^{\frac{a}{2}} dy e^{-\beta\psi(x=\frac{L}{2},y)} \quad (\text{D.341})$$

Note that the potential must be periodic for this expression to be valid.

For the case of $\psi = \psi(y) = Ay^2 + B$, this becomes

$$\Xi = \frac{1}{a} \int_{-\frac{a}{2}}^{\frac{a}{2}} dy e^{-\beta Ay^2} e^{-\beta B} = e^{-\beta B} \frac{1}{a} \int_{-\frac{a}{2}}^{\frac{a}{2}} dy \quad (\text{D.342})$$

which is indeed the value required.

For the case of $\psi = \psi(x) = Ax^2 + B$, Ξ is

$$\Xi = \frac{1}{a} \int_{-\frac{a}{2}}^{\frac{a}{2}} dy e^{-\beta A \frac{L^2}{4}} e^{-\beta B} = e^{-\beta B} e^{-\beta A \frac{L^2}{4}} \quad (\text{D.343})$$

which is again exactly the value required to convert between $\overline{D}_{xx}^{\text{eff}}$ from homogenization and D_{xx}^{eff} from the flux calculation.

In summary, Equation D.340 correctly performs the Slotboom transformation, and its inverse, for the homogenized result in these example problems. While this is not conclusive proof that the expression is more generally valid, it justifies further investigation into this possibility. In particular, this example does not relate to situations where an off-diagonal term in the diffusion coefficient matrix is nonzero.

Note that in a situation where the potential is zero over the entire unit cell boundary, such as in the validation problem of Section 4.7, the resulting value of Ξ would be 1. In such a case, \overline{D} and D would be equivalent at the larger scale. The dependence of the homogenization result on shifts in the potential could therefore be interpreted as a gauge-dependence, where the homogenization result, without modification by Ξ , is D for cases where the gauge has been selected such that the potential is zero over the unit cell boundary. For cases where the potential varies over the boundary, Ξ would still be required.

As noted above, an alternative definition of the large-scale gradient for the flux-based calculation might give different results that are more compatible with both the large-scale Smoluchowski equation and the results of homogenization. This issue is still under investigation at the time of this writing.

References

- [1] Grégoire Allaire, Robert Brizzi, Jean-François Dufrêche, Andro Mikelić, and Andrey Piatnitski. “Ion transport in porous media: derivation of the macroscopic equations using upscaling and properties of the effective coefficients”. en. In: *Computational Geosciences* 17.3 (June 2013), pp. 479–495. ISSN: 1420-0597, 1573-1499. DOI: 10.1007/s10596-013-9342-6. URL: <http://link.springer.com/10.1007/s10596-013-9342-6> (visited on 03/11/2021).
- [2] Martin S. Alnæs, Jan Blechta, Johan Hake, August Johansson, Benjamin Kehlet, Anders Logg, Chris Richardson, Johannes Ring, Marie E. Rognes, and Garth N. Wells. “The FEniCS Project Version 1.5”. In: *Archive of Numerical Software* 3.100 (2015). DOI: 10.11588/ans.2015.100.20553.
- [3] A. Anantharaman, R. Costaouec, C. Le Bris, F. Legoll, and F. Thomines. “INTRODUCTION TO NUMERICAL STOCHASTIC HOMOGENIZATION AND THE RELATED COMPUTATIONAL CHALLENGES: SOME RECENT DEVELOPMENTS”. en. In: *Lecture Notes Series, Institute for Mathematical Sciences, National University of Singapore*. Vol. 22. WORLD SCIENTIFIC, Sept. 2011, pp. 197–272. ISBN: 978-981-4360-89-0 978-981-4360-90-6. DOI: 10.1142/9789814360906_0004. URL: http://www.worldscientific.com/doi/abs/10.1142/9789814360906_0004 (visited on 10/18/2018).
- [4] A. Anantharaman and C. Le Bris. “A Numerical Approach Related to Defect-Type Theories for Some Weakly Random Problems in Homogenization”. en. In: *Multiscale Modeling & Simulation* 9.2 (Apr. 2011), pp. 513–544. ISSN: 1540-3459, 1540-3467. DOI: 10.1137/10079639X. URL: <http://epubs.siam.org/doi/10.1137/10079639X> (visited on 10/18/2018).
- [5] Luca Antonioli, Pál Pacher, E. Sylvester Vizi, and György Haskó. “CD39 and CD73 in immunity and inflammation”. en. In: *Trends in Molecular Medicine* 19.6 (June 2013), pp. 355–367. ISSN: 14714914. DOI: 10.1016/j.molmed.2013.03.005. URL: <https://linkinghub.elsevier.com/retrieve/pii/S1471491413000543> (visited on 01/27/2021).
- [6] George B. Arfken, Hans-Jurgen Weber, and Frank E. Harris. *Mathematical methods for physicists: a comprehensive guide*. 7th ed. Amsterdam ; Boston: Elsevier, 2013. ISBN: 978-0-12-384654-9.
- [7] J.-L. Auriault, Claude Boutin, and Christian Geindreau. *Homogenization of coupled phenomena in heterogenous media*. eng. London, UK; Hoboken, N.J: ISTE; J. Wiley, 2009. ISBN: 978-1-84821-161-2.
- [8] H. D. Baehr and K. Stephan. *Heat and mass transfer*. eng. 3rd rev. ed. Berlin; New York: Springer, 2011. ISBN: 978-3-642-20020-5.

- [9] Radu Balescu. *V-langevin equations, continuous time random walks and fractional diffusion*. eng. Mémoire de la Classe des Sciences Collection in-8° Sér. 3, 29. OCLC: 254679096. Bruxelles: Académie royale de Belgique, 2008. ISBN: 978-2-8031-0246-4.
- [10] Charles W Bauschlicher, Stephen R Langhoff, and Peter R Taylor. “Accurate quantum chemical calculations”. In: *Advances in chemical physics* 77 (1990). Publisher: Wiley, New York, pp. 103–161.
- [11] Jacob Bear. *Dynamics of fluids in porous media*. Environmental science series (New York, 1972-). New York: American Elsevier Pub. Co, 1972. ISBN: 978-0-444-00114-6.
- [12] Alain Bensoussan, J.-L. Lions, and George Papanicolaou. *Asymptotic analysis for periodic structures*. Providence, R.I: American Mathematical Society, 2011. ISBN: 978-0-8218-5324-5.
- [13] Jeremy M. Berg, John L. Tymoczko, Lubert Stryer, and Lubert Stryer. *Biochemistry*. 5th ed. New York: W.H. Freeman, 2002. ISBN: 978-0-7167-3051-4.
- [14] Suresh K. Bhatia and David Nicholson. “Adsorption and Diffusion of Methane in Silica Nanopores: A Comparison of Single-Site and Five-Site Models”. en. In: *The Journal of Physical Chemistry C* 116.3 (Jan. 2012), pp. 2344–2355. ISSN: 1932-7447, 1932-7455. DOI: 10.1021/jp210593d. URL: <http://pubs.acs.org/doi/10.1021/jp210593d> (visited on 02/14/2019).
- [15] R. Byron Bird, Warren E. Stewart, and Edwin N. Lightfoot. *Transport phenomena*. 2nd, Wiley international ed. New York: J. Wiley, 2002. ISBN: 978-0-471-41077-5.
- [16] Robert Byron Bird, Warren E. Stewart, and Edwin N. Lightfoot. *Transport phenomena*. eng. OCLC: 964824. New York: Wiley, 1960. ISBN: 978-0-471-07392-5.
- [17] Haruhiko Bito. “The chemical biology of synapses and neuronal circuits”. en. In: *Nature Chemical Biology* 6.8 (Aug. 2010), pp. 560–563. ISSN: 1552-4450, 1552-4469. DOI: 10.1038/nchembio.408. URL: <http://www.nature.com/articles/nchembio.408> (visited on 01/27/2021).
- [18] Mary L. Boas. *Mathematical methods in the physical sciences*. 3rd ed. Hoboken, NJ: Wiley, 2006. ISBN: 978-0-471-19826-0 978-0-471-36580-8.
- [19] M.J.L. Bours, E.L.R. Swennen, F. Di Virgilio, B.N. Cronstein, and P.C. Dagnelie. “Adenosine 5'-triphosphate and adenosine as endogenous signaling molecules in immunity and inflammation”. en. In: *Pharmacology & Therapeutics* 112.2 (Nov. 2006), pp. 358–404. ISSN: 01637258. DOI: 10.1016/j.pharmthera.2005.04.013. URL: <https://linkinghub.elsevier.com/retrieve/pii/S0163725806000660> (visited on 01/27/2021).
- [20] B. H. Bransden and C. J. Joachain. *Physics of atoms and molecules*. 2nd ed. Harlow, England ; New York: Prentice Hall, 2003. ISBN: 978-0-582-35692-4.

- [21] Marcos Luciano Bruschi. *Strategies to modify the drug release from pharmaceutical systems*. 1st edition. Waltham, MA: Elsevier, 2015. ISBN: 978-0-08-100092-2.
- [22] Tai Bui, Anh Phan, David R. Cole, and Alberto Striolo. “Transport Mechanism of Guest Methane in Water-Filled Nanopores”. en. In: *The Journal of Physical Chemistry C* 121.29 (July 2017), pp. 15675–15686. ISSN: 1932-7447, 1932-7455. DOI: 10.1021/acs.jpcc.7b02713. URL: <https://pubs.acs.org/doi/10.1021/acs.jpcc.7b02713> (visited on 08/14/2020).
- [23] Geoffrey Burnstock. “Purinergic signalling: Purinergic signalling”. en. In: *British Journal of Pharmacology* 147.S1 (Jan. 2006), S172–S181. ISSN: 00071188. DOI: 10.1038/sj.bjp.0706429. URL: <http://doi.wiley.com/10.1038/sj.bjp.0706429> (visited on 01/27/2021).
- [24] Eugene Butkov. *Mathematical physics*. 32. print. Addison-Wesley series in advanced physics. OCLC: 258506311. Reading, Mass.: Addison-Wesley, 1995. ISBN: 978-0-201-00727-5.
- [25] M. Caffarel, D. M. Ceperley, and M. H. Kalos. “Comment on “Feynman-Kac path-integral calculation of the ground-state energies of atoms””. en. In: *Physical Review Letters* 71.13 (Sept. 1993), pp. 2159–2159. ISSN: 0031-9007. DOI: 10.1103/PhysRevLett.71.2159. URL: <https://link.aps.org/doi/10.1103/PhysRevLett.71.2159> (visited on 08/29/2020).
- [26] William D. Callister and David G. Rethwisch. *Materials science and engineering: an introduction*. 9th edition. Hoboken, NJ: Wiley, 2014. ISBN: 978-1-118-32457-8.
- [27] D. M. Ceperley. “Fermion nodes”. In: *Journal of Statistical Physics* 63.5 (June 1991), pp. 1237–1267. ISSN: 1572-9613. DOI: 10.1007/BF01030009. URL: <https://doi.org/10.1007/BF01030009>.
- [28] Steven C. Chapra and Raymond P. Canale. *Numerical methods for engineers: with programming and software applications*. 3rd ed. Boston: WCB/McGraw-Hill, 1998. ISBN: 978-0-07-010938-4.
- [29] Zhangxin Chen, Guanren Huan, and Yuanle Ma. *Computational methods for multiphase flows in porous media*. Computational science & engineering. OCLC: ocm62804700. Philadelphia: Society for Industrial and Applied Mathematics, 2006. ISBN: 978-0-89871-606-1.
- [30] Ronan Costaouec. “Asymptotic Expansion of the Homogenized Matrix in Two Weakly Stochastic Homogenization Settings”. en. In: *Applied Mathematics Research eXpress* 2012.1 (2012), pp. 76–104. ISSN: 1687-1197, 1687-1200. DOI: 10.1093/amrx/abr011. URL: <https://academic.oup.com/amrx/article-lookup/doi/10.1093/amrx/abr011> (visited on 10/09/2018).
- [31] National Science and Technology Council. *Materials Genome Initiative for Global Competitiveness*. 2011. URL: https://www.mgi.gov/sites/default/files/documents/materials_genome_initiative-final.pdf.

- [32] Frank A. Coutelieis and João M. P. Q. Delgado. *Transport processes in porous media*. en. Advanced structured materials v.20. OCLC: ocn769420091. Heidelberg ; New York: Springer, 2012. ISBN: 978-3-642-27909-6.
- [33] Christopher J. Cramer. *Essentials of computational chemistry: theories and models*. 2nd ed. Chichester, West Sussex, England ; Hoboken, NJ: Wiley, 2004. ISBN: 978-0-470-09182-1 978-0-470-09181-4.
- [34] John Crank. *The mathematics of diffusion*. 2d ed. Oxford, [Eng]: Clarendon Press, 1975. ISBN: 978-0-19-853344-3.
- [35] Stefano Curtarolo, Gus L. W. Hart, Marco Buongiorno Nardelli, Natalio Mingo, Stefano Sanvito, and Ohad Levy. “The high-throughput highway to computational materials design”. en. In: *Nature Materials* 12.3 (Mar. 2013), pp. 191–201. ISSN: 1476-1122, 1476-4660. DOI: 10.1038/nmat3568. URL: <http://www.nature.com/articles/nmat3568> (visited on 07/22/2020).
- [36] John H. Cushman, ed. *Dynamics of fluids in hierarchical porous media*. eng. OCLC: 21962757. London: Academic Press, 1990. ISBN: 978-0-12-200260-1.
- [37] Jan O. Daldrop, Bartosz G. Kowalik, and Roland R. Netz. “External Potential Modifies Friction of Molecular Solutes in Water”. en. In: *Physical Review X* 7.4 (Dec. 2017). ISSN: 2160-3308. DOI: 10.1103/PhysRevX.7.041065. URL: <https://link.aps.org/doi/10.1103/PhysRevX.7.041065> (visited on 04/18/2019).
- [38] S.R. De Groot. *Thermodynamics of Irreversible Processes*. Selected topics in modern physics, 3. North-HollandPub. Company, 1951.
- [39] Silvia Deaglio and Simon C. Robson. “Ectonucleotidases as Regulators of Purinergic Signaling in Thrombosis, Inflammation, and Immunity”. en. In: *Advances in Pharmacology*. Vol. 61. Elsevier, 2011, pp. 301–332. ISBN: 978-0-12-385526-8. DOI: 10.1016/B978-0-12-385526-8.00010-2. URL: <https://linkinghub.elsevier.com/retrieve/pii/B9780123855268000102> (visited on 01/26/2021).
- [40] G. H. F Diercksen, B. T Sutcliffe, and A Veillard. *Computational Techniques in Quantum Chemistry and Molecular Physics: Proceedings of the NATO Advanced Study Institute held at Ramsau, Germany, 4-21 September, 1974*. English. OCLC: 958526451. Dordrecht: Springer Netherlands, 1975. ISBN: 978-94-010-1815-9. URL: <https://doi.org/10.1007/978-94-010-1815-9> (visited on 08/25/2020).
- [41] Paul A. M. Dirac. “Quantum mechanics of many-electron systems”. en. In: *Proceedings of the Royal Society of London. Series A, Containing Papers of a Mathematical and Physical Character* 123.792 (Apr. 1929), pp. 714–733. ISSN: 0950-1207, 2053-9150. DOI: 10.1098/rspa.1929.0094. URL: <https://royalsocietypublishing.org/doi/10.1098/rspa.1929.0094> (visited on 12/23/2020).

- [42] R. John Ellis. “Macromolecular crowding: obvious but underappreciated”. en. In: *Trends in Biochemical Sciences* 26.10 (Oct. 2001), pp. 597–604. ISSN: 09680004. DOI: 10.1016/S0968-0004(01)01938-7. URL: <https://linkinghub.elsevier.com/retrieve/pii/S0968000401019387> (visited on 01/27/2021).
- [43] Fateme S. Emami, Valeria Puddu, Rajiv J. Berry, Vikas Varshney, Siddharth V. Patwardhan, Carole C. Perry, and Hendrik Heinz. “Force Field and a Surface Model Database for Silica to Simulate Interfacial Properties in Atomic Resolution”. en. In: *Chemistry of Materials* 26.8 (Apr. 2014), pp. 2647–2658. ISSN: 0897-4756, 1520-5002. DOI: 10.1021/cm500365c. URL: <http://pubs.acs.org/doi/10.1021/cm500365c> (visited on 02/28/2019).
- [44] Fateme S. Emami, Valeria Puddu, Rajiv J. Berry, Vikas Varshney, Siddharth V. Patwardhan, Carole C. Perry, and Hendrik Heinz. “Correction to Force Field and a Surface Model Database for Silica to Simulate Interfacial Properties in Atomic Resolution”. en. In: *Chemistry of Materials* 28.1 (Jan. 2016), pp. 406–407. ISSN: 0897-4756, 1520-5002. DOI: 10.1021/acs.chemmater.5b04760. URL: <https://pubs.acs.org/doi/10.1021/acs.chemmater.5b04760> (visited on 07/23/2020).
- [45] W. M. C. Foulkes. “Comment on “Feynman-Kac path-integral calculation of the ground-state energies of atoms””. en. In: *Physical Review Letters* 71.13 (Sept. 1993), pp. 2158–2158. ISSN: 0031-9007. DOI: 10.1103/PhysRevLett.71.2158. URL: <https://link.aps.org/doi/10.1103/PhysRevLett.71.2158> (visited on 08/29/2020).
- [46] W. M. C. Foulkes, L. Mitás, R. J. Needs, and G. Rajagopal. “Quantum Monte Carlo simulations of solids”. en. In: *Reviews of Modern Physics* 73.1 (Jan. 2001), pp. 33–83. ISSN: 0034-6861, 1539-0756. DOI: 10.1103/RevModPhys.73.33. URL: <https://link.aps.org/doi/10.1103/RevModPhys.73.33> (visited on 09/03/2020).
- [47] Daan Frenkel and Berend Smit. *Understanding molecular simulation: from algorithms to applications*. 2nd ed. Computational science series 1. San Diego: Academic Press, 2002. ISBN: 978-0-12-267351-1.
- [48] Christophe Geuzaine and Jean-François Remacle. “Gmsh: A 3-D finite element mesh generator with built-in pre- and post-processing facilities: THE GMSH PAPER”. en. In: *International Journal for Numerical Methods in Engineering* 79.11 (Sept. 2009), pp. 1309–1331. ISSN: 00295981. DOI: 10.1002/nme.2579. URL: <http://doi.wiley.com/10.1002/nme.2579> (visited on 12/19/2020).
- [49] Richard Gowers, Max Linke, Jonathan Barnoud, Tyler Reddy, Manuel Melo, Sean Seyler, Jan Domański, David Dotson, Sébastien Buchoux, Ian Kenney, and Oliver Beckstein. “MDAnalysis: A Python Package for the Rapid Analysis of Molecular Dynamics Simulations”. In: *Proceedings of the 15th Python in Science Conference*. SciPy, 2016. DOI: 10.25080/majora-629e541a-00e. URL: <https://doi.org/10.25080/majora-629e541a-00e>.

- [50] I. S. Gradshteyn, I. M. Ryzhik, and Alan Jeffrey. *Table of integrals, series, and products*. eng. 7th ed. Amsterdam ; Boston: Academic Press, 2007. ISBN: 978-0-12-373637-6.
- [51] David J. Griffiths. *Introduction to electrodynamics*. 3rd ed. Upper Saddle River, N.J: Prentice Hall, 1999. ISBN: 978-0-13-805326-0.
- [52] Alan Grossfield. *WHAM: an implementation of the weighted histogram analysis method, Version 2.0.10*. 2005. URL: <http://membrane.urmc.rochester.edu/content/wham/>.
- [53] Ceri Hammond, Nikolaos Dimitratos, Jose Antonio Lopez-Sanchez, Robert L. Jenkins, Gareth Whiting, Simon A. Kondrat, Mohd Hasbi ab Rahim, Michael M. Forde, Adam Thetford, Henk Hagen, Eric E. Stangland, Jacob M. Moulijn, Stuart H. Taylor, David J. Willock, and Graham J. Hutchings. “Aqueous-Phase Methane Oxidation over Fe-MFI Zeolites; Promotion through Isomorphous Framework Substitution”. en. In: *ACS Catalysis* 3.8 (Aug. 2013), pp. 1835–1844. ISSN: 2155-5435, 2155-5435. DOI: 10.1021/cs400288b. URL: <http://pubs.acs.org/doi/10.1021/cs400288b> (visited on 07/03/2018).
- [54] N. Hansen, R. Krishna, J. M. van Baten, A. T. Bell, and F. J. Keil. “Analysis of Diffusion Limitation in the Alkylation of Benzene over H-ZSM-5 by Combining Quantum Chemical Calculations, Molecular Simulations, and a Continuum Approach”. en. In: *The Journal of Physical Chemistry C* 113.1 (Jan. 2009), pp. 235–246. ISSN: 1932-7447, 1932-7455. DOI: 10.1021/jp8073046. URL: <https://pubs.acs.org/doi/10.1021/jp8073046> (visited on 02/25/2019).
- [55] Milton Edward Harr. *Groundwater and seepage*. English. OCLC: 489956. New York: McGraw-Hill, 1962. ISBN: 978-0-07-026740-4.
- [56] Z. Hashin and S. Shtrikman. “A variational approach to the theory of the elastic behaviour of multiphase materials”. en. In: *Journal of the Mechanics and Physics of Solids* 11.2 (Mar. 1963), pp. 127–140. ISSN: 00225096. DOI: 10.1016/0022-5096(63)90060-7. URL: <http://linkinghub.elsevier.com/retrieve/pii/0022509663900607> (visited on 11/01/2018).
- [57] Anthony L. Hines and Robert N. Maddox. *Mass transfer: fundamentals and applications*. Prentice-Hall international series in the physical and chemical engineering sciences. Englewood Cliffs, N.J: Prentice-Hall, 1985. ISBN: 978-0-13-559609-8.
- [58] P. Hohenberg and W. Kohn. “Inhomogeneous Electron Gas”. en. In: *Physical Review* 136.3B (Nov. 1964), B864–B871. ISSN: 0031-899X. DOI: 10.1103/PhysRev.136.B864. URL: <https://link.aps.org/doi/10.1103/PhysRev.136.B864> (visited on 05/07/2020).
- [59] M. F. Horstemeyer. “Multiscale Modeling: A Review”. en. In: *Practical Aspects of Computational Chemistry*. Ed. by Jerzy Leszczynski and Manoj K. Shukla. Dordrecht: Springer Netherlands, 2009, pp. 87–135. ISBN: 978-90-481-2686-6 978-90-481-2687-3. DOI: 10.1007/978-90-481-2687-3_4. URL: <http://>

//link.springer.com/10.1007/978-90-481-2687-3_4 (visited on 07/22/2020).

- [60] Thomas J. R. Hughes. *The finite element method: linear static and dynamic finite element analysis*. Englewood Cliffs, N.J: Prentice-Hall, 1987. ISBN: 978-0-13-317025-2.
- [61] Gerhard Hummer. “Position-dependent diffusion coefficients and free energies from Bayesian analysis of equilibrium and replica molecular dynamics simulations”. en. In: *New Journal of Physics* 7 (Feb. 2005), pp. 34–34. ISSN: 1367-2630. DOI: 10.1088/1367-2630/7/1/034. URL: <https://iopscience.iop.org/article/10.1088/1367-2630/7/1/034> (visited on 07/02/2020).
- [62] R. Iftimie, P. Minari, and M. E. Tuckerman. “Ab initio molecular dynamics: Concepts, recent developments, and future trends”. en. In: *Proceedings of the National Academy of Sciences* 102.19 (May 2005), pp. 6654–6659. ISSN: 0027-8424, 1091-6490. DOI: 10.1073/pnas.0500193102. URL: <http://www.pnas.org/cgi/doi/10.1073/pnas.0500193102> (visited on 12/15/2020).
- [63] Frank P. Incropera and David P. DeWitt. *Fundamentals of heat and mass transfer*. 3rd ed. New York: Wiley, 1990. ISBN: 978-0-471-61246-9.
- [64] Jacob N. Israelachvili. *Intermolecular and surface forces*. 3rd ed. OCLC: ocn656213150. Burlington, MA: Academic Press, 2011. ISBN: 978-0-12-375182-9 978-0-08-092363-5.
- [65] John David Jackson. *Classical electrodynamics*. 3rd ed. New York: Wiley, 1999. ISBN: 978-0-471-30932-1.
- [66] William L. Jorgensen, Jeffrey D. Madura, and Carol J. Swenson. “Optimized intermolecular potential functions for liquid hydrocarbons”. en. In: *Journal of the American Chemical Society* 106.22 (Oct. 1984), pp. 6638–6646. ISSN: 0002-7863. DOI: 10.1021/ja00334a030. URL: <https://pubs.acs.org/doi/abs/10.1021/ja00334a030> (visited on 12/15/2020).
- [67] Johannes Kästner. “Umbrella sampling: Umbrella sampling”. en. In: *Wiley Interdisciplinary Reviews: Computational Molecular Science* 1.6 (Nov. 2011), pp. 932–942. ISSN: 17590876. DOI: 10.1002/wcms.66. URL: <http://doi.wiley.com/10.1002/wcms.66> (visited on 11/06/2020).
- [68] P M Keken-Huskey, A Gillette, J Hake, and J A McCammon. “Finite-element estimation of protein–ligand association rates with post-encounter effects: applications to calcium binding in troponin C and SERCA”. en. In: *Computational Science & Discovery* 5.1 (Oct. 2012), p. 014015. ISSN: 1749-4699. DOI: 10.1088/1749-4699/5/1/014015. URL: <http://stacks.iop.org/1749-4699/5/i=1/a=014015?key=crossref.6390c16cb178274c9f5dc828effcfb42> (visited on 03/02/2020).

- [69] P. M. Kekenés-Huskey, A. K. Gillette, and J. A. McCammon. “Predicting the influence of long-range molecular interactions on macroscopic-scale diffusion by homogenization of the Smoluchowski equation”. en. In: *The Journal of Chemical Physics* 140.17 (May 2014), p. 174106. ISSN: 0021-9606, 1089-7690. DOI: 10.1063/1.4873382. URL: <http://aip.scitation.org/doi/10.1063/1.4873382> (visited on 03/13/2018).
- [70] Peter M. Kekenés-Huskey, Tao Liao, Andrew K. Gillette, Johan E. Hake, Yongjie Zhang, Anushka P. Michailova, Andrew D. McCulloch, and J. Andrew McCammon. “Molecular and Subcellular-Scale Modeling of Nucleotide Diffusion in the Cardiac Myofilament Lattice”. en. In: *Biophysical Journal* 105.9 (Nov. 2013), pp. 2130–2140. ISSN: 00063495. DOI: 10.1016/j.bpj.2013.09.020. URL: <http://linkinghub.elsevier.com/retrieve/pii/S0006349513010680> (visited on 03/13/2018).
- [71] Peter M. Kekenés-Huskey, Caitlin E. Scott, and Selcuk Atalay. “Quantifying the Influence of the Crowded Cytoplasm on Small Molecule Diffusion”. en. In: *The Journal of Physical Chemistry B* 120.33 (Aug. 2016), pp. 8696–8706. ISSN: 1520-6106, 1520-5207. DOI: 10.1021/acs.jpcc.6b03887. URL: <http://pubs.acs.org/doi/10.1021/acs.jpcc.6b03887> (visited on 05/02/2019).
- [72] David E Keyes, Lois C McInnes, Carol Woodward, William Gropp, Eric Myra, Michael Pernice, John Bell, Jed Brown, Alain Clo, Jeffrey Connors, Emil Constantinescu, Don Estep, Kate Evans, Charbel Farhat, Ammar Hakim, Glenn Hammond, Glen Hansen, Judith Hill, Tobin Isaac, Xiangmin Jiao, Kirk Jordan, Dinesh Kaushik, Efthimios Kaxiras, Alice Koniges, Kihwan Lee, Aaron Lott, Qiming Lu, John Magerlein, Reed Maxwell, Michael McCourt, Miriam Mehl, Roger Pawlowski, Amanda P Randles, Daniel Reynolds, Beatrice Rivière, Ulrich Rüde, Tim Scheibe, John Shadid, Brendan Sheehan, Mark Shephard, Andrew Siegel, Barry Smith, Xianzhu Tang, Cian Wilson, and Barbara Wohlmuth. “Multiphysics simulations: Challenges and opportunities”. en. In: *The International Journal of High Performance Computing Applications* 27.1 (Feb. 2013), pp. 4–83. ISSN: 1094-3420, 1741-2846. DOI: 10.1177/1094342012468181. URL: <http://journals.sagepub.com/doi/10.1177/1094342012468181> (visited on 04/02/2020).
- [73] Fadoua Khmaïssia, Hichem Frigui, Mahendra Sunkara, Jacek Jasinski, Alejandro Martinez Garcia, Tom Pace, and Madhu Menon. “Accelerating band gap prediction for solar materials using feature selection and regression techniques”. en. In: *Computational Materials Science* 147 (May 2018), pp. 304–315. ISSN: 09270256. DOI: 10.1016/j.commatsci.2018.02.012. URL: <https://linkinghub.elsevier.com/retrieve/pii/S0927025618300958> (visited on 04/14/2020).
- [74] Cheol Woong Kim, Nam Ho Heo, and Karl Seff. “Framework Sites Preferred by Aluminum in Zeolite ZSM-5. Structure of a Fully Dehydrated, Fully Cs+-Exchanged ZSM-5 Crystal (MFI, Si/Al = 24)”. In: *The Journal of Physical Chemistry C* 115.50 (Dec. 2011). Publisher: American Chemical Society,

- pp. 24823–24838. ISSN: 1932-7447. DOI: 10.1021/jp208246q. URL: <https://doi.org/10.1021/jp208246q>.
- [75] Hyungjun Kim. *Multiscale and multiphysics computational frameworks for nano- and bio-systems*. Springer theses: recognizing outstanding Ph.D. research. New York: Springer, 2011. ISBN: 978-1-4419-7600-0 978-1-4419-7601-7.
- [76] W. Kohn and L. J. Sham. “Self-Consistent Equations Including Exchange and Correlation Effects”. en. In: *Physical Review* 140.4A (Nov. 1965), A1133–A1138. ISSN: 0031-899X. DOI: 10.1103/PhysRev.140.A1133. URL: <https://link.aps.org/doi/10.1103/PhysRev.140.A1133> (visited on 05/07/2020).
- [77] A. Korzeniowski, J. L. Fry, D. E. Orr, and N. G. Fazleev. “Korzeniowski et al. reply”. en. In: *Physical Review Letters* 71.13 (Sept. 1993), pp. 2160–2161. ISSN: 0031-9007. DOI: 10.1103/PhysRevLett.71.2160. URL: <https://link.aps.org/doi/10.1103/PhysRevLett.71.2160> (visited on 08/29/2020).
- [78] Filip Kukulski, Sébastien A. Lévesque, and Jean Sévigny. “Impact of Ectoenzymes on P2 and P1 Receptor Signaling”. en. In: *Advances in Pharmacology*. Vol. 61. Elsevier, 2011, pp. 263–299. ISBN: 978-0-12-385526-8. DOI: 10.1016/B978-0-12-385526-8.00009-6. URL: <https://linkinghub.elsevier.com/retrieve/pii/B9780123855268000096> (visited on 01/27/2021).
- [79] Shankar Kumar, John M. Rosenberg, Djamal Bouzida, Robert H. Swendsen, and Peter A. Kollman. “THE weighted histogram analysis method for free-energy calculations on biomolecules. I. The method”. en. In: *Journal of Computational Chemistry* 13.8 (Oct. 1992), pp. 1011–1021. ISSN: 0192-8651, 1096-987X. DOI: 10.1002/jcc.540130812. URL: <http://doi.wiley.com/10.1002/jcc.540130812> (visited on 11/05/2020).
- [80] Shankar Kumar, John M. Rosenberg, Djamal Bouzida, Robert H. Swendsen, and Peter A. Kollman. “Multidimensional free-energy calculations using the weighted histogram analysis method”. en. In: *Journal of Computational Chemistry* 16.11 (Nov. 1995), pp. 1339–1350. ISSN: 0192-8651, 1096-987X. DOI: 10.1002/jcc.540161104. URL: <http://doi.wiley.com/10.1002/jcc.540161104> (visited on 11/05/2020).
- [81] Chris Lee, Jbmoody, and Michael Holst. *ctlee/gamer: Release v2.0.1-beta*. Feb. 2019. DOI: 10.5281/zenodo.2563425. URL: <https://zenodo.org/record/2563425> (visited on 03/18/2019).
- [82] Christopher T Lee, Justin G. Laughlin, Nils Angliviel de La Beaumelle, Rommie Amaro, J. Andrew McCammon, Ravi Ramamoorthi, Michael J. Holst, and Padmini Rangamani. “GAMer 2: A System for 3D Mesh Processing of Cellular Electron Micrographs: Supplemental Movie 1”. In: *bioRxiv* (Jan. 2019). DOI: 10.1101/534479. URL: <http://biorxiv.org/lookup/doi/10.1101/534479> (visited on 03/18/2019).
- [83] Louis Leithold. *The calculus of a single variable with analytic geometry*. 6th ed. New York: Harper & Row, 1990. ISBN: 978-0-06-044107-4 978-0-06-043930-9.

- [84] Anders Logg, Garth N. Wells, and Johan Hake. “DOLFIN: a C++/Python Finite Element Library”. In: *Automated Solution of Differential Equations by the Finite Element Method, Volume 84 of Lecture Notes in Computational Science and Engineering*. Ed. by Anders Logg, Kent-Andre Mardal, and Garth N. Wells. Springer, 2012. Chap. 10.
- [85] Benzhuo Lu, Michael J. Holst, J. Andrew McCammon, and Y.C. Zhou. “Poisson–Nernst–Planck equations for simulating biomolecular diffusion–reaction processes I: Finite element solutions”. en. In: *Journal of Computational Physics* 229.19 (Sept. 2010), pp. 6979–6994. ISSN: 00219991. DOI: 10.1016/j.jcp.2010.05.035. URL: <https://linkinghub.elsevier.com/retrieve/pii/S0021999110002962> (visited on 02/21/2019).
- [86] Reinoud Maex. “Nernst-Planck Equation”. en. In: *Encyclopedia of Computational Neuroscience*. Ed. by Dieter Jaeger and Ranu Jung. New York, NY: Springer New York, 2014, pp. 1–7. ISBN: 978-1-4614-7320-6. DOI: 10.1007/978-1-4614-7320-6_233-1. URL: http://link.springer.com/10.1007/978-1-4614-7320-6_233-1 (visited on 01/21/2020).
- [87] Donald A. McQuarrie. *Statistical mechanics*. Harper’s chemistry series. New York: Harper & Row, 1975. ISBN: 978-0-06-044366-5.
- [88] Donald A. McQuarrie and John D. Simon. *Physical chemistry: a molecular approach*. Sausalito, Calif: University Science Books, 1997. ISBN: 978-0-935702-99-6.
- [89] Nicholas Metropolis, Arianna W Rosenbluth, Marshall N Rosenbluth, Augusta H Teller, and Edward Teller. “Equation of State Calculations by Fast Computing Machines”. en. In: (1953), p. 7.
- [90] Naveen Michaud-Agrawal, Elizabeth J. Denning, Thomas B. Woolf, and Oliver Beckstein. “MDAnalysis: A toolkit for the analysis of molecular dynamics simulations”. In: *Journal of Computational Chemistry* 32.10 (Apr. 2011). Publisher: Wiley, pp. 2319–2327. DOI: 10.1002/jcc.21787. URL: <https://doi.org/10.1002/jcc.21787>.
- [91] Hendrik J. Monkhorst. “Chemical physics without the Born-Oppenheimer approximation: The molecular coupled-cluster method”. en. In: *Physical Review A* 36.4 (Aug. 1987), pp. 1544–1561. ISSN: 0556-2791. DOI: 10.1103/PhysRevA.36.1544. URL: <https://link.aps.org/doi/10.1103/PhysRevA.36.1544> (visited on 08/25/2020).
- [92] Michael J. Moran and Howard N. Shapiro. *Fundamentals of engineering thermodynamics*. 3rd ed. New York: Wiley, 1995. ISBN: 978-0-471-07681-0.
- [93] James C. Nearing. *Mathematical tools for physics*. Dover ed. Dover books on mathematics. Mineola, N.Y: Dover Publications, 2010. ISBN: 978-0-486-47772-5 978-0-486-48212-5.

- [94] Chris Oostenbrink, Alessandra Villa, Alan E. Mark, and Wilfred F. Van Gunsteren. “A biomolecular force field based on the free enthalpy of hydration and solvation: The GROMOS force-field parameter sets 53A5 and 53A6”. en. In: *Journal of Computational Chemistry* 25.13 (Oct. 2004), pp. 1656–1676. ISSN: 0192-8651, 1096-987X. DOI: 10.1002/jcc.20090. URL: <http://doi.wiley.com/10.1002/jcc.20090> (visited on 11/05/2020).
- [95] Irving Ozier. “Ground-State Electric Dipole Moment of Methane”. en. In: *Physical Review Letters* 27.20 (Nov. 1971), pp. 1329–1332. ISSN: 0031-9007. DOI: 10.1103/PhysRevLett.27.1329. URL: <https://link.aps.org/doi/10.1103/PhysRevLett.27.1329> (visited on 11/06/2020).
- [96] Thomas G. Pace, David J. Bentler, and Gregory A. Yankey. “Practical Considerations for Frequency-Dependent Issues in the Explicit Dynamic Analysis of Clearwater Dam”. en. In: *Embankments, Dams, and Slopes*. Denver, Colorado, United States: American Society of Civil Engineers, Oct. 2007, pp. 1–10. ISBN: 978-0-7844-0905-3. DOI: 10.1061/40905(224)3. URL: <http://ascelibrary.org/doi/abs/10.1061/40905%28224%293> (visited on 07/11/2020).
- [97] Sanghyun Park, Fatemeh Khalili-Araghi, Emad Tajkhorshid, and Klaus Schulten. “Free energy calculation from steered molecular dynamics simulations using Jarzynski’s equality”. en. In: *The Journal of Chemical Physics* 119.6 (Aug. 2003), pp. 3559–3566. ISSN: 0021-9606, 1089-7690. DOI: 10.1063/1.1590311. URL: <http://aip.scitation.org/doi/10.1063/1.1590311> (visited on 11/06/2020).
- [98] R. K. Pathria and Paul D. Beale. *Statistical mechanics*. 3rd ed. Amsterdam ; Boston: Elsevier/Academic Press, 2011. ISBN: 978-0-12-382188-1.
- [99] Andrzej Pękalski and Katarzyna Sznajd-Weron, eds. *Anomalous diffusion: from basics to applications: proceedings of the XIth Max Born Symposium held at Ladek Zdroj, Poland, 20-27 May, 1998*. Lecture notes in physics v. 519. Meeting Name: Max Born Symposium. Berlin ; New York: Springer, 1999. ISBN: 978-3-540-65416-2.
- [100] John P. Perdew and Adrienn Ruzsinszky. “Fourteen easy lessons in density functional theory”. en. In: *International Journal of Quantum Chemistry* 110.15 (Aug. 2010), pp. 2801–2807. ISSN: 00207608. DOI: 10.1002/qua.22829. URL: <http://doi.wiley.com/10.1002/qua.22829> (visited on 04/09/2020).
- [101] George Pólya and John Horton Conway. *How to solve it: a new aspect of mathematical method*. Expanded Princeton Science Library ed. Princeton science library. OCLC: ocm55008123. Princeton [N.J.]: Princeton University Press, 2004. ISBN: 978-0-691-11966-3.
- [102] John A. Pople. “Nobel Lecture: Quantum chemical models”. en. In: *Reviews of Modern Physics* 71.5 (Oct. 1999), pp. 1267–1274. ISSN: 0034-6861, 1539-0756. DOI: 10.1103/RevModPhys.71.1267. URL: <https://link.aps.org/doi/10.1103/RevModPhys.71.1267> (visited on 08/28/2020).

- [103] Dierk Raabe, Matthias Scheffler, Kurt Kremer, Walter Thiel, Jörg Neugebauer, and Martin Jansen. *Multi-Scale Modeling in Materials Science and Engineering*. URL: <https://www.mpg.de/967642/CPT01MultiScaleModelbasetext.pdf>.
- [104] Hadi Rahmaninejad, Tom Pace, Shashank Bhatt, Bin Sun, and Peter Kekeneshuskey. “Co-localization and confinement of ecto-nucleotidases modulate extracellular adenosine nucleotide distributions”. en. In: *PLOS Computational Biology* 16.6 (June 2020). Ed. by James M. Briggs, e1007903. ISSN: 1553-7358. DOI: 10.1371/journal.pcbi.1007903. URL: <https://dx.plos.org/10.1371/journal.pcbi.1007903> (visited on 07/02/2020).
- [105] A.F. Rauch, T.G. Pace, G. Yankey, J.S. Dingrando, and J.A. Schaefer. “Liquefaction under dams and levees: Back-of-the-envelope predictions of deformation”. In: *Association of State Dam Safety Officials - Dam Safety 2007* (2007).
- [106] Alan F. Rauch, Steve Artman, John C. Kammeyer, Bruce J. Haas, Jeffrey Barrett, Tom Pace, P. Bradford Smiley, Michael J. Steele, and Yong Wu. “Cement-Bentonite Slurry Walls for Seismic Containment of the Kingston Coal Ash Landfill”. en. In: *Grouting 2017*. Honolulu, Hawaii: American Society of Civil Engineers, July 2017, pp. 216–226. ISBN: 978-0-7844-8080-9. DOI: 10.1061/9780784480809.022. URL: <http://ascelibrary.org/doi/10.1061/9780784480809.022> (visited on 07/11/2020).
- [107] J. N. Reddy. *An introduction to the finite element method*. 2nd ed. McGraw-Hill series in mechanical engineering. New York: McGraw-Hill, 1993. ISBN: 978-0-07-051355-6.
- [108] Frederick Reif. *Fundamentals of statistical and thermal physics*. eng. reiss. OCLC: 845506926. Long Grove, Ill: Waveland Press, 2009. ISBN: 978-1-57766-612-7.
- [109] Steven Rifai, Robert Ferencz, Wen-Ping Wang, Evangelos Spyropoulos, Charles Lawrence, and Matthew Melis. “The role of multiphysics simulation in multidisciplinary analysis”. In: *7th AIAA/USAF/NASA/ISSMO Symposium on Multidisciplinary Analysis and Optimization*. 1998, p. 4863.
- [110] Germán Rivas and Allen P. Minton. “Macromolecular Crowding In Vitro , In Vivo , and In Between”. en. In: *Trends in Biochemical Sciences* 41.11 (Nov. 2016), pp. 970–981. ISSN: 09680004. DOI: 10.1016/j.tibs.2016.08.013. URL: <https://linkinghub.elsevier.com/retrieve/pii/S096800041630130X> (visited on 01/27/2021).
- [111] Harry E. Robson, ed. *Verified syntheses of zeolitic materials*. 2nd rev. ed. Amsterdam ; New York: Elsevier, 2001. ISBN: 978-0-444-50703-7.
- [112] Benoît Roux. “The calculation of the potential of mean force using computer simulations”. en. In: *Computer Physics Communications* 91.1-3 (Sept. 1995), pp. 275–282. ISSN: 00104655. DOI: 10.1016/0010-4655(95)00053-I. URL: <https://linkinghub.elsevier.com/retrieve/pii/001046559500053I> (visited on 11/05/2020).

- [113] Adrienn Ruzsinszky and John P. Perdew. “Twelve outstanding problems in ground-state density functional theory: A bouquet of puzzles”. en. In: *Computational and Theoretical Chemistry* 963.1 (Jan. 2011), pp. 2–6. ISSN: 2210271X. DOI: 10.1016/j.comptc.2010.09.002. URL: <https://linkinghub.elsevier.com/retrieve/pii/S2210271X10006092> (visited on 04/09/2020).
- [114] J. J. Sakurai and Jim Napolitano. *Modern quantum mechanics*. 2nd ed. Boston: Addison-Wesley, 2011. ISBN: 978-0-8053-8291-4.
- [115] Bernhard A Schrefler, Lorenzo Sanavia, and Frédéric Collin. “Coupled and multiphysics phenomena”. In: (2015). Publisher: ALERT Geomaterials.
- [116] Klaus Schulten and Ioan Kosztin. “Lectures in Theoretical Biophysics”. University of Illinois at Urbana-Champaign, 2000. URL: <http://www.ks.uiuc.edu/Services/Class/NSM.pdf>.
- [117] Thomas P Senftle, Sungwook Hong, Md Mahbubul Islam, Sudhir B Kylasa, Yuanxia Zheng, Yun Kyung Shin, Chad Junkermeier, Roman Engel-Herbert, Michael J Janik, Hasan Metin Aktulga, Toon Verstraelen, Ananth Grama, and Adri C T van Duin. “The ReaxFF reactive force-field: development, applications and future directions”. en. In: *npj Computational Materials* 2.1 (Nov. 2016), p. 15011. ISSN: 2057-3960. DOI: 10.1038/npjcompumats.2015.11. URL: <http://www.nature.com/articles/npjcompumats201511> (visited on 02/25/2021).
- [118] Piotr Setny, Riccardo Baron, Peter Michael Kekenes-Huskey, J. Andrew McCammon, and Joachim Dzubiella. “Solvent fluctuations in hydrophobic cavity–ligand binding kinetics”. en. In: *Proceedings of the National Academy of Sciences* 110.4 (Jan. 2013), pp. 1197–1202. ISSN: 0027-8424, 1091-6490. DOI: 10.1073/pnas.1221231110. URL: <http://www.pnas.org/lookup/doi/10.1073/pnas.1221231110> (visited on 02/28/2019).
- [119] Ramamurti Shankar. *Principles of quantum mechanics*. 2nd ed. New York: Plenum Press, 1994. ISBN: 978-0-306-44790-7.
- [120] Paul G. Shewmon. *Diffusion in solids*. McGraw-Hill series in materials science and engineering. New York: McGraw-Hill, 1963.
- [121] David J. Singh and Lars Nordström. *Planewaves, pseudopotentials, and the LAPW method*. 2nd ed. New York, NY: Springer, 2006. ISBN: 978-0-387-28780-5 978-0-387-29684-5.
- [122] J.W. Slotboom. “Computer-aided two-dimensional analysis of bipolar transistors”. en. In: *IEEE Transactions on Electron Devices* 20.8 (Aug. 1973), pp. 669–679. ISSN: 0018-9383. DOI: 10.1109/T-ED.1973.17727. URL: <http://ieeexplore.ieee.org/document/1477384/> (visited on 05/09/2019).

- [123] Yuhua Song, Yongjie Zhang, Tongye Shen, Chandrajit L. Bajaj, J. Andrew McCammon, and Nathan A. Baker. “Finite Element Solution of the Steady-State Smoluchowski Equation for Rate Constant Calculations”. en. In: *Bio-physical Journal* 86.4 (Apr. 2004), pp. 2017–2029. ISSN: 00063495. DOI: 10.1016/S0006-3495(04)74263-0. URL: <http://linkinghub.elsevier.com/retrieve/pii/S0006349504742630> (visited on 12/11/2018).
- [124] Attila Szabo and Neil S. Ostlund. *Modern quantum chemistry: introduction to advanced electronic structure theory*. Mineola, N.Y: Dover Publications, 1996. ISBN: 978-0-486-69186-2.
- [125] Ross Taylor and R. Krishna. *Multicomponent mass transfer*. Wiley series in chemical engineering. New York: Wiley, 1993. ISBN: 978-0-471-57417-0.
- [126] Norm M. Tubman, Ilkka Kylänpää, Sharon Hammes-Schiffer, and David M. Ceperley. “Beyond the Born-Oppenheimer approximation with quantum Monte Carlo methods”. In: *Phys. Rev. A* 90.4 (Oct. 2014). Publisher: American Physical Society, p. 042507. DOI: 10.1103/PhysRevA.90.042507. URL: <https://link.aps.org/doi/10.1103/PhysRevA.90.042507>.
- [127] Yoshitaka Umeno, Takahiro Shimada, Yusuke Kinoshita, and Takayuki Kitamura. *Multiphysics in nanostructures*. eng. Nanostructure Science and Technology. Tokyo: Springer, 2017. ISBN: 978-4-431-56573-4 978-4-431-56571-0.
- [128] Stefan Van Der Walt, S Chris Colbert, and Gael Varoquaux. “The NumPy array: a structure for efficient numerical computation”. In: *Computing in Science & Engineering* 13.2 (2011). Publisher: AIP Publishing, pp. 22–30. DOI: 10.1109/MCSE.2011.37.
- [129] S. Whitaker. “The equations of motion in porous media”. en. In: *Chemical Engineering Science* 21.3 (Mar. 1966), pp. 291–300. ISSN: 00092509. DOI: 10.1016/0009-2509(66)85020-0. URL: <https://linkinghub.elsevier.com/retrieve/pii/0009250966850200> (visited on 05/15/2020).
- [130] James Daniel Whitfield, Peter John Love, and Alán Aspuru-Guzik. “Computational complexity in electronic structure”. en. In: *Phys. Chem. Chem. Phys.* 15.2 (2013), pp. 397–411. ISSN: 1463-9076, 1463-9084. DOI: 10.1039/C2CP42695A. URL: <http://xlink.rsc.org/?DOI=C2CP42695A> (visited on 08/28/2020).
- [131] L T Wille and J Vennik. “Computational complexity of the ground-state determination of atomic clusters”. en. In: *Journal of Physics A: Mathematical and General* 18.8 (June 1985), pp. L419–L422. ISSN: 0305-4470, 1361-6447. DOI: 10.1088/0305-4470/18/8/003. URL: <https://iopscience.iop.org/article/10.1088/0305-4470/18/8/003> (visited on 08/28/2020).
- [132] P. A. Witherspoon and D. N. Saraf. “Diffusion of Methane, Ethane, Propane, and n-Butane in Water from 25 to 43°”. en. In: *The Journal of Physical Chemistry* 69.11 (Nov. 1965), pp. 3752–3755. ISSN: 0022-3654, 1541-5740. DOI: 10.1021/j100895a017. URL: <https://pubs.acs.org/doi/abs/10.1021/j100895a017> (visited on 08/12/2020).

- [133] Thomas B. Woolf and Benoit Roux. “Conformational Flexibility of o-Phosphorylcholine and o-Phosphorylethanolamine: A Molecular Dynamics Study of Solvation Effects”. en. In: *Journal of the American Chemical Society* 116.13 (June 1994), pp. 5916–5926. ISSN: 0002-7863. DOI: 10.1021/ja00092a048. URL: <http://pubs.acs.org/doi/abs/10.1021/ja00092a048> (visited on 04/18/2019).
- [134] Vasilii Vasil’evich Zhikov, S. M. Kozlov, and O. A. Oleinik. *Homogenization of differential operators and integral functionals*. eng. Berlin ; New York: Springer-Verlag, 1994. ISBN: 978-3-540-54809-6 978-0-387-54809-8.
- [135] Wouter Zijl. “The symmetry approximation for nonsymmetric permeability tensors and its consequences for mass transport”. en. In: *Transport in Porous Media* 22.2 (Feb. 1996), pp. 121–136. ISSN: 0169-3913, 1573-1634. DOI: 10.1007/BF01143511. URL: <http://link.springer.com/10.1007/BF01143511> (visited on 09/25/2020).
- [136] R. Zwanzig. “Diffusion in a rough potential.” en. In: *Proceedings of the National Academy of Sciences* 85.7 (Apr. 1988), pp. 2029–2030. ISSN: 0027-8424, 1091-6490. DOI: 10.1073/pnas.85.7.2029. URL: <http://www.pnas.org/cgi/doi/10.1073/pnas.85.7.2029> (visited on 08/17/2020).

Vita

THOMAS G. PACE, P.E.

Education

1. M.S., Physics – University of Kentucky, May 2020
2. M.S., Civil Engineering – Purdue University, May 2001
3. B.S., Civil Engineering – Purdue University, December 1999

Professional Experience

1. Laboratory of Dr. Peter M. Kekenos-Huskey (Lexington, Kentucky)
 - Research Specialist: (Loyola University Chicago) August 2019 – Present
 - Graduate Research Assistant: (University of Kentucky) July 2017 – August 2019
2. Stantec (Lexington, Kentucky, formerly FMSM Engineers, Inc.)
 - Senior Project Engineer: July 2005 – Present
 - Project Engineer: May 2001 – July 2005
 - Intern: May 1999 – August 1999, May 2000 – August 2000
3. Purdue University (West Lafayette, Indiana)
 - Graduate Teaching Assistant: Spring 2000, Fall 2000, and Spring 2001
4. Kentucky Transportation Center (Lexington, Kentucky)
 - Laboratory Technician: June 1996 – August 1996, June 1997

Publications

1. Fadoua Khmaissia, Hichem Frigui, Mahendra Sunkara, Jacek Jasinski, Alejandro Martinez Garcia, Tom Pace, and Madhu Menon. “Accelerating band gap prediction for solar materials using feature selection and regression techniques”. en. In: *Computational Materials Science* 147 (May 2018), pp. 304–315. ISSN: 09270256. DOI: 10.1016/j.commatsci.2018.02.012. URL: <https://linkinghub.elsevier.com/retrieve/pii/S0927025618300958> (visited on 04/14/2020)

2. Thomas G. Pace, David J. Bentler, and Gregory A. Yankey. “Practical Considerations for Frequency-Dependent Issues in the Explicit Dynamic Analysis of Clearwater Dam”. en. In: *Embankments, Dams, and Slopes*. Denver, Colorado, United States: American Society of Civil Engineers, Oct. 2007, pp. 1–10. ISBN: 978-0-7844-0905-3. DOI: 10.1061/40905(224)3. URL: <http://ascelibrary.org/doi/abs/10.1061/40905%28224%293> (visited on 07/11/2020)
3. Hadi Rahmaninejad, Tom Pace, Shashank Bhatt, Bin Sun, and Peter Kekeneshuskey. “Co-localization and confinement of ecto-nucleotidases modulate extracellular adenosine nucleotide distributions”. en. In: *PLOS Computational Biology* 16.6 (June 2020). Ed. by James M. Briggs, e1007903. ISSN: 1553-7358. DOI: 10.1371/journal.pcbi.1007903. URL: <https://dx.plos.org/10.1371/journal.pcbi.1007903> (visited on 07/02/2020)
4. A.F. Rauch, T.G. Pace, G. Yankey, J.S. Dingrando, and J.A. Schaefer. “Liquefaction under dams and levees: Back-of-the-envelope predictions of deformation”. In: *Association of State Dam Safety Officials - Dam Safety 2007* (2007)
5. Alan F. Rauch, Steve Artman, John C. Kammeyer, Bruce J. Haas, Jeffrey Barrett, Tom Pace, P. Bradford Smiley, Michael J. Steele, and Yong Wu. “Cement-Bentonite Slurry Walls for Seismic Containment of the Kingston Coal Ash Landfill”. en. In: *Grouting 2017*. Honolulu, Hawaii: American Society of Civil Engineers, July 2017, pp. 216–226. ISBN: 978-0-7844-8080-9. DOI: 10.1061/9780784480809.022. URL: <http://ascelibrary.org/doi/10.1061/9780784480809.022> (visited on 07/11/2020)